

Investigation of Interfacial Properties under Electrocatalytic Reduction Conditions

Xiang Li

A thesis
submitted to the Faculty of
the department of Chemistry
in partial fulfillment
of the requirements for the degree of
Doctor of Philosophy

Boston College
Morrissey College of Arts and Sciences
Graduate School
Advised by Prof. Matthias M. Waegele

May 2021

Investigation of Interfacial Properties under Electrocatalytic Reduction Conditions

Xiang Li

Advisor: Matthias Waegle, Assistant Professor of Chemistry

Heterogeneous electrocatalytic reduction is an environmentally friendly method for the conversion of abundant feedstock molecules into valuable products. Examples include the reduction of carbon dioxide to hydrocarbons and the reduction of nitrate to ammonia. Heterogeneous electrocatalysis occurs at the interface between an electrode and an electrolyte. Interfacial properties, such as surface morphology, interfacial electric field, interfacial water structure, and local pH, can substantially influence the activity and selectivity of electrocatalytic reduction processes. However, a comprehensive, molecular-level understanding of how these interfacial properties control electrocatalysis is still largely lacking to date. To develop such an understanding, it is essential to probe the properties of the electrocatalytic interface under operating conditions. This great experimental challenge is further compounded by the fact that the interface often undergoes dynamic changes during catalysis. In this thesis, we took a multimodal approach to characterize the aqueous electrolyte/copper interface during CO_2/CO reduction and hydrogen evolution. Copper is the only pure metal that promotes the reduction of CO_2/CO to hydrocarbons at significant reaction rates. The hydrogen evolution reaction is the main competing reaction in aqueous electrolytes. It is therefore essential to understand how these reactions are controlled by the properties of the interface. In the first part of this thesis, we employed *in-situ* surface-enhanced infrared absorption spectroscopy (SEIRAS) and surface-enhanced Raman spectroscopy (SERS) to investigate dynamic changes of the copper electrode surface. We found that the polycrystalline copper electrode surface undergoes a reconstruction process upon adsorption of CO. The formation of nanoscale metal clusters on the electrode

manifests itself by the appearance of a new CO stretch band, which arises from a CO sub-population bound to undercoordinated copper atoms. The formation of these clusters is reversible, that is, they disappear upon desorption of CO. This work demonstrates that a reaction intermediate such as CO can induce dynamic and reversible changes in the surface morphology of a heterogeneous catalyst. Because the changes are reversible, they would escape *ex situ* measurements. Our findings highlight the need for probing catalytic surfaces under operating conditions. In the second part of this thesis, we focused on how the electrolyte influences electrocatalysis at the aqueous electrolyte/copper electrode interface. Specifically, we explored the mechanisms by which cations of the supporting electrolyte affect the reduction of CO and the hydrogen evolution reaction on copper. With differential electrochemical mass spectrometry (DEMS), we determined to what extent the reduction of CO to ethylene is affected by the identity of the cations of the supporting electrolyte. Ethylene is produced in the presence of methyl₄N⁺ and ethyl₄N⁺ cations, whereas this product is not synthesized in propyl₄N⁺- and butyl₄N⁺-containing electrolytes. With SEIRAS, we found that an intermolecular interaction between surface-adsorbed CO and interfacial water is disrupted in the presence of the two larger cations. This observation suggests that this interaction promotes the hydrogenation of surface-bound CO to ethylene. This work illustrates that weak intermolecular interactions can substantially influence electrocatalytic processes. In a related study, we examined the effect of alkali metal cations of the supporting electrolyte on the hydrogen evolution reaction. We found that, in alkaline conditions, changing the cation from Na⁺ to Cs⁺ has no measurable effect on the HER. Because it is well-established that Cs⁺ promotes the reduction of CO₂/CO to hydrocarbons, the results illustrate the changing the alkali cation enables the selective promotion of this pathway under alkaline conditions. Further, we found that in 0.1 M solutions of NaOH and CsOH of the highest commercially available purity grades, trace impurities of iron deposit on the copper electrode during the hydrogen evolution reaction. Because iron

is a better catalyst for the hydrogen evolution reaction than copper, the rate of the hydrogen evolution reaction is enhanced by up to a factor of ≈ 5 . These findings demonstrate that trace impurities of this ubiquitous metal pose a great challenge for the development of selective catalytic processes for CO_2/CO reduction. This thesis provides a critical study of how the interfacial properties change under the electrocatalytic reduction of CO_2/CO and hydrogen evolution conditions. The properties of both Cu electrode and the electrolyte contribute to the control of the selectivity of these complex electrocatalytic processes.

Contents

1	Introduction	1
2	Theory	8
2.1	Surface-Enhanced Raman Spectroscopy	8
2.1.1	Raman Scattering	8
2.1.2	Surface-Enhanced Raman Spectroscopy	11
2.2	Differential Electrochemical Mass Spectroscopy	13
2.2.1	Viscous Flow and Molecular Flow	14
2.2.2	Residual Gas Analyzer	16
2.2.3	Differential Vacuum Stage	19
2.2.4	Electrochemical cell for DEMS	20
2.2.5	Time Constant for Sampling	22
2.3	Electrochemistry	24
2.3.1	Rotating Disk Electrode	24
2.3.2	Tafel Analysis	26
3	Spectroscopic Observation of Reversible Surface Reconstruction of Copper Electrodes Under CO₂ Reduction Conditions	28
3.1	Introduction	28
3.2	Results	29
3.2.1	ATR-FTIR Spectra of CO on Cu Thin Films	29
3.2.2	SERS Spectra of CO on Cu Foils	34

3.2.3	Time-Resolved ATR-FTIR Spectra of CO on Cu Thin Films	37
3.2.4	Reproducibility	37
3.3	Discussion	38
3.3.1	Assignment of Bands	38
3.3.2	Interpretation of Data in Terms of Surface Reconstruction	41
3.3.3	Consideration of Alternative Interpretations	43
3.4	Conclusions	44
3.5	Experimental Procedures	45
3.5.1	Materials for Cu Thin Film Preparation	45
3.5.2	Materials for Electrode Preparation and Spectro-Electrochemical Measurements	45
3.5.3	Preparation of Cu Thin Films	46
3.5.4	ATR-FTIR Measurements	47
3.5.5	Electrochemical Methods for ATR-FTIR Measurements	48
3.5.6	Preparation of the Raman-Active Surface	48
3.5.7	Raman Measurements	49
3.5.8	Lineshape Analysis	50
3.6	Acknowledgements	50
3.7	Original Publication	51
4	Hydrogen bonding steers the product selectivity of electrocatalytic CO reduc- tion	52
4.1	Introduction	52
4.2	Results and Discussion	54
4.2.1	Effects of Alkyl ₄ N ⁺ Cations on CO Reduction	54
4.2.2	SEIRAS of the Cu/Electrolyte Interface	60

4.2.3	Insensitivity of the CO Surface-Coverage on Alkyl ₄ N ⁺ Identity . . .	66
4.2.4	Cation-Dependent Interfacial Electric Field	70
4.2.5	Dependence of the CO _{ads} -H ₂ O Interaction on Cation Identity . . .	75
4.3	Conclusions	79
4.4	Experimental Procedures	81
4.4.1	Materials	81
4.4.2	DEMS System	81
4.4.3	Cu Foil Preparation	82
4.4.4	Electrochemical Methods for DEMS	82
4.4.5	Cu Thin Film Preparation for SEIRAS	83
4.4.6	Electrochemical Methods for SEIRAS	83
4.4.7	SEIRAS Measurements	88
4.5	Acknowledgements	89
4.6	Original Publication	89
5	Impact of Alkali Metal Cations and Iron Impurities on the Evolution of Hydrogen on Cu Electrodes in Alkaline Electrolytes	90
5.1	Introduction	90
5.2	Results and Discussion	91
5.2.1	Effect of Trace Iron and Nickel Impurities on the HER on Cu Electrodes	91
5.2.2	Impact of Iron Deposits on Tafel Slopes and Exchange Currents	97
5.2.3	Impact of Iron on the HER at pH 9	100
5.2.4	Effects of Cations on the HER	101
5.2.5	DFT Examination of the Effects of Cations on HER Elementary Processes	105

5.3	Conclusions	106
5.4	Experimental Procedures	107
5.4.1	Materials	107
5.4.2	Electrode Preparation	107
5.4.3	Electrochemical Measurements	107
5.4.4	Pre-electrolysis	109
5.4.5	X-ray Photoelectron Spectroscopy (XPS)	109
5.4.6	Inductively Coupled Plasma - Atomic Emission Spectroscopy (ICP-AES)	110
5.5	Acknowledgements	110
5.6	Original Publication	110
6	Summary and Future Perspective	111

List of Figures

2.1	Energy-level diagram of the states involved in Rayleigh scattering and Raman scattering.	9
2.2	A localized surface plasmon. Reproduced from Ref [92]	12
2.3	Flow regimes for gas flowing as a function of the gas pressure and flow-controlling dimensions. Reprinted with permission from [110]. Copyright [2007], American Vacuum Society.	15
2.4	Sketch of the composition of a typical RGA.	16
2.5	Peak shape of mass/charge ratio 2 with our RGA.	18
2.6	Scheme of the vacuum system. (1)(3)(7) Ball valve (2) Pneumatic valve (4)(6) Vacuum pressure transducer (5) Metering stem needle valve (8) Liquid nitrogen cold trap	20
2.7	Electrochemical cell setup for DEMS.	21
2.8	Electrochemical cell setup for DEMS and SEIRAS.	22
2.9	H ₂ partial pressure measurement with the electrochemical cell shown in figure 2.7 with the sampling tip distance of 100 μm . A cathodic potential drop was applied at time 0 s. Two-stage pressure reduction system shows better time constant compared to the single-stage.	23
2.10	(A) H ₂ partial pressure measurement with the electrochemical cell shown in figure 2.7. The tip distance is as indicated in the figure. A cathodic potential drop was applied at time 0 s. (B) The time constant got from (A) is plotted versus the tip distance and the linear fitting is also shown.	24

2.11	Motion of the solution at the surface of an RDE.	26
3.1	Dependence of the IR spectrum in the C≡O stretch region on applied potential.	30
3.2	Dependence of the integrated areas of the LFB and HFB on applied potential.	30
3.3	(A) Representative spectra collected by stepping the potential in cathodic direction (cathodic scan) and the corresponding spectra recorded after the most cathodic potential (−1.10 V) was reached (anodic scan). (B) Integrated band areas derived from the spectra shown in part A, anodic scan, plotted together with the data from Figure 3.2	32
3.4	(A) Representative spectra showing the loss of absorbance at $\approx 1540 \text{ cm}^{-1}$. (B) Integrated band area of the carbonate band as a function of potential. (C) Comparison of the scaled carbonate band (CB; scaling factor: -0.22) with the corresponding curves of the LFB and HFB.	33
3.5	Dependence of the spectral lineshape in the C≡O stretch region on applied potential. Values in the figure denote potential in volts vs. SHE.	34
3.6	Areas of the LFB and HFB in 1 atm CO (solid symbols) and 1 atm CO ₂ (open symbols).	35
3.7	Dependence of the band areas on potential at different partial pressures of CO. The reduced partial pressure data was collected using a 1:9 mixture of CO and Ar. In both cases, the LFB acquires a substantial integrated area of $\approx 75\text{-}100 \text{ mOD}\cdot\text{cm}^{-1}$ at the onset potential of the HFB.	35
3.8	Dependence of the Raman spectrum on applied potential.	36
3.9	Potential dependencies of the areas of the bands shown in Figure 3.8 . . .	36

3.10	(A) Time evolution of the spectrum following a potential step from -0.70 to -1.10 V vs SHE. (B) Kinetics of the integrated areas of the LFB and HFB. The gray shaded area highlights the period in which the HFB is absent. The lines indicate double and single exponential fits to the LFB and HFB, respectively. The inset shows the LFB offset by $b = 100$ mOD cm^{-1} and multiplied by $m = 1.4$	38
3.11	(A) Comparison of the data presented in Figure 3.2 with another data set collected on a separately prepared thin film (shown in Figure 3.6), illustrating the high reproducibility of the data. (B) Reversibility of the lineshape changes of the additional data set presented in (A).	39
3.12	(A) Reversibility of the spectral lineshape changes under CO_2 atmosphere for the data presented in Figure 3.6. (B) Additional data set collected on a separately prepared thin film. The slight hysteresis observed in CO_2 atmosphere is attributed to the relatively high cathodic potentials which exert stress on the copper films.	39
3.13	Illustration of reproducibility of the potential dependencies of the band areas derived from Raman spectra. Each panel represents a data set collected on a different day.	40
3.14	Comparison of Raman spectra collected in D_2O and H_2O . The absence of an isotope shift for the hydrocarbon band ($2800\text{-}3000$ cm^{-1}) indicates that the band is not related to the reduction reaction, but due to adsorption of an exogenous species. The enhancement of this band at more cathodic potentials is explained by the reconstruction process. Values in the figure denote potential in volts vs. SHE.	43
3.15	Cyclic voltammogram (50 mV s^{-1}) of a copper thin film in CO_2 saturated 0.1 M KHCO_3 . The geometric area of the electrode was ≈ 1.9 cm^2	47

3.16	Cyclic voltammogram (10 mV s^{-1}) of a copper foil in CO_2 saturated 0.1 M KHCO_3 . The geometric area of the electrode was $\approx 1 \text{ cm}^2$	49
4.1	DEMS measurements. (A) Electrochemical current density based on the geometric area of the electrode, (B) H_2 partial pressure ($m/z = 2$ for H_2^+), and (C) C_2H_4 partial pressure ($m/z = 26$ for C_2H_2^+) recorded during the electroreduction of CO on Cu in the presence of different cations as indicated.	55
4.2	The $m/z = 26$ signal is absent in Ar -purged electrolyte. (A) Electrochemical current density during the DEMS measurements. (B) H_2 partial pressure, and (C) C_2H_4 partial pressure in the presence of aqueous solutions of $0.1 \text{ M methyl}_4\text{N}^+$ borate under 1 atm of CO (solid line) or Ar (dashed line). At high current densities ($\approx 10 \text{ mA cm}^{-2}$), hydrogen bubbles cover the electrode within a few seconds. Stochastic desorption of the bubbles causes the observed current density fluctuations. A significant fraction of the bubbles does not interact with the sampling tip. Therefore, a fraction of the hydrogen escapes mass spectrometric detection, giving rise to discrepancies between current density and detected hydrogen partial pressure.	57

4.3	The $m/z = 26$ signal is absent when a Pt electrode is used. (A) Electrochemical current density during the DEMS measurements. (B) H_2 partial pressure, and (C) C_2H_4 partial pressure in the presence of aqueous solutions of 0.1 M methyl $_4N^+$ borate under 1 atm of CO on Cu (solid line) or Pt (dashed line). Reaction potentials that gave the same amount of detected H_2 were chosen. The lower H_2 detection efficiency in the case of Pt compared to the experiments with Cu is attributed to differences in H_2 bubble nucleation, potentially due to differences in surface morphology. Further, the thin Pt foil has a higher propensity to warp. Therefore, the electrode-sampling tip distance for the experiments with Pt could not be precisely controlled, which impacts the collection efficiency.	58
4.4	The $m/z = 26$ signal is unaffected by the use of deuterated alkyl $_4N^+$. (A) Electrochemical current density during the DEMS measurements. (B) H_2 partial pressure, and (C) C_2H_4 partial pressure detected in the presence of aqueous solutions of 0.1 M $(CH_3)_4N^+$ (solid line) and $(CD_3)_4N^+$ chlorides (dashed line) under 1 atm CO.	59
4.5	The relative partial pressures of the observable m/z values are consistent with the relative signal intensities of the standard mass spectrum of C_2H_4 . (A) $m/z = 23, 25, 26, 27$ signals for the 0.1 M methyl $_4N^+$ -experiment presented in Figure 1C of the main text. (B) Normalized standard mass spectrum of C_2H_4 from the NIST Chemistry Webbook[148]	61

4.6	GC-MS confirms of the formation of ethylene by CO reduction. (A) GC-MS total ion chromatograms (TIC) of a C ₂ H ₄ standard sample and gaseous products of electrolysis in CO-saturated aqueous solutions of 0.1 M methyl ₄ N ⁺ borate as indicated. (B) Mass spectra of the chromatogram peaks at 17.35 min obtained from the gaseous products collected during electrolysis at -1.49 V vs. SHE. GC-MS experiments were carried out in an H-cell. The cathode and anode compartments were separated by a Selemion AMV anion-exchange membrane (AGC Engineering Co.; Chiba, Japan). Each compartment contained 10 mL of electrolyte. Prior to the start of electrolysis, the electrolyte was saturated with CO and the cell was sealed. 100 μL of gaseous sample from the headspace of the cell was injected into GC-MS after 40 min of electrolysis.	62
4.7	Representative C≡O stretch spectra of CO _{ads} as a function of applied potential in the presence of a solution of 0.1 M butyl ₄ N ⁺ chloride in D ₂ O.	63
4.8	Scheme of spectroelectrochemical cell.	64
4.9	(A) Representative cyclic voltammogram obtained following five Cu film cleaning cycles from 0.08 to -0.49 V at a scan rate of 50 mV s ⁻¹ . (B) Representative CVs taken at scan rates of 20 (red), 40 (blue), 60 (green), 80 (yellow), and 100 mV s ⁻¹ (purple) to measure the double layer capacitance. (C) The double layer charging current vs. scan rate for the data shown in graph (B) (red squares) and the linear fit (black dotted line) to the data. The roughness of the film was calculated by dividing the slope of the fitted line in graph (C) by a factor of two and a reference double layer capacitance value of 28 μF cm ⁻² for a smooth Cu surface[149]	65
4.10	AFM image of an as-synthesized Cu film on a Si ATR crystal.	65

4.11	The observed trends in the $m/z = 26$ signal are also observed in the presence of the chloride anion. (A) Electrochemical current density during the DEMS measurements. (B) H_2 partial pressure, and (C) C_2H_4 partial pressure detected in the presence of aqueous solutions of 0.1 M methyl $_4N^+$ chloride (solid line) and butyl $_4N^+$ chloride (dashed line) under 1 atm CO .	67
4.12	The normalized O–H stretch spectra in the presence of aqueous solutions of 0.1 M methyl $_4N^+$ and butyl $_4N^+$ borate at -1.29 V. The 3675 cm^{-1} band is prominent in methyl $_4N^+$ -containing electrolyte but absent in the presence of butyl $_4N^+$.	68
4.13	Representative $C\equiv O$ stretch spectra in solutions of 0.1 M methyl $_4N^+$, ethyl $_4N^+$, and propyl $_4N^+$ chloride in D_2O .	68
4.14	Linear sweep voltammetry current-voltage curves for the spectroscopic data presented above. Arrows indicate the sweep direction.	69
4.15	Integrated $C\equiv O$ stretch band areas of CO_{ads} as a function of applied potential in the presence of different cations as indicated. Each trace is an average of three independent experiments. The standard errors are indicated.	70
4.16	Peak frequencies of the $C\equiv O$ stretch band of CO_{ads} as function of applied potential in the presence of different cations as indicated. The lines are linear fits to the data. The standard errors are indicated.	71
4.17	Dependence of the interfacial electric fields on applied potential in the presence of different electrolyte cations as indicated.	75
4.18	Normalized O–D stretch spectra recorded at a potential of -1.02 V in the presence of different cations as indicated. The unnormalized spectra are provided in the SI Appendix (Figure S14).	76

4.19 (A) Representative O–D stretch spectra in 0.1 M methyl ₄ N ⁺ chloride in D ₂ O. (B) Integrated band areas of the C≡O stretch band (red circles) and O–D stretch band at 2710 cm ⁻¹ (blue squares) as a function of applied potential.	77
4.20 O–D stretch spectra in Ar-purged 0.1 M methyl ₄ N ⁺ chloride electrolyte confirm that the 2710 cm ⁻¹ band is only present for the CO-covered Cu electrode.	78
4.21 Possible CO _{ads} coupling mechanism on Cu(100), as proposed by Bagger et al. [143]. (A) In the presence of methyl ₄ N ⁺ (or ethyl ₄ N ⁺), interfacial waters are available to stabilize the CO dimer by hydrogen bonding. (B) In the presence of butyl ₄ N ⁺ (or propyl ₄ N ⁺), the formation of the CO dimer is blocked due to the displacement of interfacial water by these hydrophobic cations.	80
4.22 Raw DEMS data for methyl ₄ N ⁺ . (A) Electrochemical current density, (B) H ₂ partial pressure, and (C) C ₂ H ₄ partial pressure recorded during two independent experiments (thin red and blue traces) of CO electroreduction on Cu. The thick black trace represents the smoothed average of the two experiments.	84
4.23 Raw DEMS data for ethyl ₄ N ⁺ . (A) Electrochemical current density, (B) H ₂ partial pressure, and (C) C ₂ H ₄ partial pressure recorded during two independent experiments (thin red and blue traces) of CO electroreduction on Cu. The thick black trace represents the smoothed average of the two experiments.	85

4.24	Raw DEMS data for propyl ₄ N ⁺ . (A) Electrochemical current density, (B) H ₂ partial pressure, and (C) C ₂ H ₄ partial pressure recorded during two independent experiments (thin red and blue traces) of CO electroreduction on Cu. The thick black trace represents the smoothed average of the two experiments.	86
4.25	Raw DEMS data for butyl ₄ N ⁺ . (A) Electrochemical current density, (B) H ₂ partial pressure, and (C) C ₂ H ₄ partial pressure recorded during two independent experiments (thin red and blue traces) of CO electroreduction on Cu. The thick black trace represents the smoothed average of the two experiments.	87
4.26	An example of FTIR data interpolation. The data presented was collected in the presence of 0.1 M butyl ₄ N ⁺ in D ₂ O at potential of -1.02 V. The interpolated data (red) captures the CO peak frequency more accurately than the raw data (black).	89
5.1	Consecutive CVs of a polycrystalline Cu RDE in 0.1 M solutions of as-received (A) NaOH (99.99%) and (B) CsOH (99.95%). The CVs were taken at a scan rate of 10 mV s ⁻¹ and a rotation rate of 2500 rpm of the RDE. The purity of each salt is indicated in the parenthesis in each panel. The numbers in the panels refer to the cycle number and “rev” denotes the respective reverse (anodic) scan. For clarity, the reverse scans of the other cycles are not shown. Steady state measurements were collected right after the eleventh CV.	92
5.2	Current densities at constant applied potentials (-0.60 V vs. RHE for 0.1 M CsOH and -0.68 V vs. RHE for 0.1 M NaOH) prior to the interrogation of the Cu RDE with XPS.	95

5.3	X-ray photoelectron spectra of the Cu RDE before and after 1.9 h of electrolysis in the regions for (A) Fe and (B) Ni.	96
5.4	Logarithmic current densities as a function of overpotential during the cathodic forward scan of the second CV for each electrolyte at RDE rotation rates of 1500 rpm (solid markers) and 2500 rpm (hollow markers).	97
5.5	Tafel plots for the forward (cathodic) scans of the second CVs. The data represent the average of six independent experiments for each electrolyte. The error bars represent one standard deviation. For clarity, only a subset of the collected data points is shown on the plot. The Tafel plots for the 6th and 11th cycles are reported in Figure 5.6	98
5.6	Tafel plots for the forward (cathodic) scans of the (A) 6th and (B) 11th CVs at pH 13.	99
5.7	Consecutive CVs of a polycrystalline Cu RDE in 0.1 M (A) Na ⁺ and (B) Cs ⁺ electrolytes (pH ≈ 9) prepared from NaOH (99.99%) and CsOH (99.95%) and boric acid. For clarity, only the forward scans of the CVs are shown. Steady state measurements were collected right after the eleventh CV.	101
5.8	Tafel plots for the forward (cathodic) scans of the (A) 2nd, (B) 6th, and (C) 11th CVs in 0.1 M alkali metal borate electrolytes (pH ≈ 9). The data represent the average of six independent experiments for each electrolyte. The error bars represent one standard deviation. For clarity, only a subset of the collected data points is shown on the plots.	102

5.9 Consecutive CVs of a polycrystalline Cu RDE in 0.1 M solutions of pre-electrolyzed (A) NaOH and (B) CsOH. The CVs were taken at a scan rate of 10 mV s^{-1} and a rotation rate of 2500 rpm of the RDE. The numbers in the panels refer to the cycle number and “rev” denotes the respective reverse (anodic) scan. For clarity, the reverse scans of the other cycles are not shown. Steady state measurements in 0.1 M CsOH were collected right after the eleventh CV. 103

5.10 Tafel plots for the forward (cathodic) scans of the second CV in pre-electrolyzed electrolytes. The data represent the average of three independent experiments for each electrolyte. The error bars represent one standard deviation. For clarity, only a subset of the collected data points is shown on the plot. 104

Acknowledgments

My PhD study in the Boston College will be the most memorable journey of my life. These years have been both long and short, full of sweet and sour, but also full of harvest and growth. I would like to thank everyone who spent a good time with me in the past few years, it is your help that enabled me to overcome difficulties until the successful completion of my studies.

First, I would like to acknowledge my doctor advisor, Prof. Matthias M. Waegele. His broad vision, rigorous academic attitude, and style of working for excellence have deeply infected and inspired me. The completion of every research project is based on his dedicated guidance. He kept discussing with me and guide me to understand the research background of the project, gain the basic knowledge and design reasonable experiments. He made me a more well-organized person and know how to think logically. I am proud to recognized myself as his advisee.

I would also like to acknowledge my thesis committee members, Prof. Dunwei Wang and Prof. Udayan Mohanty, for their time and efforts. Their comments are irreplaceable help to me in the completion of this thesis. In particular, I would like to thank Prof. Chia-Kuang Tsung. I would like to thank him for his generous help in my projects in the past five years. His energetic and optimistic research spirit will always influence me.

I would like to thank Xiahui Yao and Da He, for their kind help during the initial two years, which is essential for me to start the research work in Boston College. I am grateful to Prof. Michael J. Janik, Naveen Agrawal and Hansel Montalvo-Castro from Pennsylvania State University for successful collaborations. I would also like to thank Haoyi Li from Boston College, Prof. De-en Jiang and Chuanye Xiong from the University of California, Riverside for pleasant cooperation and inspiration of our reserch project.

I am sincerely grateful to Jingyi Li and Charuni M. Gunathunge for the six years we have worked together. We helped each other to overcome difficulties and supported each other in both research and life. I also want to thank Vincent Ovalle, Paul Hicks, Wei-Shang Lo, Jinchun Yang, Connor Gallacher and Julie Hong. They are always there to provide help. I am lucky to have you guys by my side.

Fianlly, I would like to thank my parents, Weiguo Li and Lianfen Xia, for their endless love and support. It makes me brave to pursue what I want to do. To my husband, Jie Zhou, thanks for your support in every decision I make and your warm hugs when I am tired. Thank you for making my life colorful and for your sacrificed dream of a PhD.

Chapter 1

Introduction

Heterogeneous electrocatalytic reduction is an environmentally friendly method for transforming feedstock into valuable products [1]. For example, it carries the hope for future mass production of ammonia from dinitrogen reduction with a lower energy consumption than the traditional Haber-Bosch synthesis [2, 3]. Compared to methods that employ chemical reductants, electrocatalytic processes can directly utilize electrical energy from renewable sources, such as wind and solar power [4]. Although the cost of renewable electricity is decreasing substantially, efficient grid balancing poses a challenge [5, 6]. The electrocatalytic transformation of CO₂ to hydrocarbons provides an elegant solution by storing excess electrical energy in the form of chemical bonds [4, 7–10]. The electrocatalytic conversion of CO₂ to fuels and high-value commodity chemicals closes the carbon cycle when renewable electric energy is utilized [11]. In this regard, substantial progress has been made in recent years. For example, ethylene evolution with 70% faradaic efficiency at the current density of 100 mA cm⁻² from CO₂ electrocatalytic reduction with a copper gas diffusion electrode in an alkaline electrolyte has been reported [12]. Further, the desired performance and selectivity of electrocatalytic processes can be manipulated by tuning the electrode potential [1, 13, 14].

Despite their great promise, electrocatalytic processes still suffer from their own limitations, such as poor selectivity towards desired products, requirement of high overpotentials

to achieve reasonable rates, and performance losses after short periods of operation [8, 15–18]. For instance, CO₂ electrocatalytic reduction in aqueous electrolyte leads to a wide range of products, including CH₄, HCOOH, HCHO, CH₃OH, and CO, rendering the Faradaic efficiency towards any specific product low. Due to the similarity of the redox potentials of these products, it is challenging to tune the selectivity for desired chemicals [8]. It becomes even more difficult to increase the faradaic efficiency for hydrocarbons because the competing side reaction of hydrogen evolution occurs at a comparable potential.

To design stable, efficient, and selective electrocatalysts, it is essential to understand how the chemical and physical characteristics of electrocatalytic interfaces modulate reaction processes of interest. Interfacial properties include but are not limited to surface morphology, interfacial electric field, interfacial water structure, and the pH in the vicinity of the electrode. It is well established that these interfacial properties can greatly affect the activity and selectivity of the electrocatalytic reduction processes [19–27], as illustrated by the examples given in the following.

The surface morphology of the electrode can greatly affect catalytic processes. For example, for CO₂ reduction, it has been shown that the onset potential of ethylene evolution on nanostructured Cu cube electrodes immersed in an electrolyte at pH 7 is shifted by ≈ 200 mV compared to the onset potential of this product on polycrystalline Cu [19]. It also has been shown that the facet of the metal electrode can steer the electrocatalytic selectivity. For example, Cu(100) exhibits a ≈ 100 mV earlier onset potential for ethylene evolution compared to Cu(111) [20]. The oxidation state of the Cu electrode, which can be tuned by various pre-treatments, influences the electrocatalytic process greatly. Electro-redeposited copper shows the presence of Cu⁺, which can stabilize ethylene-generation intermediates and help sustain an ethylene partial current density of up to 161 mA cm⁻² [28].

The cations of the supporting electrolyte can greatly affect the electrocatalytic reduction processes [27]. Cations can affect the electrocatalysis in the following ways: (1)

modulating the interfacial electric field [29–33]; (2) blocking the active sites for the desired reaction [34–40]; (3) buffering the pH of the interfacial region [41, 42]; (4) altering the interfacial water structure [43, 44]; (5) interacting with the adsorbed reaction intermediates [45–49]. Because of the complexity of cation effects on electrocatalytic processes, they are a rich and active field of research. For example, doubling of the partial current density of ethylene has been reported when switching from LiHCO_3 to CsHCO_3 for CO electrocatalytic reduction [22]. Density functional theory calculations have shown that the electric field on the order of $1 \text{ V } \text{\AA}^{-1}$ created by the cations in the outer Helmholtz plane is able to stabilize intermediates for C-C coupling, thereby facilitating C_2H_4 production [22]. Furthermore, it has been reported that the reduction kinetics of surface-adsorbed CO on Cu is faster by one order of magnitude in the presence of Cs^+ compared to the kinetics in Li^+ -containing electrolyte on a Cu electrode at a potential of -1.51 V vs. SHE [50]. With vibrational Stark spectroscopy, the strong interfacial electric field in the presence of Cs^+ was identified as the origin of the acceleration of the reaction kinetics.

The pH of the electrolyte also plays a central role in electrocatalysis. For example, the molar ratio between CO and formate as the product from CO_2 electrocatalytic reduction on Sn electrodes changes from 1 to 0.15 when the pH changes from 2.9 to 7.8 [24].

Studying electrocatalytic interfaces is further complicated by the fact that they tend to undergo dynamic changes during electrolysis. For example, it has been reported that a polycrystalline Cu electrode undergoes surface reconstruction to Cu(111) first and then Cu(100) on a tens-of-minutes scale in 0.1 M KOH electrolyte under carbon dioxide reduction conditions [51]. The interfacial pH also tends to change during the electrocatalytic reduction processes as protons are consumed in the reaction [52, 53]. The pH is critical to be determined because it plays an active role in multi-proton/electron transfer processes [54]. A pH change can also induce changes in surface species. For example, an irreversible population of bridge-bonded CO ($\text{CO}_{\text{bridge}}$) on polycrystalline Cu electrodes

under alkaline conditions has been reported [55]. $\text{CO}_{\text{bridge}}$ is inert to further electrocatalytic reduction.

The surface speciation of Cu electrodes can also experience great change with the applied potential. For example, with surface-enhanced Raman spectroscopy, it has been observed that multiple oxide and hydroxide species exist on Cu surfaces at potentials relevant to CO electrocatalytic reduction in alkaline electrolyte [56]. The oxidation state of the Cu electrode and the population of the surface adsorbed species (atop-bound CO and bridge-bound CO) are shown to change with the electrocatalytic CO_2 reduction process [57].

All the examples above illustrate that, to overcome the limitations noted above and improve the performance of the electrocatalysts, a rigorous understanding of how the interfacial properties affect the electrocatalytic reduction processes is crucial. In this regard, *in situ* probing of interfacial properties under the electrocatalytic conditions is essential.

In this thesis, we have utilized a multimodal approach to investigate the interface between aqueous electrolytes and polycrystalline copper electrodes to reveal how the interface properties affect the CO_2/CO reduction process and the competing hydrogen evolution reaction. In the first part of the thesis, we focus on the investigation of Cu electrode surface morphology under CO_2 reduction conditions. The surface morphology of the Cu electrode has attracted extensive interest among the various factors that affect CO_2 reduction. Studies employing nanostructured electrodes [58–70] and electrodes with well-defined crystallographic facets [26, 71–77] have established the impact of the surface structure on the selectivity of the CO_2 reduction reaction. Although some works have investigated the relationship between the surface morphology of the electrode and their reactivity [58–60, 65, 67, 68], the surface morphologies of the electrodes were usually examined *ex-situ*. However, they can greatly change during catalysis [51, 78–81]. Further, the change of the surface morphologies can be reversible, that is, the morphology

can return to its original state after the catalysis [78]. Therefore, a change of the surface morphology may escape *ex-situ* measurements.

Electrochemical scanning tunneling microscopy (ECSTM) has been reported to investigate the change of the Cu electrode surface morphology during CO reduction in 0.1 M KOH [79]. However, it can only be utilized under low overpotential conditions due to the interference of the large current from CO reduction with the tunneling current [51, 79]. Alternatively, surface-enhanced infrared absorption spectroscopy (SEIRAS) and surface-enhanced Raman spectroscopy (SERS) coupled with a suitable molecular probe can provide atomic level information of the structure [81–85]. As an on-pathway intermediate of electrocatalytic reduction of CO₂, CO can be used as the probe of the change of the surface morphology under the reaction conditions [84]. By analyzing the lineshape of CO_{ads} on the Cu electrode in both SEIRAS and Raman spectra, we have revealed that the morphology of the Cu electrode surface is not static but dynamically changes under the typical CO₂ reduction conditions. The surface morphology dynamic change induces a new CO adsorption site, which is corresponding to a band centered around 2080 cm⁻¹. The new generated adsorption site is expected to have profound effects on the catalytic properties of the Cu electrode since the CO stretching frequency is significantly different ($\approx 30\text{cm}^{-1}$) from the original adsorption sites.

Beyond the surface morphology, we have also investigated how the electrolyte influences electrocatalysis at the aqueous electrolyte/copper electrode interface. In the second part of the thesis, we have revealed the molecular origin of the dependence of the product selectivity on the characteristics of the electrochemical double layer. Tuning the electrochemical double layer by changing the cations of the supporting electrolyte is a powerful way. Herein, we choose a series of quaternary alkyl ammonium cations (alkyl₄N⁺) to systematically manipulated the interfacial properties of the aqueous electrolyte/polycrystalline Cu interface. The radius of these cation increases with increasing

alkyl chain length, which enabled us to tune the width of the double layer and the strength of the interfacial electric field under a given applied electrode potential. We employed differential electrochemical mass spectrometry (DEMS) to investigate the effect of these cations on the ethylene evolution from the reduction of CO_{ads} . We can only observe the ethylene evolution in methyl $_4\text{N}^+$ and ethyl $_4\text{N}^+$ -containing electrolyte, while the ethylene evolution is below the detection limit in the presence of propyl $_4\text{N}^+$ and butyl $_4\text{N}^+$. By combining with the SEIRAS, we have excluded the possibilities that cations blocking and cation-tuned interfacial electric field are the reasons for the absence of ethylene evolution in propyl $_4\text{N}^+$ and butyl $_4\text{N}^+$ -containing electrolyte. And then we have revealed that the interfacial water plays a critical role in ethylene evolution from CO reduction on the Cu electrode, which can stabilize the key intermediate, CO dimer.

In the third part of this thesis, we examined the effects of alkali metal cations of the supporting electrolyte on the hydrogen evolution reaction (HER) on Cu electrodes. In aqueous electrolytes, the HER is often the main competing reaction of desired electrocatalytic reduction reactions. For example, the Faradaic efficiency of hydrogen is higher than 50% at an applied potential of -1.2 V vs RHE in CO_2 -saturated 0.1 M KHCO_3 electrolyte, where it competes with methane formation [16]. Therefore, it is essential to understand how the HER is controlled by the properties of the interface. It has been reported that under the electrocatalytic reduction of CO_2 reaction conditions at neutral pH, there is no alkali metal cation effect observed in the partial current density of hydrogen evolution [22]. However, an enhanced hydrogen evolution was reported from Li^+ to Cs^+ -containing electrolyte at pH of 13 with the reduction of CO on Cu [20]. However, the impact of alkali metal cations on the HER on Cu electrodes in alkaline conditions has not been investigated in the absence of other Faradaic reactions.

Herein, we have revealed that even in the electrolyte prepared with high purity salts, trace amounts of Fe can deposit on the Cu electrode. Fe promotes hydrogen evolution. We

have also found that Fe deposits at a higher rate at high pH. With purified electrolyte, we observed virtually identical HER current densities in Na⁺ and Cs⁺-containing electrolyte, indicating the absence of a significant cation effect on the HER on Cu electrode under alkaline conditions. Therefore, Cs⁺ can be employed to selectively promote CO reduction towards ethylene in alkaline conditions.

Chapter 2

Theory

2.1 Surface-Enhanced Raman Spectroscopy

2.1.1 Raman Scattering

When light is scattered by a molecule, most of the photons are scattered with the same energy as the incident light. This is the elastic scattering or Rayleigh scattering [86]. Among the scattered photons, a small fraction (1 in 10 million) is scattered with different energy compared to the incident light [87]. The process of scattering with different energy is called Raman scattering. It is named after the scientist C.V. Raman [88], who was awarded the Nobel Prize in Physics in 1930 for this discovery.

As shown in figure 2.1, the incident photons can excite a molecule to a virtual energy state [86]. The excited molecules then relax to various vibrational energy states, which may differ from the original energy state and emit photons of various energies. The difference in energy between the incident and emitted photons is regarded as the Raman shift, which contains information of vibrational energy states of the molecule. When the energy of the emitted photons is smaller than the incident photons, the Raman shift is a Stokes shift. In another case, some molecules may already be in the excited vibrational energy states before the interaction with the incident photons. Once they are excited to the virtual energy state, they can relax to the vibrational energy state that is lower than their original

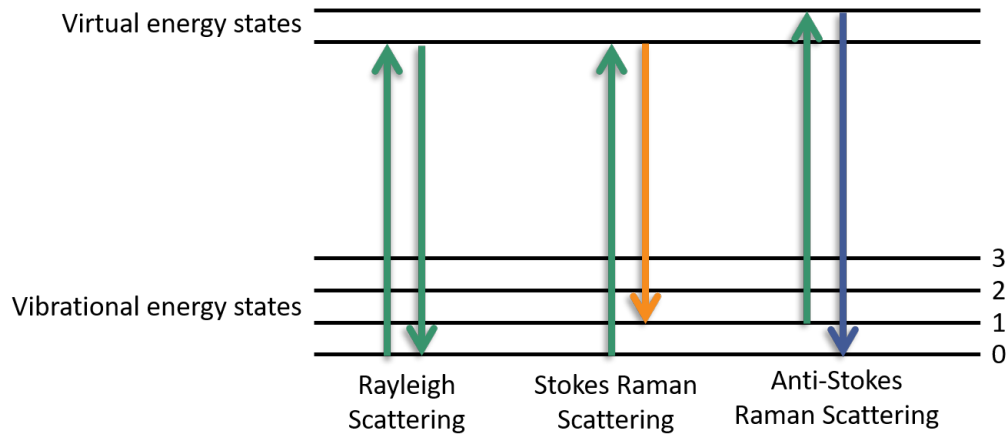


Figure 2.1: Energy-level diagram of the states involved in Rayleigh scattering and Raman scattering.

vibrational energy state. This leads to the energy of the emitted photons being higher than the incident photons. In this case, the Raman shift is an Anti-Stokes shift. Normally, the intensity of peaks with Stokes shift is higher than Anti-Stokes shift. This is simply because the percentage of molecules in the ground state is much larger than the molecules in the excited energy states according to the Boltzmann distribution.

Raman spectroscopy is based on Raman scattering. By measuring and analyzing the Raman spectrum, the information about the vibrational and rotational energy states of the target molecules can be ascertained [86]. The Raman shift is only dependent on the vibrational-rotational energy levels of the molecules, and not affected by the energy of the incident light.

To tell whether a specific vibrational/rotational mode of a molecule is Raman active, we can refer to the classic theory of Raman scattering [86]. The incident light used for Raman spectroscopy is monochromatic (normally laser) and its electric field strength (E) oscillates with time. It can be expressed as:

$$E = E_0 \cos 2\pi\nu_0 t \quad (2.1)$$

where E_0 is the amplitude of the field and ν_0 is the frequency of the light. Once the light interacts with a molecule, the induced electronic dipole moment (P) is:

$$P = \alpha E = \alpha E_0 \cos 2\pi \nu_0 t \quad (2.2)$$

where α is the polarizability of the target molecule. Assuming that one of the vibrational/rotational modes of the target molecule is vibrating/rotating with frequency ν_m , the nuclear displacement (q) can be expressed as:

$$q = q_0 \cos 2\pi \nu_m t \quad (2.3)$$

where q_0 is the equilibrium position of the target molecule. For a small amplitude of vibration/rotation, the relationship between q and α is linear. Therefore, we have:

$$\alpha = \alpha_0 + \left(\frac{\partial \alpha}{\partial q}\right)q + \dots \quad (2.4)$$

where α_0 is the polarizability at the equilibrium position. Taken together, the dipole moment can be expressed by the electric field strength of the incident light (E) and the polarizability of the molecule (α):

$$\begin{aligned} P &= \alpha E_0 \cos 2\pi \nu_0 t \\ &= \alpha_0 E_0 \cos 2\pi \nu_0 t + \left(\frac{\partial \alpha}{\partial q}\right)q E_0 \cos 2\pi \nu_0 t \\ &= \alpha_0 E_0 \cos 2\pi \nu_0 t + \left(\frac{\partial \alpha}{\partial q}\right)q_0 E_0 \cos 2\pi \nu_0 t \cos 2\pi \nu_m t \\ &= \alpha_0 E_0 \cos 2\pi \nu_0 t + \frac{1}{2} \left(\frac{\partial \alpha}{\partial q}\right)q_0 E_0 \{ \cos[2\pi(\nu_0 + \nu_m)t] + \cos[2\pi(\nu_0 - \nu_m)t] \} \end{aligned} \quad (2.5)$$

The first term $\alpha_0 E_0 \cos 2\pi \nu_0 t$ in the equation 2.5 corresponds to Rayleigh scattering, while the left two terms correspond to Raman scattering. If $\frac{\partial \alpha}{\partial q}$ is not zero, the items correspond-

ing to Raman scattering are not zero and the specific vibrational/rotational mode is Raman active.

2.1.2 Surface-Enhanced Raman Spectroscopy

Surface enhanced Raman scattering (SERS) was first observed by Fleischmann et al. in 1974 [89]. They found that the intensity of Raman scattering of pyridine molecules adsorbed on a Ag electrode was enhanced dramatically. Initially, they explained the enhancement by an increased surface area from the higher roughness of the Ag electrode. However, the enhanced Raman scattering can be as high as 10^6 , which is significantly higher than the increase of the surface area.

Two mechanisms are believed to be responsible for SERS enhancement: The electromagnetic effect and the chemical effect [90]. These two mechanisms contribute simultaneously to the overall enhancement [91]. The electromagnetic effect is a long-range effect. It can enhance the Raman intensity by a factor of 10^{10} . The chemical effect is a short-range effect. It can enhance the Raman intensity by a factor of 10^2 .

According to the electromagnetic mechanism, free electrons at the metal surface are excited by the incident light [90]. The incident electric field creates a distortion in the electron cloud and induces a collective electron oscillation. This is called surface plasmon as shown in figure 2.2. Once the incident light is at the resonance frequency of the surface plasmon, the absorption of the light and the response of the electrons will be strong. Then the scattering of the metal substrate will be enhanced dramatically.

For surface-enhanced Raman scattering to occur, the size of the features on the metal substrate must be small compared to the wavelength of the incident light [90]. If the size of the surface feature is similar or larger than the wavelength of the incident light, the incident electric field will excite not only dipolar plasmons but also multipoles. Unlike dipole, those multipolar modes are not efficient in exciting Raman scattering. Hence the

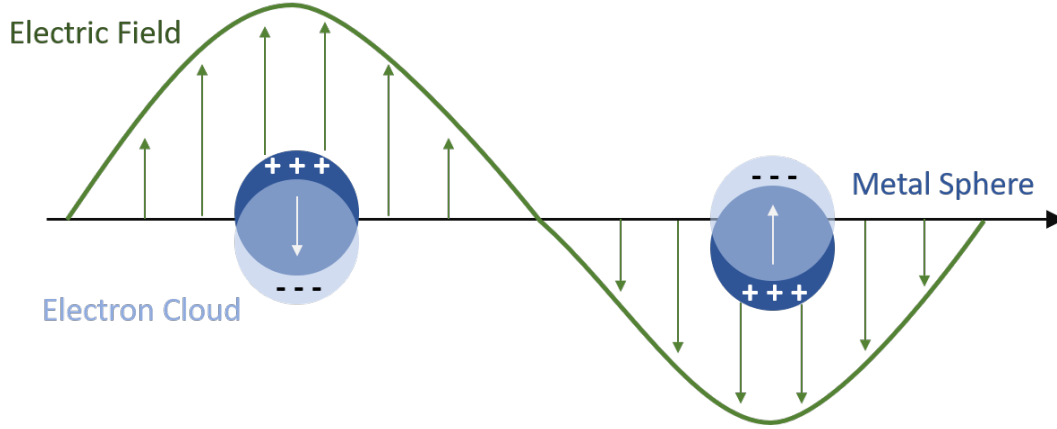


Figure 2.2: A localized surface plasmon. Reproduced from Ref [92]

SERS efficiency decreases. This suggests that the SERS-active surface should have the features in 5-100 nm scale.

It is commonly assumed that the factor of Raman scattering enhancement is equal to the fourth power of the local field enhancement factor [93]. Let us define a factor of the local field enhancement $M_{loc}(\lambda_0)$, therefore the local electric field E_{loc} :

$$E_{loc} = M_{loc}(\lambda_0)E_0 \quad (2.6)$$

where λ_0 is the wavelength and E_0 is the electric field of the incident light. Then the target molecule is excited by the enhanced field E_{loc} :

$$E_{scat} = \alpha E_{loc} = \alpha M_{loc}(\lambda_0)E_0 \quad (2.7)$$

where α is the polarizability of the target molecule. The molecule scatters at wavelength λ_R with Raman shift from λ_0 , and the scattered light is enhanced by E_{scat} :

$$E_{rad} = M_{rad}(\lambda_R)E_{scat} = \alpha M_{loc}(\lambda_0)M_{rad}(\lambda_R)E_0 \quad (2.8)$$

For a monochromatic propagating electromagnetic wave, the intensity is proportional to the square of the electric field:

$$I_{SERS} = M_{loc}^2(\lambda_0)M_{rad}^2(\lambda_R)I_0 \quad (2.9)$$

where I_0 is the intensity without local electric field enhancement. When λ_R is closed enough to λ_0 ,

$$\begin{aligned} M_{loc}(\lambda_0) &\approx M_{rad}(\lambda_R) \\ I_{SERS} &= M_{loc}^4(\lambda_0)I_0 \end{aligned} \quad (2.10)$$

Therefore, SERS enhancement is normally considered at fourth power of the local enhancement of the electric field.

The discovery of SERS makes it a sensitive tool for analyzing molecules at low concentrations. For a long period of time, SERS has almost exclusively been associated with three metals: silver, gold and copper [94–97]. Recently, SERS has also been observed on rhodium [98, 99] and platinum [100–102].

2.2 Differential Electrochemical Mass Spectroscopy

In electrochemistry, it is desirable to detect products formed at the electrode in real time. This is a difficult task because the rate of product generated on the electrode is comparatively small [103]. Bruckenstein and Gadde were the first to demonstrate online mass spectrometry in 1971 [104]. And it has been extended and perfected in the following works [105–107]. This technique is now commonly termed Differential Electrochemical Mass Spectrometry (DEMS) [108]. It employs differential sampling of the formed products and it utilizes a differential pumping system to remove most of the solvent species

so that the sampling gas pressure can fall in the operation pressure range of the mass spectrometry. In this thesis, we have successfully built a DEMS system following a design reported before [109–111] and detected the gaseous products of CO electrocatalytic reduction. In this section, we will introduce several key concepts of DEMS.

2.2.1 Viscous Flow and Molecular Flow

Before we begin to discuss viscous flow and molecular flow, we need to introduce one concept first: mean free path (λ). The mean free path of a gas molecule or atom is the average distance it travels before colliding with another molecule or atom [110]. The mean free path is inversely proportional to the density of the gas (thus pressure) and the cross-sectional area of the gas molecule/atom.

Viscous flow occurs when the mean free path of the gas molecule/atom is smaller than the characteristic dimension [110]. For a capillary tubing, its diameter (d) is the characteristic dimension. Viscous flow usually occurs when $d/\lambda > 100$. Molecular flow occurs when the mean free path of a gas molecule/atom is larger than the characteristic dimension. Usually molecular flow occurs when $d/\lambda < 1$. Once a specific gas is under molecular flow, then its flow rate is molecular mass dependent. The rate is proportional to $1/(M^{0.5})$, where M is the molecular mass of the gas molecule/atom. If the ratio of the characteristic dimension to the mean free path of the gas molecule/atom (d/λ) is between 1 and 100, then transition flow occurs. The flow regimes for gases are shown in figure 2.3.

During the sampling process, the composition of the gas may change compared to the original sample. This change is called fractionation [110]. Fractionation is mainly associated with the mass dependent flow. Viscous flow does not fractionate the sample gas, while molecular flow fractionates the sample gas in a predictable ratio. However, transition flow leads to uncertain fractionation.

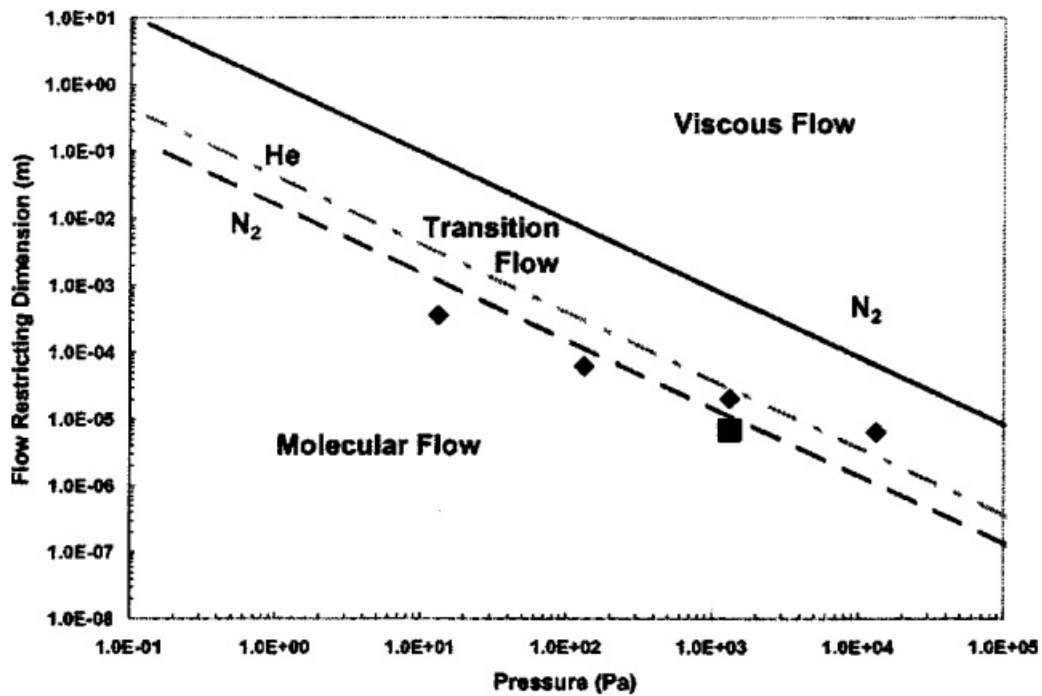


Figure 2.3: Flow regimes for gas flowing as a function of the gas pressure and flow-controlling dimensions. Reprinted with permission from [110]. Copyright [2007], American Vacuum Society.

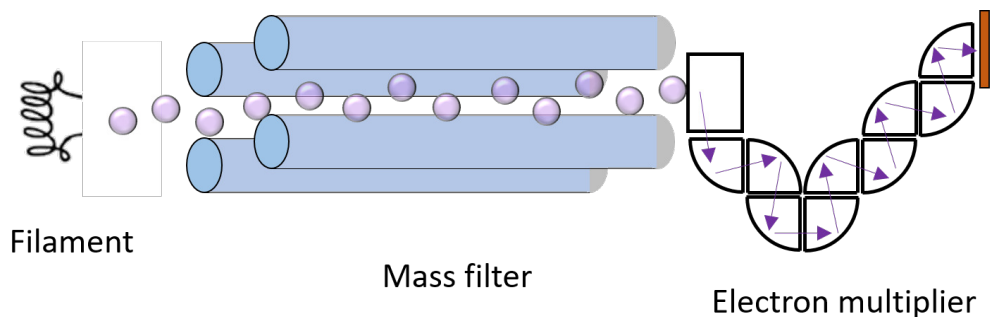


Figure 2.4: Sketch of the composition of a typical RGA.

2.2.2 Residual Gas Analyzer

The residual gas analyzer (RGA) is a small mass spectrometer that is typically used to analyze gaseous samples in vacuum. The key components of a RGA is shown in figure 2.4. Gas molecules/atoms will be ionized at the filament. Electron impact knocks off an electron and fragments molecules/atoms forming positive ions. Then the positive ions will be sorted by their mass/charge ratio in the quadrupole mass analyzer. The ion current passed the mass filter will be measured by Faraday cup coupled with an electron multiplier.

In this work, we used a Microvision 2 RGA (MKS; Andover, MA) with a standard open source. There are several operating parameters determining the measurement as listed in the following.

1. **Filament emission current (mA):** It is the flow of electrons emitted by the hot filament. This is normally maintained at a fixed value of 1 mA. The current flow through the filament will be increased until the value of emission current is reached.
2. **Electron Energy:** Electron energy for most efficient ionization is 70 eV. It will ionize almost all the molecules. However, it can produce doubly-ionized atoms such as Ar^{++} . Double ionization can be minimized by reducing the energy of the ionizing electrons, normally, 30-35 eV. Reducing the ionizing voltage also reduces the sensitivity.

3. **Ion Energy:** It is the kinetic energy of the ions as they enter the mass filter. Ion energy determines the time spent by the ions in the filter and hence, limits the resolution that can be obtained. The lower the energy, the better the mass resolution.
4. **Extractor Potential:** It is the negative potential of the focus plate. The focus plate is kept at a negative potential (relative to ground) and its function is to draw ions into the filter section.
5. **Faraday Cup:** Fast moving ions strike the cup cause a 'shower' of 'secondary' electrons. The use of the 'cup' rather than a plate, allows all electrons to be collected. Hence, one ion arriving at the Faraday cup needs one electron for neutralization but causes several electrons to be emitted. This provides amplification for each ion.
6. **Electron Multiplier:** It's a surface designed to generate secondary electrons. The ion impacts the surface generating 2 or 3 electrons each of which undergo further surface collisions generating more electrons, and so on in a cascade effect. Power for this cascade is provided by an applied voltage. A gain (ratio of output with multiplier to Faraday cup current) can be set to multiply the current got from Faraday cup.

For a RGA, we can use several following indicators to evaluate its performance.

1. **Basic Sensitivity:** It is defined with ampere/torr (A/Torr) at the Faraday cup. Typical range is 0.1 mA/Torr to 1 mA/Torr. This value can be tuned by calibration.
2. **Ultimate Sensitivity:** It is the sensitivity with A/torr after amplification by the electron multiplier. Ultimate sensitivity is equal to the basic sensitivity multiply electron multiplier gain. Gain depends on EM voltage and condition of multiplier active surfaces. Useful gain is limited by electronic noise. In our test, we usually have the sensitivity around 20 mA/torr.

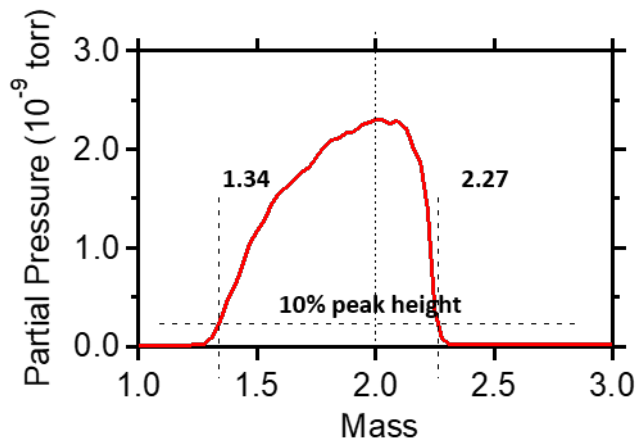


Figure 2.5: Peak shape of mass/charge ratio 2 with our RGA.

3. **Resolution:** It is defined as the peak width at 0.1 peak height above the baseline. Quadrupole mass spectrometer peaks are not symmetrical and have a longer ‘tail’ on the low amu side. As shown in figure 2.5, if we take the peak width at 10% of the peak height, it should fall into 1 amu range to avoid convolution with adjacent mass.
4. **Linearity:** The pressure range where the peak height is proportional to the partial pressure of the molecule. The response (peak height) as a function of partial pressure in our RGA becomes non-linear at pressures higher than 10^{-5} torr.
5. **Stability:** It is indicated by the change in peak height with time at a constant partial pressure. The change can be caused by thermal effects on electronics and mass filter, contamination on ionizer, rods or electron multiplier, aging of electron multiplier, and/or electronic drift. Usually a 30-minute warm-up is necessary for a good measurement. Therefore, we always keep the filament on 24/7 to achieve a stable baseline for routine measurements.

2.2.3 Differential Vacuum Stage

For the RGA to work properly, namely a linear response of ion current to partial pressure, the detection chamber needs to be kept below 5×10^{-5} torr. Then with a reasonable detection chamber diameter, it must be a molecular flow leaving the detection chamber. To avoid fractionation, a molecular flow going into the detection chamber is necessary. When the sample flows of both going into and out of the detection chamber are molecular flow, the concentration of the species in the detection chamber is the same as the original sample flow. Even though lower molecular weight species enter the detection chamber with a high rate, they also leave with the equally high rate. So there is no net change in the concentration of any species.

Therefore, with a ≈ 1 mm diameter tubing to introduce the sample gas flow, the pressure in the tubing should be under ≈ 0.1 torr to keep the molecular flow as figure 2.3 indicated. Differential pumping is designed to reduce the sample gas pressure down to a molecular flow pressure and then to the RGA working pressure. In addition, a needle valve or an orifice is commonly used to control the sample gas flow and guarantee a molecular flow into the detection chamber.

According to the need for the detection of the product from the electrode/electrolyte interface, we have designed and constructed the vacuum sampling system as shown in figure 2.6. The RGA sits in a stainless steel detection chamber. A hot cathode transducer (355 Micro-Ion; MKS; Andover, MA) is used to continuously monitor the pressure inside the detection chamber. The pressure inside the detection chamber is maintained by a combination pumping station incorporating a turbo pump and a diaphragm pump (HiCube 80 Eco; Pfeiffer Vacuum). With a typical pumping speed of 67 L/s, the pressure inside the detection chamber is kept around 10^{-5} torr during the measurement. The pressure of the pre-stage is controlled to be around 0.1 torr by a dry scroll pump (Edwards nXDS 6i;

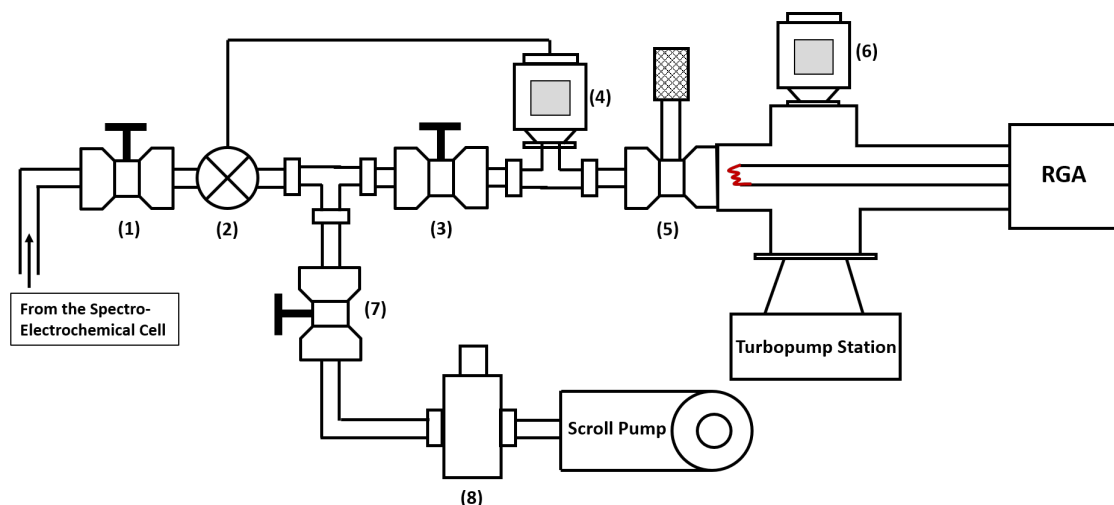


Figure 2.6: Scheme of the vacuum system. (1)(3)(7) Ball valve (2) Pneumatic valve (4)(6) Vacuum pressure transducer (5) Metering stem needle valve (8) Liquid nitrogen cold trap

Edwards Vacuum). A liquid nitrogen cold trap is used to protect the scroll pump from condensable water vapor. A pneumatic valve triggered by a vacuum pressure transducer is used to protect the RGA and turbo pump from any potential pressure rise due to leaks. Once the pressure reading on the transducer is higher than 20 torr, which indicates a leak, the transducer will trigger the pneumatic valve to close. Then the detection chamber will be isolated from the electrochemical cell.

2.2.4 Electrochemical cell for DEMS

For *in situ* detection of the product evolved from the interface of electrode/electrolyte, a specialized electrochemical cell needs to be employed. Following a design reported before [108, 109], we have made a one-compartment electrochemical cell with gas purging ports and a tip connected to the sampling vacuum system, as shown in figure 2.7. The sampling tip is made of a polyether ether ketone (PEEK) tube plugged by a porous polytetrafluoroethylene (PTFE) cylinder with a pore size of $\approx 10 \mu\text{m}$, a diameter of $\approx 3 \text{ mm}$, and a height of $\approx 2 \text{ mm}$ (Genuine Porex). To provide a watertight seal, the cylinder is

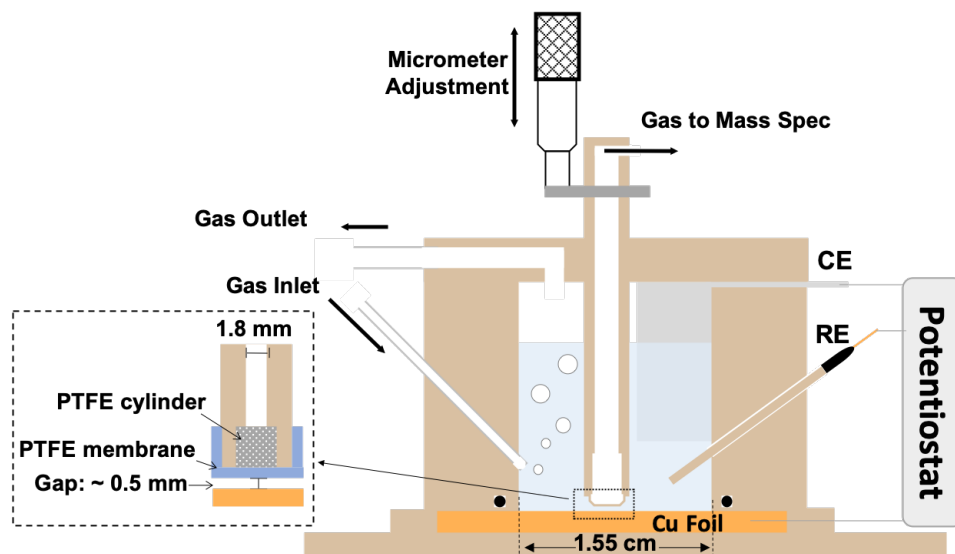


Figure 2.7: Electrochemical cell setup for DEMS.

epoxied into the PEEK tube. A PTFE membrane of 20 nm pore size (PF-002HS; Cobetter Laboratory) is wrapped around the PEEK tube/PTFE cylinder assembly and is fixated with epoxy and shrink tubing. The position of the sampling tip is controlled by a linear translation stage with micrometer adjustment. The sampling tip is positioned ≈ 0.5 mm above the electrode surface during the product detection.

To couple the product detection with infrared absorption spectroscopy and realize the detection of electrocatalytic activity and surface-adsorbed intermediates simultaneously, we have modified the electrochemical cell design as shown in figure 2.8. This setup allows conduction of DEMS and surface-enhanced infrared absorption spectroscopy (SEIRAS) on the same electrode simultaneously. The Cu film deposited on a Si ATR crystal is used as working electrode (WE). The sampling tip is positioned $\approx 100 \mu\text{m}$ above the electrode surface. An adjustable bellow is introduced for a smooth movement of the sampling tip.

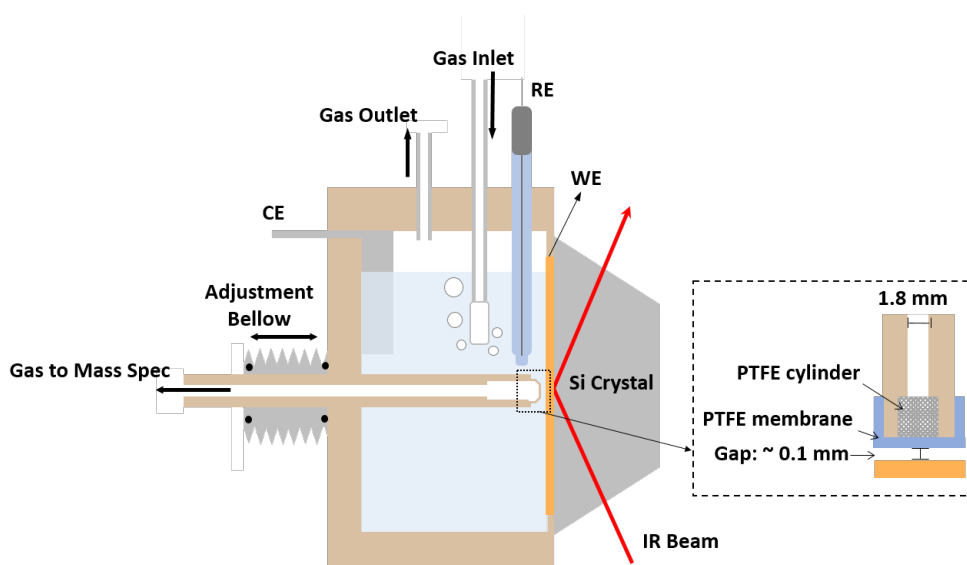


Figure 2.8: Electrochemical cell setup for DEMS and SEIRAS.

2.2.5 Time Constant for Sampling

The time constant is the delay from when the product is generated to when it is detected [110]. It includes: (1) diffusion time from the electrode surface to the sampling tip; (2) time delay as the sample is transported through the sampling vacuum system; (3) a delay dependent on the ion source, with an open ion source for our RGA, it is typical 0.1 s.

The time delay caused by the sampling vacuum system can be improved with the two stage pressure reduction [110]. From the electrochemical cell to the detection chamber, the pressure needs to be reduced to 10^{-5} torr. If the valve (7) as shown in figure 2.6 is completely closed, only the turbo pump station is used to drop the pressure of the sample gas. The sampling system is noted as single-stage pressure reduction. When the valve (7) is open, the scroll pump also contributes to reduce the pressure. The pressure is reduced in two steps. Most of the sample gas is drawn through the liquid nitrogen cold trap and evacuated by the scroll pump. A small fraction of the sample gas is split into the detection chamber. In this way, it is a two-stage pressure reduction. As shown in figure 2.9, the

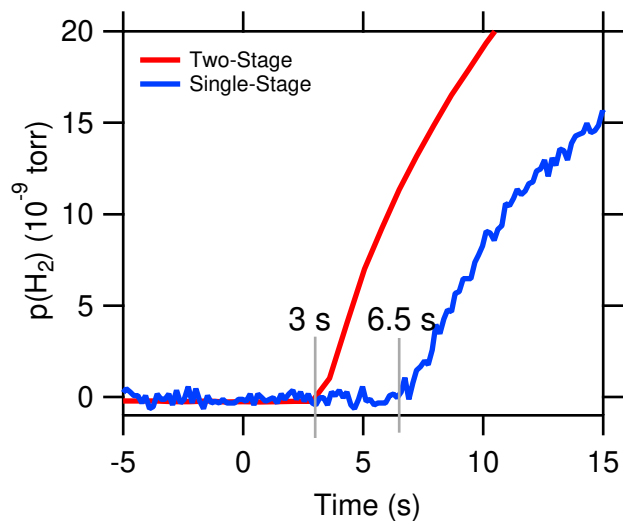


Figure 2.9: H_2 partial pressure measurement with the electrochemical cell shown in figure 2.7 with the sampling tip distance of $100 \mu\text{m}$. A cathodic potential drop was applied at time 0 s. Two-stage pressure reduction system shows better time constant compared to the single-stage.

two-stage pressure reduction system shows 3 s time constant for H_2 detection, while the single-stage pressure reduction system shows 6.5 s time constant. The bypass pumping in the two-stage pressure reduction system improves the time constant substantially by increasing the flow rate through the sampling system.

The time delay caused by the diffusion time from the electrode surface to the sampling tip can also be improved. The most straightforward way is to adjust the distance between the electrode surface and the sampling tip. As shown in figure 2.10, with decreasing tip distance, the time constant becomes smaller. With $20 \mu\text{m}$ tip distance, our DEMS can reach a time constant of 2.1 s for H_2 detection.

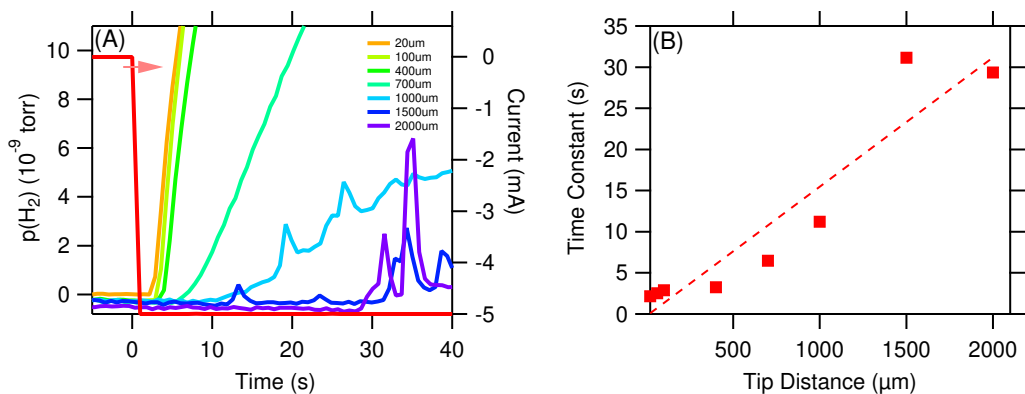


Figure 2.10: (A) H₂ partial pressure measurement with the electrochemical cell shown in figure 2.7. The tip distance is as indicated in the figure. A cathodic potential drop was applied at time 0 s. (B) The time constant got from (A) is plotted versus the tip distance and the linear fitting is also shown.

2.3 Electrochemistry

2.3.1 Rotating Disk Electrode

In 1950s, Levich first proposed the theory of a RDE (rotating disk electrode) based on the principle of hydrodynamics, which attracted widespread attention in the electrochemical community [112, 113]. RDE eliminates the limitation of mass transportation by rotation and it is more efficient than stirring. The electrode is cut and embedded in a holder, so that only the bottom end surface of the electrode is exposed to the electrolyte. The disk should be concentric with the axis of rotation, which has a good axial symmetry. Therefore, the RDE has a uniformly-accessible surface, meaning that all sites on the electrode surface have the same rate of mass transport.

The RDE should operate at a moderate speed. If it is too fast, turbulent flow will occur [114]. The Reynolds number, Re , is used to describe the character of the flow and

distinguish between laminar and turbulent flow [114]:

$$Re = \frac{\mathbf{v}l}{\nu} \quad (2.11)$$

where \mathbf{v} is the characteristic velocity, l is the characteristic length and ν is the kinematic viscosity. The critical Re is about 1×10^5 .

The characteristic velocity and length need to be defined depending on the geometry [114]. As for the RDE, the characteristic velocity is the linear velocity at the outer edge of the disk, $\mathbf{v} = \omega r$, where ω is the angular velocity. The characteristic length is the radius of the disk. At room temperature, the kinematic viscosity of a dilute solution is $\nu \approx 10^{-2} \text{ cm}^2/\text{s}$. Therefore, the condition for laminar flow is:

$$Re = \frac{\omega r^2}{\nu} \leq 1 \times 10^5 \quad (2.12)$$

For a typical disk with the diameter of 3 mm, ω should be less than $4.4 \times 10^4 \text{ rad/s}$, corresponding to a speed less than $4.4 \times 10^5 \text{ rpm}$. In the case mentioned above, Re represents an absolutely smooth surface. If the surface is rough, turbulence can occur at smaller values of Re . Therefore, the maximum speed of RDE is generally below 4000 rpm to ensure that it is in the region of laminar flow. However, if the speed of the RDE is too slow, natural convection can also disturb the flow. Therefore, it is typically operated above 400 rpm.

As shown in figure 2.11, the disk can drag the solution which is closest to it and impact its momentum in the tangential direction along the plane of the disk. As a result, the solution is pushed to the side of the disk. The gap left behind is filled by the bulk solution along a direction perpendicular to the disk. In this way, the solution near the surface keeps being refreshed by the new bulk electrolyte.

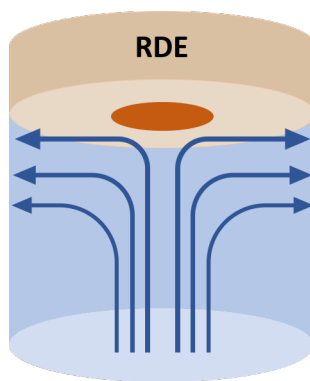


Figure 2.11: Motion of the solution at the surface of an RDE.

2.3.2 Tafel Analysis

In 1930s, English physical chemist John Alfred Valentine Butler and German physical chemist Max Volmer derived the basic equation describing electrode process kinetics, the ‘Butler-Volmer equation’ [113]:

$$j = j_0 \left\{ \exp\left(\frac{\beta F \eta}{RT}\right) - \exp\left[-\frac{(1 - \beta) F \eta}{RT}\right] \right\} \quad (2.13)$$

where j_0 is the exchange current density, β is the symmetry factor, F is the Faraday constant, and η is the overpotential. The exchange current represents the rate of forward as well as reverse reactions when the electrochemical reaction is at equilibrium. The Butler-Volmer equation contains both anodic and cathodic current density. When the cathodic overpotential is larger, the reduction current density is much larger than the oxidation current density. Therefore, the oxidation current density can be ignored, and vice versa. Normally, the anodic current density can be ignored when it is less than 1% to the cathodic

current density [115]:

$$\begin{aligned}\frac{e^{\beta F\eta/RT}}{e^{-(1-\beta)F\eta/RT}} &\leq 0.01 \\ e^{F\eta/RT} &\leq 0.01 \\ \eta &\leq \frac{RT}{F} \ln 0.01\end{aligned}\tag{2.14}$$

which implies the overpotential should be higher than 118 mV at 298 K.

We assume the anodic current density can be ignored, then the overpotential can be represented with:

$$|\eta| = \frac{RT}{(1-\beta)F} \ln j - \frac{RT}{(1-\beta)F} \ln j_0\tag{2.15}$$

when the temperature is 298 K, it can be simplified as:

$$|\eta| = \frac{0.059}{(1-\beta)} \log j - C\tag{2.16}$$

where C is a constant, $\frac{0.059}{(1-\beta)} \log j_0$. In an electrochemical experiment, the plot of the overpotential against $\log j$ is called Tafel plot. The above equation was derived for an outer-sphere one-electron transfer process. However, a Tafel plot can be generated even for multi-step, inner-sphere processes. In this case, the obtained slope from the plot is not necessarily related to the symmetry factor as in the equation above. However, the slope is then directly related to the transfer coefficient, which is a quantity that carries mechanistic information. For the Tafel analysis, the measured current must be free of mass-transport effects.

Chapter 3

Spectroscopic Observation of Reversible Surface Reconstruction of Copper Electrodes Under CO₂ Reduction Conditions

3.1 Introduction

In this chapter, using both surface-enhanced Raman (SERS) and attenuated total internal reflection Fourier-transform infrared (ATR-FTIR) spectroscopies, we report the first observation of reversible reconstruction of polycrystalline copper electrodes induced by carbon monoxide intermediately formed under conditions of CO₂ reduction. We find that copper electrodes reversibly form nanoscale clusters at potentials associated with significant carbon monoxide coverage. The formation of these clusters manifests itself both in terms of the appearance of a new carbon monoxide stretch band and a substantial intensity gain of the absorption bands of surface species. Our spectroscopic data suggests that CO binds to the newly formed clusters more strongly than to the sites available before reconstruction. As such a difference in binding energies, likely on the order of a fraction of an electron-volt, is expected to greatly affect the electrocatalytic properties of copper, we believe that this first documentation of reversible surface reconstruction of copper under conditions of electrocatalytic CO₂ reduction to be essential for the correct interpretation of a wide range

of electroanalytical studies of this important prototype catalyst.

3.2 Results

3.2.1 ATR-FTIR Spectra of CO on Cu Thin Films

As CO is an on-pathway intermediate in the reduction of CO₂ [71, 72, 116, 117], initial experiments were carried out in 0.1 M KHCO₃ saturated with pure CO gas. Figure 3.1 shows a series of infrared (IR) spectra in the C≡O stretch region of atop-bound CO of a copper thin film electrode. At moderate cathodic potentials in the range of ≈ -0.5 to -0.7 V vs SHE, the spectra exhibit a single symmetric peak at ≈ 2050 cm⁻¹. An additional, relatively narrow band develops at ≈ 2080 cm⁻¹ starting at ≈ -0.8 V. As shown in Figure 3.1, the observed spectra are well described by a model consisting of a linear combination of a symmetric and a slightly skewed Gaussian function. In the following, the two bands are referred to as the “low frequency band” (LFB) and the “high frequency band” (HFB).

As shown in Figure 3.2, the integrated area of the LFB gradually increases with increasing cathodic potential over a wide voltage range (≈ 0.5 V). By contrast, the HFB exhibits a distinctly sharp increase in integrated area over a narrow potential span of ≈ 0.15 V.

The IR spectra discussed so far were sequentially collected in the direction of increasing cathodic potential (arrows, Figure 3.2). To test if the growth of the HFB is reversible after the spectrum at the most cathodic potential of -1.10 V was recorded, we collected additional spectra at selected potentials by stepping the potential backward, i.e., in the anodic direction. Figure 3.3A compares three representative spectra collected before the most cathodic potential was reached (left side) with corresponding spectra recorded afterward (right side). The similarity between the two sets of spectra proves that growth and

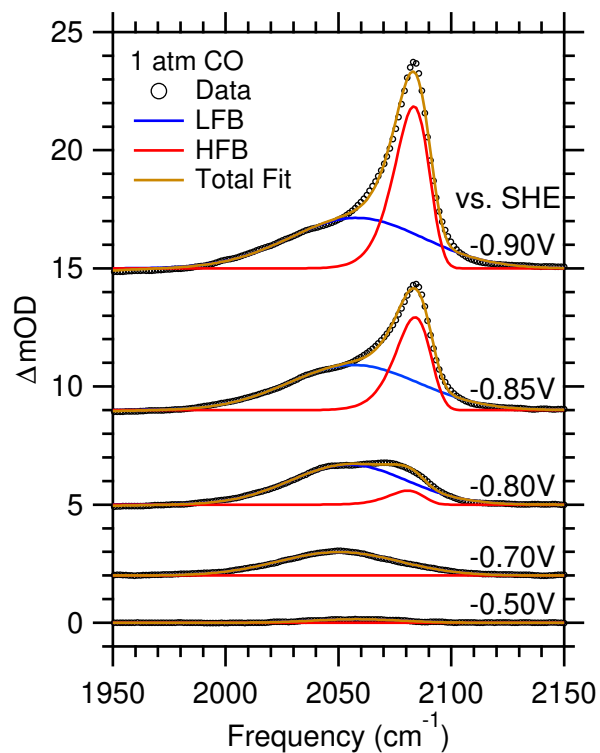


Figure 3.1: Dependence of the IR spectrum in the C≡O stretch region on applied potential.

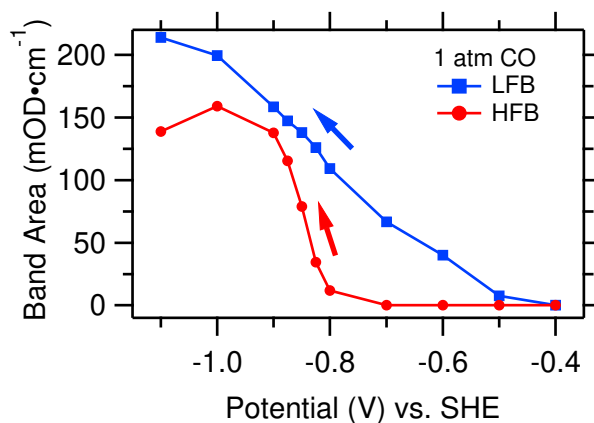


Figure 3.2: Dependence of the integrated areas of the LFB and HFB on applied potential.

decline of the HFB are reversible. The corresponding integrated areas of the bands are shown in Figure 3.3B.

To gain further insights into the interfacial processes, we analyzed the desorption of anions from the electrode. With increasing cathodic potential, CO_3^{2-} and HCO_3^- ions, which are specifically adsorbed on the surface at low cathodic potentials, gradually desorb from the electrode, leading to a loss of absorbance at $\approx 1540 \text{ cm}^{-1}$ (Figure 3.4A). Figure 3.4B shows the potential dependence of the integrated band area of these ions. It has previously been shown that carbonate and bicarbonate ions are displaced by CO with increasing cathodic potential [118]. Assuming that Beer's law holds, the integrated areas of the spectra in the $\text{C}\equiv\text{O}$ stretch region should be directly proportional to the CO surface coverage. With this assumption, inspection of Figure 3.4C reveals that the total CO population (proportional to the sum of the LFB and HFB) approximately doubles as the potential is stepped from ≈ -0.8 to $\approx -0.95 \text{ V}$ due to the sharp rise of the HFB. Surprisingly, the steep increase in the CO population is not mirrored in a corresponding change in the carbonate desorption curve, which closely tracks the curve of the LFB.

Next, we carried out experiments in 0.1 M KHCO_3 saturated with CO_2 , where surface-adsorbed CO is produced via the reduction of CO_2 at the copper electrode. As in the experiment with pure CO atmosphere, a single Gaussian band gradually appears at moderate cathodic potentials, followed by the development of a narrow band that sharply increases over a small potential range (Figure 3.5). In Figure 3.6, the potential dependencies of the LFB and HFB observed under these conditions are compared to the experiments in pure CO atmosphere. Irrespective of how the surface-adsorbed CO is produced, i.e., by direct adsorption from the electrolyte with 1 atm CO as in the previous experiment or via the electrochemical reduction of CO_2 in 1 atm CO_2 , the LFB acquires a significant integrated band area of $\approx 100 \text{ mOD}\cdot\text{cm}^{-1}$ at the onset potential of the HFB as indicated by the shaded areas in Figure 3.6. Similar results are obtained when carrying out the experiment

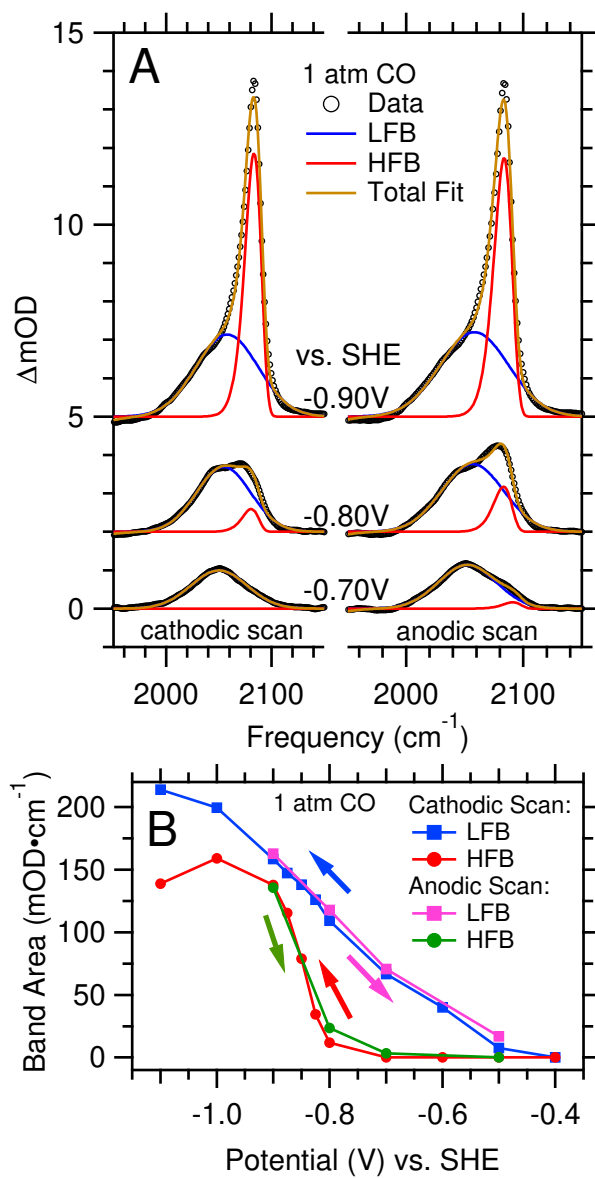


Figure 3.3: (A) Representative spectra collected by stepping the potential in cathodic direction (cathodic scan) and the corresponding spectra recorded after the most cathodic potential (-1.10 V) was reached (anodic scan). (B) Integrated band areas derived from the spectra shown in part A, anodic scan, plotted together with the data from Figure 3.2

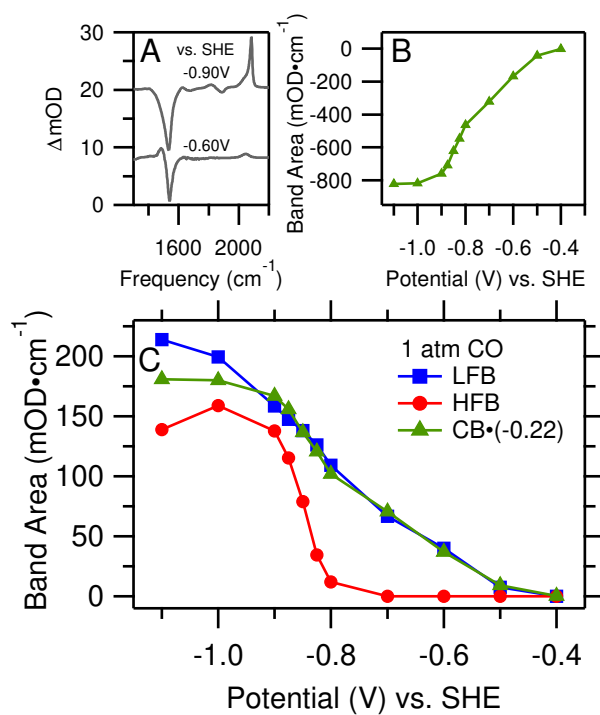


Figure 3.4: (A) Representative spectra showing the loss of absorbance at $\approx 1540 \text{ cm}^{-1}$. (B) Integrated band area of the carbonate band as a function of potential. (C) Comparison of the scaled carbonate band (CB; scaling factor: -0.22) with the corresponding curves of the LFB and HFB.

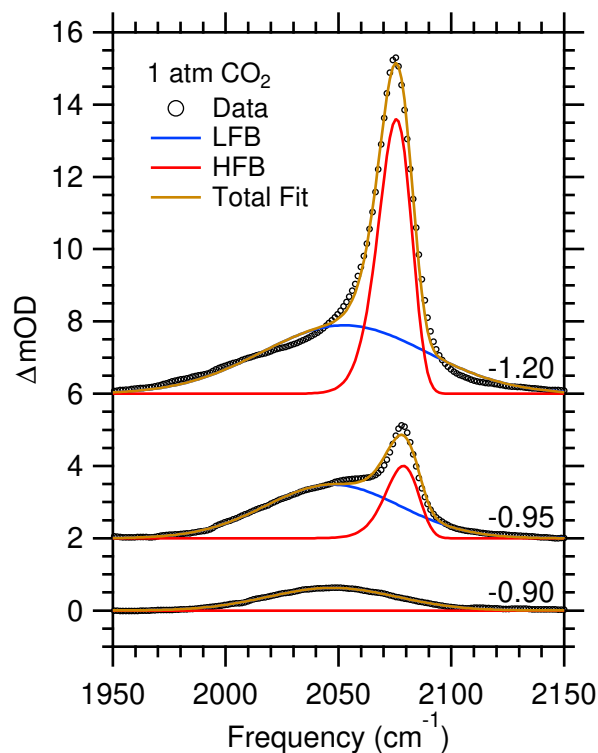


Figure 3.5: Dependence of the spectral lineshape in the C≡O stretch region on applied potential. Values in the figure denote potential in volts vs. SHE.

at reduced partial pressure of CO (Figure 3.7).

3.2.2 SERS Spectra of CO on Cu Foils

To further investigate the spectral lineshapes, we carried out surface-enhanced Raman spectroscopy on Cu foils in 0.1 M KHCO₃ saturated with CO₂ under reduction conditions. Figure 3.8 shows Raman spectra in the frequency region of 240-430 cm⁻¹, where bands associated with metal-adsorbate interactions appear, and the spectra concurrently collected in the C≡O stretch region (1920-130 cm⁻¹). In agreement with our IR studies, Raman spectra in the C≡O stretch region exhibit similar spectral features and potential dependence. A key observation is the simultaneous appearance of the HFB at ≈ 2080 cm⁻¹ and the two bands at 280 and 360 cm⁻¹ (Figures 3.8 and 3.9).

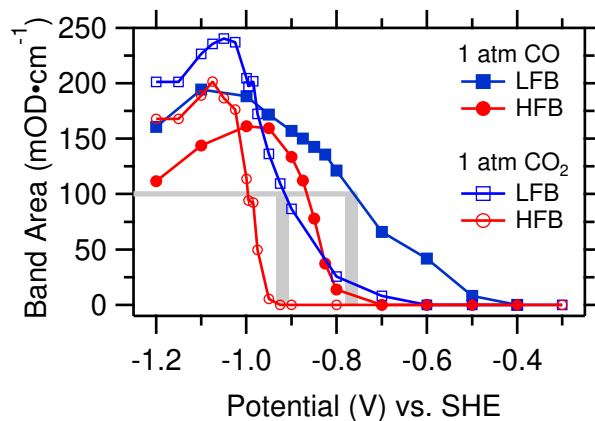


Figure 3.6: Areas of the LFB and HFB in 1 atm CO (solid symbols) and 1 atm CO₂ (open symbols).

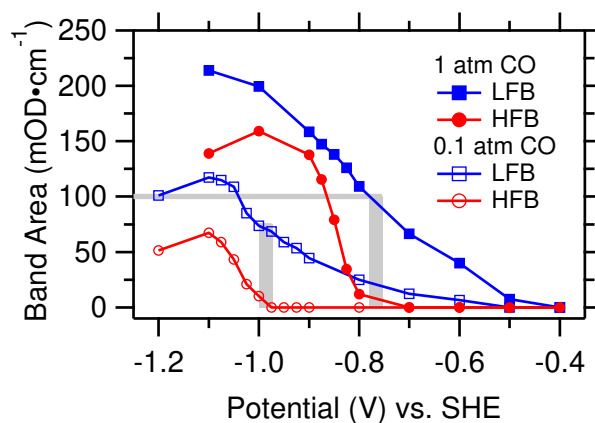


Figure 3.7: Dependence of the band areas on potential at different partial pressures of CO. The reduced partial pressure data was collected using a 1:9 mixture of CO and Ar. In both cases, the LFB acquires a substantial integrated area of ≈ 75 -100 mOD·cm⁻¹ at the onset potential of the HFB.

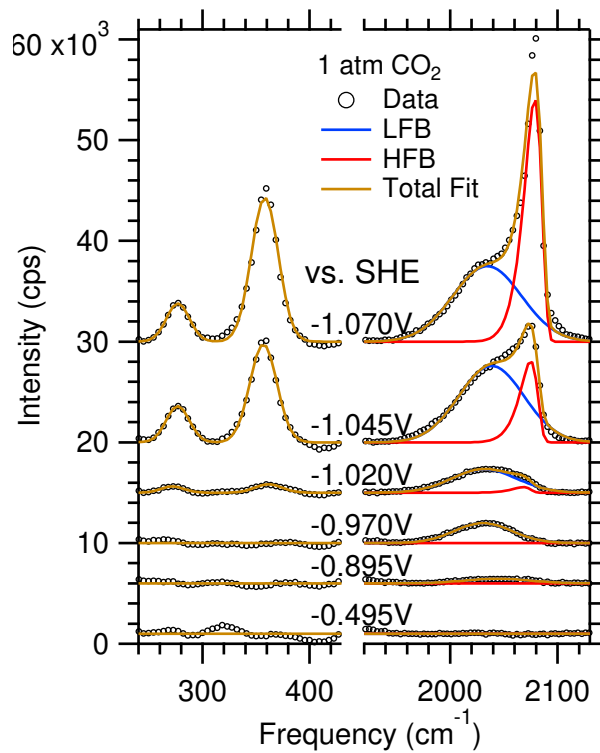


Figure 3.8: Dependence of the Raman spectrum on applied potential.

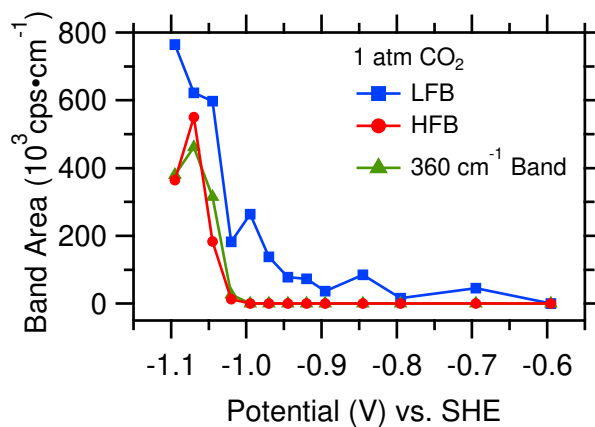


Figure 3.9: Potential dependencies of the areas of the bands shown in Figure 3.8

3.2.3 Time-Resolved ATR-FTIR Spectra of CO on Cu Thin Films

To further investigate the dependence of the spectral lineshape on catalytic conditions, we performed time-resolved IR measurements of the two bands in the C≡O region by stepping the potential from -0.70 to -1.10 V. Upon this potential step, the electrocatalytic reduction of CO₂ to CO is activated and CO accumulates on the electrode surface. The time evolution of the spectral line shape is shown in Figure 3.10A. It is evident that the LFB is exclusively present at times <0.4 s, but the HFB develops into a prominent feature in the following 0.5 s. The time dependencies of the integrated band areas are shown in Figure 3.10B. The LFB's trace is well described by a double exponential fit with a fast ($\tau \approx 0.3$ s) and slow phase ($\tau \approx 1.3$ s). By contrast, the HFB's trace is well modeled by a single exponential fit with a time constant of $\tau \approx 1.3$ s and a temporal offset of ≈ 0.4 s (gray shaded area, Figure 3.10B). The fits reveal that the two bands evolve with comparable kinetics ($\tau \approx 1.3$ s) following the initial period of ≈ 0.4 s. This observation implies that the band areas are linearly dependent:

$$A_{\text{HF}} = m(E, \theta) \times A_{\text{LF}} - b \quad (3.1)$$

where A_{HF} and A_{LF} represent the integrated areas of the HFB and LFB, respectively. The factor $m(E, \theta)$ depends on the applied potential, E , and CO surface coverage, θ ; b is a constant. The inset of Figure 3.10B shows A_{HF} offset by $b = 100$ mOD cm⁻¹ and multiplied by $m = 1.4$.

3.2.4 Reproducibility

Finally, we note that the ATR-FTIR data exhibit good quantitative agreement between repeated measurements (Figures 3.11 and 3.12). While the SERS spectra of repeated

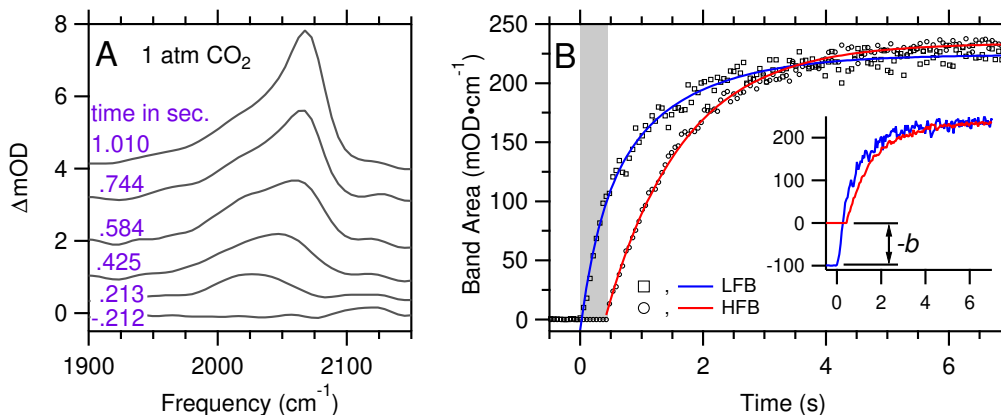


Figure 3.10: (A) Time evolution of the spectrum following a potential step from -0.70 to -1.10 V vs SHE. (B) Kinetics of the integrated areas of the LFB and HFB. The gray shaded area highlights the period in which the HFB is absent. The lines indicate double and single exponential fits to the LFB and HFB, respectively. The inset shows the LFB offset by $b = 100 \text{ mOD cm}^{-1}$ and multiplied by $m = 1.4$.

experiments show quantitative differences, the trends shown in Figures 3.8 and 3.9 are highly reproducible (Figure 3.13).

3.3 Discussion

3.3.1 Assignment of Bands

The observed peaks can be readily interpreted by comparison with Raman and infrared spectroscopic studies of CO adsorbed on single and polycrystalline copper surfaces in ultrahigh vacuum and electrochemical environments. We will first assign the metal-adsorbate bands observed at ≈ 360 and 280 cm^{-1} before discussing the bands found in the intramolecular stretch region.

Using the isotope labeling technique, the infrared spectroscopic study of CO on Cu(100) by Hirschmugl et al. assigned peaks at ≈ 345 and 285 cm^{-1} to the Cu-CO stretch and the frustrated rotation of the CO molecule bound in an atop geometry, respectively [119]. Similarly, the Raman spectroscopic study of CO on disordered Cu films by Akemann et

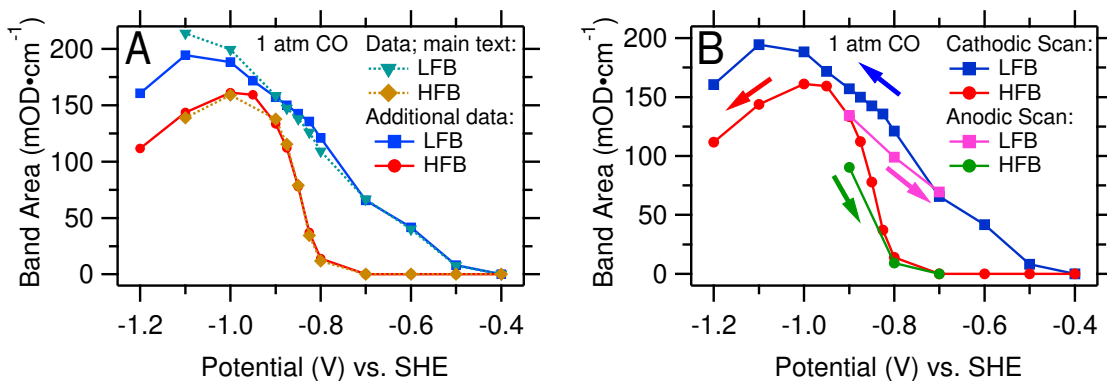


Figure 3.11: (A) Comparison of the data presented in Figure 3.2 with another data set collected on a separately prepared thin film (shown in Figure 3.6), illustrating the high reproducibility of the data. (B) Reversibility of the lineshape changes of the additional data set presented in (A).

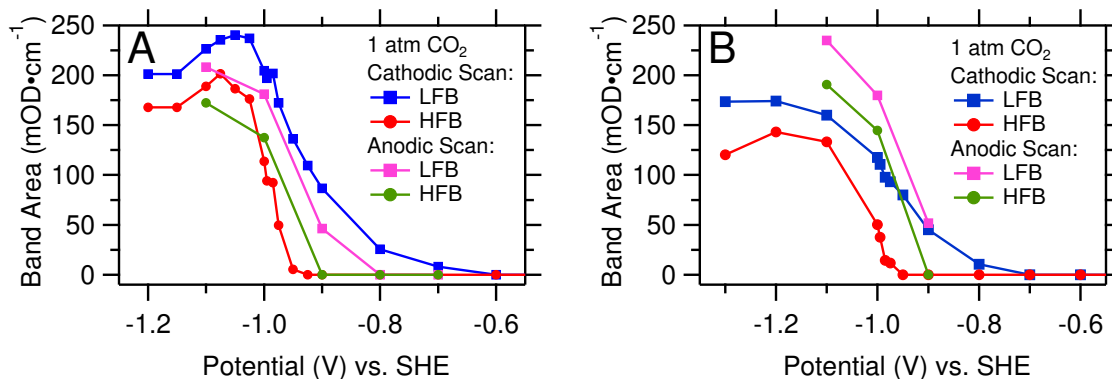


Figure 3.12: (A) Reversibility of the spectral lineshape changes under CO₂ atmosphere for the data presented in Figure 3.6. (B) Additional data set collected on a separately prepared thin film. The slight hysteresis observed in CO₂ atmosphere is attributed to the relatively high cathodic potentials which exert stress on the copper films.

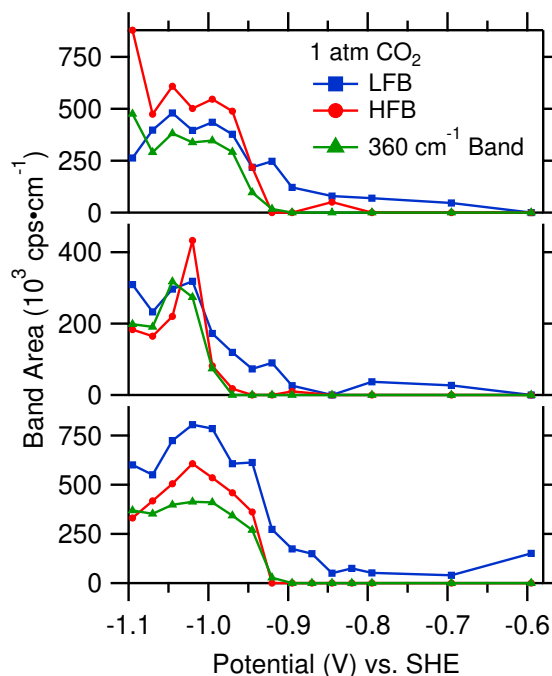


Figure 3.13: Illustration of reproducibility of the potential dependencies of the band areas derived from Raman spectra. Each panel represents a data set collected on a different day.

al. revealed peaks at ≈ 358 and 280 cm^{-1} [120]. The surface-adsorbate related bands at ≈ 360 and 280 cm^{-1} in our spectra are therefore ascribed to the Cu-CO stretch and the frustrated rotational mode of CO, respectively.

At the gas/copper interface, it is well-established that atop-bound CO on terraces produces a C \equiv O stretch band $\approx 30 \text{ cm}^{-1}$ lower than CO adsorbed on undercoordinated defect sites [121, 122]. Therefore, the stronger binding of CO to copper defect sites [123] (compared to terrace sites) leads to a blue-shift of the vibrational frequency of CO [81, 121, 122]. We note in passing that the opposite is the case for the more commonly studied platinum surface [122]. A blue-shift of the vibrational frequency of CO with increased binding strength to Cu atoms is also predicted by theory [124]. In agreement with studies at the gas/copper interface, spectroelectrochemical studies on monocrystalline copper electrodes under cathodic potential by Hori et al. found a CO stretch band at $\approx 2075 \text{ cm}^{-1}$ on stepped copper surfaces [125] and a band at $\approx 2055 \text{ cm}^{-1}$ on Cu(100) [118]. Therefore,

we can confidently assign the HFB to CO adsorbed on undercoordinated defect sites and the LFB to CO adsorbed on sites with a comparatively higher degree of coordination.

3.3.2 Interpretation of Data in Terms of Surface Reconstruction

The potential dependencies of the bands can be fully explained by the following hypothesis: With increasing cathodic potential, the CO coverage on the surface monotonically increases as evidenced by the gradual rise of the LFB (Figure 3.2). Once a certain threshold coverage is reached, the interaction of CO with the substrate induces a reconstruction of the surface, leading to the formation of CO-stabilized copper clusters containing undercoordinated copper atoms. CO bound to these undercoordinated sites gives rise to the new HFB.

Our hypothesis, which is in agreement with the recent observation of surface reconstruction at the gas/copper interface [80, 81], is supported by the following observations: First, the physical origin of the linear relationship between the two bands as expressed by equation 3.1 is now apparent. In the time-resolved experiments, CO₂ reduction is activated by stepping to the reaction potential. Following this step, the CO coverage on the surface gradually rises as a function of time as evidenced by the appearance of the LFB at early times (gray shaded area, Figure 3.10B). Once the threshold CO coverage is surpassed, CO-induced surface reconstruction takes place. The constant $b \approx 100 \text{ mOD cm}^{-1}$ is the integrated area of the LFB at the threshold coverage. From this time on, the HFB develops and reaches a prominence proportional to the factor $m(E, \theta)$, which describes the degree of surface reconstruction. The linear model, equation 3.1, also describes the steady-state potential dependencies of the bands (Figure 3.2). Because the undercoordinated sites, associated with the HFB, are created only after the threshold coverage is surpassed, the absence of a corresponding CO stretch band at moderate potentials naturally follows.

Second, the hypothesis explains why the carbonate desorption curve does not mirror

the sharp rise of the HFB (Figure 3.4). The surface reconstruction exposes additional copper atoms to the electrolyte, i.e., new adsorption sites are created. Because these newly created sites were not previously occupied by carbonate ions, CO adsorbing on these newly created sites does not displace carbonate ions.

Third, our hypothesis explains the sharp intensity increase that all Raman bands experience as the potential is tuned more cathodic than ≈ -1.0 V (Figures 3.8 and 3.9). At potentials above ≈ -1.0 V, the CO coverage on the electrode is below the threshold coverage of surface reconstruction. However, once reconstruction occurs, all bands are substantially enhanced due to the formation of nanoscale Cu clusters, which render the surface more favorable for SERS [91]. It is important to note that the enhancement is not restricted to the C \equiv O stretch band, but the ≈ 360 and 280 cm^{-1} bands experience a concurrent enhancement. Indeed, the enhancement of the spectral features in the Raman spectra is not restricted to CO-related bands. A hydrocarbon band in the 2800 - 3000 cm^{-1} region, not related to a species produced in the process of CO $_2$ reduction but arising from adsorption of an exogenous species, is also strongly enhanced (Figure 3.14), which is readily explained by the reconstruction process. We emphasize that this observation strongly speaks against alternative interpretations in terms of other mechanisms, such as dipole-dipole coupling or the Stark effect, as explained in the next section.

The spectral widths of the two bands, measures of surface heterogeneity, are also consistent with our interpretation. On the polycrystalline electrode, various crystallographic planes are exposed to the electrolyte, giving rise to the relatively broad width of the LFB. While our data admittedly do not report on the shape of the nanoscale metal clusters, the relatively narrow width of the HFB suggests that the formed clusters contain Cu atoms with comparable degrees of undercoordination. This notion is in line with the recent observation of the formation of well-defined nanoscale clusters at the CO gas/copper interface [80]. Our interpretation is further supported by the remarkable resemblance of our

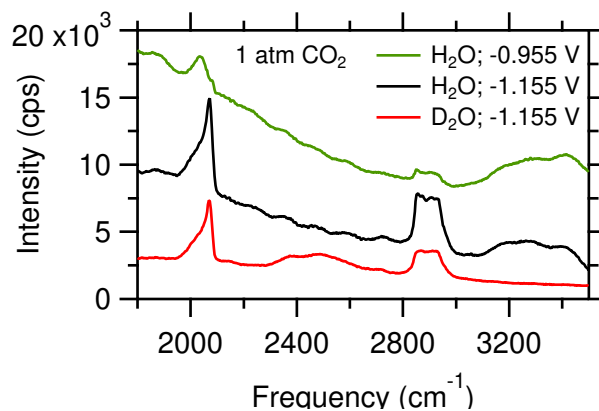


Figure 3.14: Comparison of Raman spectra collected in D_2O and H_2O . The absence of an isotope shift for the hydrocarbon band ($2800\text{-}3000\text{ cm}^{-1}$) indicates that the band is not related to the reduction reaction, but due to adsorption of an exogenous species. The enhancement of this band at more cathodic potentials is explained by the reconstruction process. Values in the figure denote potential in volts vs. SHE.

infrared spectra with the temperature-programmed desorption profiles obtained from desorption of CO from polycrystalline copper [65].

3.3.3 Consideration of Alternative Interpretations

Finally, we note that we can exclude the possibility that the lineshape changes arise from other species and/or mechanisms. The bands do not exhibit an isotopic shift when the experiments are carried out in deuterated electrolyte and therefore do not arise from the Cu-H stretch (Figure 3.14) [126]. They are further absent in He-purged electrolyte. Other surface intermediates formed during CO_2 reduction, such as CHO, COH, OCCO, or OCCOH, are expected to absorb below 1800 cm^{-1} [117, 127], and theory predicts extremely low surface populations for these species [128]. Other mechanisms, such as a Fano resonance or dipole-dipole coupling can also be excluded: The shapes of the observed spectra are inconsistent with the range of lineshapes that are expected from a Fano resonance [129]. While dipole-dipole coupling leads to a growth of a high frequency band at the expense of a low frequency band, the total integrated band area remains conserved [122]. Inspection

of Figure 3.2 reveals that the sharp rise of the HFB does not affect the monotonic increase of the LFB. If dipole-dipole coupling were a significant factor in the rise of the HFB, the growth rate of the LFB would decrease, which is not observed. This finding is also not readily rationalized in terms of mechanisms that modulate the vibrational frequency, such as the Stark effect or interactions between CO and coadsorbed hydrogen [130, 131]. Moreover, both mechanisms do not easily explain why the hydrocarbon band at 2800-3000 cm^{-1} (Figure 3.14), arising from adsorption of an exogenous species, is strongly enhanced in the presence of CO or why the Cu-CO stretch experiences a marked intensity gain concurrent with the appearance of the HFB (Figures 3.8 and 3.9). In summary, while other theories fail to describe the entire collection of observations presented herein, our hypothesis of reversible surface reconstruction provides a coherent picture that fully explains all our experimental findings.

3.4 Conclusions

Taken together, our data provide strong evidence of CO-induced surface reconstruction that leads to the formation of nanoscale clusters of copper on the catalytic surface. To the best of our knowledge, this is the first observation of reversible surface reconstruction on a copper electrode under catalytic conditions. We note that the two electrodes investigated here (thin copper film in ATR-FTIR and roughened copper foil in SERS experiments) were sourced and prepared entirely differently. Irrespective of their differences, both behave in a similar manner. Indeed, the two $\text{C}\equiv\text{O}$ stretch bands were previously observed in a number of studies of polycrystalline electrodes [72, 117, 132–134] but were collectively analyzed. These observations strongly suggest that reversible reconstruction occurs in a wide range of differently prepared copper electrodes. Other *in situ* techniques, such as X-ray absorption spectroscopy [135], could be useful for further elucidating the recon-

struction process. The difference in the vibrational frequencies of the two C≡O stretch bands of $\approx 30 \text{ cm}^{-1}$ suggests substantially different binding strengths of CO adsorbed on the two distinct types of sites, likely on the order of a fraction of an electronvolt [65, 71, 136]. As such a significant difference is expected to have profound effects on the catalytic properties of the electrode, the process of surface reconstruction needs to be considered in future investigations of this important prototype catalyst.

3.5 Experimental Procedures

3.5.1 Materials for Cu Thin Film Preparation

NH₄F (40 wt.% in H₂O) and HF (48 wt.%) were purchased from Fisher Scientific. CuSO₄·5H₂O (99.999%; trace metals basis), Na₂EDTA (99.0-101.0%; ACS Reagent), 2,2-bipyridine ($\geq 99\%$; ReagentPlus), HCHO (35 wt.%; 10% methanol as stabilizer), NaOH (99.99%; trace metals basis), and KHCO₃ ($\geq 99.95\%$; trace metal basis) were acquired from Sigma Aldrich.

3.5.2 Materials for Electrode Preparation and Spectro-Electrochemical Measurements

Polycrystalline diamond pastes and alumina slurries were procured from South Bay Technologies (San Clemente, CA) or Electron Microscopy Sciences (Hatfield, PA). High purity water (18.2 M Ω cm) derived from a Barnstead Nanopure Diamond system (APS Water Services; Lake Balboa, CA) was used for all experiments. Potassium bicarbonate ($>99.95\%$ trace metal basis, 99.7-100.5% dry basis) was obtained from Sigma Aldrich. Phosphoric acid (85%; TraceSELECT; Fluka) was acquired from Fisher Scientific. He (Ultra High Purity), CO (99.999%), CO₂ (5.0 research grade) were purchased from Air

Gas.

3.5.3 Preparation of Cu Thin Films

Cu thin films were prepared by an electroless plating procedure [117, 134]. The reflecting plane of a 60° Si prism (Pike Technologies; Madison WI) was sequentially polished with 6, 1, and 0.5 μm diamond pastes for 10-15 min each to reveal a fresh Si layer. The crystal was then rinsed in a constant stream of Nanopure water for 5-10 min while rubbing it with a wet Kim-wipe. Following sequentially sonication in water, acetone, and water for 5-10 min each, the Si surface was etched by immersing the reflecting plane of the prism in an aqueous solution of 40 wt.% NH_4F (25°C) for 30 s. After etching, the prism was rinsed with water and the reflecting surface was brought into contact with a 0.5 wt.% HF seeding bath containing 750 μM CuSO_4 (25°C) for 1.5 min. The Cu-seeded surface was gently rinsed with water and immersed into a plating bath (0.25 M HCHO, 0.02 M CuSO_4 , 20 mM Na_2EDTA , and 0.3 mM 2,2-bipyridine; pH 12; T = 54-55°C) for 3.5 min. The plating bath was prepared as follows. Solutions of HCHO, CuSO_4 , and $\text{Na}_2\text{EDTA}/2,2\text{-bipyridine}$ adjusted to a pH of 12 with NaOH were prepared in separate vials. The latter solution (5 mL) was dropwise added to a 10 mL 1:1 mixture (by volume) of the two former ones and diluted to a total volume of 25 mL to give the desired final concentrations given above. The pH of the plating bath was readjusted to 12 with NaOH. Following the deposition, the resistance across the film surface was measured to be 10-30 Ω . The cell was then immediately assembled and the copper film was blanketed with 4 ml of 0.1 M KHCO_3 electrolyte. The film was subjected to cleaning voltammetry cycles from -0.035 to -0.605 V vs. Ag/AgCl at a scan rate of 0.05 V s^{-1} in He saturated electrolyte for a total of three cycles. A representative cyclic voltammogram in CO_2 saturated electrolyte is shown in Figure 3.15. In good agreement with previous reports [117], capacitance measurements revealed a film roughness factor of about 10-12.

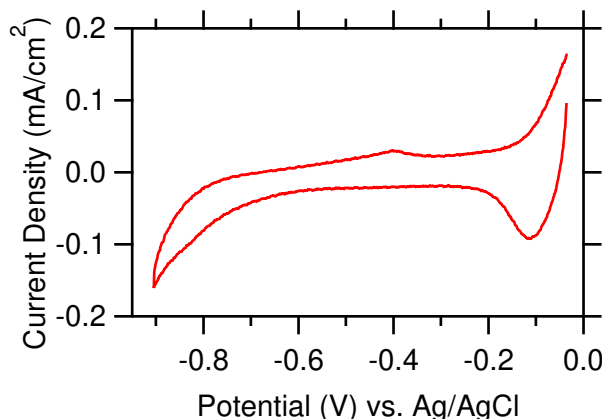


Figure 3.15: Cyclic voltammogram (50 mV s^{-1}) of a copper thin film in CO_2 saturated 0.1 M KHCO_3 . The geometric area of the electrode was $\approx 1.9 \text{ cm}^2$

3.5.4 ATR-FTIR Measurements

ATR-FTIR spectra were recorded in the Kretschmann configuration with a nitrogen-purged Bruker Vertex 70 FTIR spectrometer (Billerica, MA) equipped with an MCT detector (FTIR-16; Infrared Associates; Stuart, FL). The FTIR instrument was interfaced with an ATR accessory (VeeMax III; Pike Technologies; Madison, WI) equipped with a customized electrochemical cell machined from PEEK. Steady-state measurements were collected at 4 cm^{-1} spectral resolution and a 40 kHz scanner velocity. For each reported spectrum, a single beam reference spectrum was first collected at -0.505 V (CO) or $-0.405 \text{ V (CO}_2)$ vs. Ag/AgCl. Following collection of the single beam reference spectrum, the potential was decreased to the sample potential at a rate of 0.01 V s^{-1} . To ensure steady-state conditions, the target potential was held for 60 s before collection of a single beam spectrum. The change in optical density was calculated according to $\Delta\text{mOD} = -10^3 \times \log(\text{SB}_S/\text{SB}_R)$, where SB_S and SB_R represent the single beam spectra at the sample and reference potentials, respectively.

Rapid-scan FTIR measurements were carried out with a resolution of 16 cm^{-1} and a scanner velocity of 160 kHz (time resolution $\approx 0.053 \text{ s}$). After the reference potential was

applied for 60 s, a step to the sample potential was triggered by the forward-motion of the interferometer mirror. Acquisition of spectra was initiated a few hundred milliseconds before the potential step. The first spectrum collected at the reference potential was used as the reference.

All measurements were carried out in 0.1 M KHCO_3 electrolyte at room temperature. Constant flow (2-5 sccm) of CO or CO_2 gas was maintain throughout the experiment with mass flow controllers (GE50A; MKS; Andover, MA).

3.5.5 Electrochemical Methods for ATR-FTIR Measurements

Experiments were carried out in a three electrode cell with a leakless Ag/AgCl reference electrode (ET072-1; eDAQ, Colorado Springs, CO) and a Pt wire (99.95%; BASi Inc.; West Lafayette, IN) as the counter electrode. The Ag/AgCl electrode was regularly calibrated against a saturated calomel electrode (CHI 150; CH Instruments Inc.; Austin, TX). Prior to each experiment the cell was cleaned in an aqueous acid solution (30 wt.% H_2SO_4 , 30 wt.% HNO_3) for one hour; then sonicated in Nanopure water for another hour. The uncompensated resistance of the cell was found to be negligible as determined by the VersaStudio software of the VersaStat3 potentiostat (AMETEK; Berwyn, PA).

3.5.6 Preparation of the Raman-Active Surface

Cu foil (1.0 mm thickness; Puratronic 99.999% metals basis) was purchased from Alfa Aesar. The copper electrode surface was prepared by consecutive polishing with 1000 grit sand paper (5 min), 1, and 0.3 μm alumina slurries (10 min each), followed by sequential sonication in acetone (5 min) and deionized water (5 min). The copper electrode was subjected to an anodic cleaning in 85 wt.% H_3PO_4 in H_2O at 0.1 A cm^{-2} for 5 min, rinsed with deionized water and fastened into the cell. A Ag/AgCl electrode (MW-2021; Basi

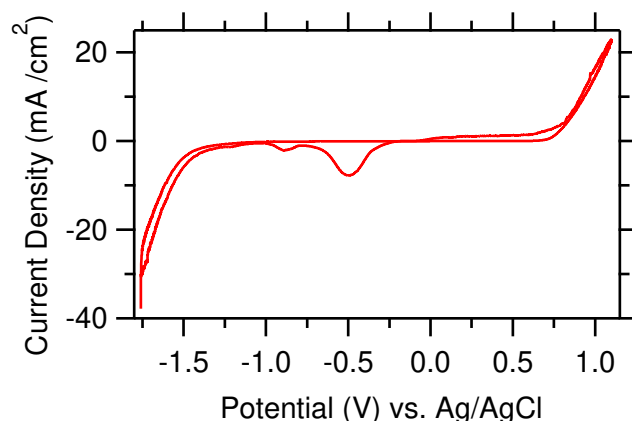


Figure 3.16: Cyclic voltammogram (10 mV s^{-1}) of a copper foil in CO_2 saturated 0.1 M KHCO_3 . The geometric area of the electrode was $\approx 1 \text{ cm}^2$.

Inc.; West Lafayette, IN) was used as the reference electrode and was positioned $\approx 0.3 \text{ cm}$ from the working electrode. A piece of platinum foil (0.025 mm thick; Premion 99.99% metals basis; Alfa Aesar) was used as the counter electrode. A Model 600E potentiostat (CH Instruments, Inc.; Austin, TX) was used to control the potential. Before data collection, the electrolyte was purged with nitrogen gas (20 min). After this initial time, the cell was continuously purged with CO_2 . The copper electrode surface was roughened under CO_2 saturated conditions by subjecting it to fast voltammetry cycles (-1.76 to 1.10 V vs. Ag/AgCl , 1 V s^{-1} , 15 cycles) followed by slow voltammetry cycles (0.01 V s^{-1} , 2 cycles) with the same potential limits (Figure 3.16) [133].

3.5.7 Raman Measurements

Raman spectra were collected with a Horiba Scientific Xplora Raman microscope using a water immersion objective ($\text{NA}=1.0$, $\text{WD}=2.0 \text{ mm}$; LUMPLFLN-60X/W; Olympus Inc.; Waltham, MA). The spectra were obtained in the range of $200\text{-}3500 \text{ cm}^{-1}$ using a grating with 600 lines/mm , a $300 \mu\text{m}$ hole, and a $100 \mu\text{m}$ slit width. A 638 nm laser (0.35 W) served as an excitation source. The acquisition time for a spectrum was 25 s . Calibration for the Raman spectrometer was maintained using a silicon wafer standard (521 cm^{-1}).

A home-built spectro-electrochemical flow cell machined from PEEK was interfaced with the Raman microscope for spectroscopic measurements. Before each experiment, the cell was cleaned according to the protocol described in the prior paragraph. Before spectrum acquisition, the desired potential was applied for 20 s to ensure steady-state conditions. After spectrum acquisition, the cell was briefly (10-20 s) kept at open circuit potential before applying the next potential. All Raman spectra were collected in the direction of decreasing cathodic potential. The uncompensated iR drop in the cell was $\approx 5 \Omega$ and was not corrected for due to the small currents in these experiments ($< 5 \text{ mA cm}^{-2}$ for most potentials). The electrolyte was continuously purged with carbon dioxide throughout the experiment. A diaphragm pump (Cole-Parmer Masterflex L/S Variable-Speed Drive) was employed to maintain constant flow of the electrolyte across the electrode surface.

3.5.8 Lineshape Analysis

Lineshape analysis was carried out by fitting a combination of two Gaussian functions as defined by Stancik et al. [137] and a linear background to the raw spectra.

3.6 Acknowledgements

This work was supported by the National Science Foundation (award no.: 1565948). We thank Prof. Dunwei Wang for granting access to his Raman microscope and for critically reading the manuscript. Prof. Frank Tsung is acknowledged for useful comments on the manuscript. We thank Prof. Kenneth Burch for fruitful discussions and Prof. Yogesh Surendranath for helpful comments on the thin film preparation.

3.7 Original Publication

This chapter has been published: Gunathunge C M,* Li X,* Li J, Hicks R. P., Ovalle, V. J., & Waegele, M. M. Spectroscopic observation of reversible surface reconstruction of copper electrodes under CO₂ reduction. *The Journal of Physical Chemistry C*, **121**, 12337-12344 (2017).

Chapter 4

Hydrogen bonding steers the product selectivity of electrocatalytic CO reduction

4.1 Introduction

In this chapter, using a series of quaternary alkyl ammonium cations (alkyl_4N^+), we systematically manipulated the interfacial properties of the aqueous electrolyte/polycrystalline Cu interface. We chose these cations for two reasons: First, the ionic radius of an alkyl_4N^+ cation increases with increasing alkyl chain length [138]. This characteristic enabled us to tune the width of the electrochemical double layer and therefore the strength of the interfacial electric field for a given applied electrode potential. Second, compared to the more commonly employed alkali cations in CO_2 reduction studies, the use of these cations minimizes the number of possible interactions: Alkali cations are Lewis acids and their Lewis acid hardness decreases by a factor of three when going from Li^+ to Cs^+ [139]. Because of their Lewis acidity, hydrated alkali cations can buffer the interfacial pH [41, 42] and they could potentially chemically interact with intermediates such as surface-adsorbed CO (CO_{ads}) [140], which is a Lewis base. By contrast, alkyl_4N^+ cations are not Lewis acids and their bulky alkyl chains minimize the chance of chemical interactions between these cations and intermediates.

Employing a combined DEMS and SEIRAS approach, we probed the effect of these cations on the reduction of CO_{ads} to ethylene on the polycrystalline Cu electrode. The reduction of CO_{ads} corresponds to the potential-determining step in the electrochemical reduction of CO_2 to hydrocarbons [71, 116, 128, 141, 142]. Understanding the influence of the liquid reaction environment on this process is therefore essential for developing a better mechanistic understanding of CO_2 reduction.

Using DEMS, we found that ethylene is produced in methyl $_4\text{N}^+$ - and ethyl $_4\text{N}^+$ -containing electrolytes, but ethylene is not formed in the presence of propyl $_4\text{N}^+$ and butyl $_4\text{N}^+$. With SEIRAS, we comprehensively analyzed the Cu/electrolyte interface. Irrespective of the identity of the alkyl $_4\text{N}^+$ cation of the electrolyte, we observed approximately the same CO-saturation coverage on the Cu electrode. This observation suggests that the cations do not block CO adsorption sites. Analyzing the dependence of the $\text{C}\equiv\text{O}$ stretch frequency of CO_{ads} on applied electrode potential, we determined the electrochemical Stark tuning slopes and derived the potential-dependent interfacial electric fields in the presence of the four cations. At moderate applied potentials around -1.3 V vs. SHE, the interfacial electric field is on the order of 0.1 V \AA^{-1} . On the basis of a simple electrostatic model, we found that the interfacial electric field does not appreciably affect the adsorption of CO on Cu under the experimental conditions employed.

Analyzing the O–D stretch band of interfacial heavy water (D_2O) at the CO-covered Cu electrode, we found evidence for a layer of waters directly on top of CO_{ads} in methyl $_4\text{N}^+$ - and ethyl $_4\text{N}^+$ -containing electrolytes. These waters have their O–D bonds directed towards the terminal oxygens of the CO_{ads} molecules. Interestingly, this layer of waters is displaced by propyl $_4\text{N}^+$ and butyl $_4\text{N}^+$. These observations suggest that the $\text{CO}_{\text{ads}}\text{-D}_2\text{O}$ interaction is essential for the formation of ethylene during the electrochemical reduction of CO. These waters are predisposed to stabilize the CO dimer, a key intermediate in ethylene formation, by hydrogen-bonding to its terminal oxygens. Theoretical work has

recently predicted that this hydrogen bonding interaction is critical of the formation of this important intermediate [143].

4.2 Results and Discussion

4.2.1 Effects of Alkyl₄N⁺ Cations on CO Reduction

With DEMS, we analyzed the product selectivity during the electrocatalytic reduction of CO to ethylene on polycrystalline Cu electrodes in four different electrolytes. The electrolytes were aqueous solutions of methyl₄N⁺, ethyl₄N⁺, propyl₄N⁺, and butyl₄N⁺ borates (0.1 M) and ethylenediaminetetraacetic acid disodium (EDTA-Na₂; 20 μM). EDTA-Na₂ prevents deactivation of the electrocatalytic interface by chelating trace metal impurities [144]. The electrolytes had a pH of 9.5, which is close to the pK_a of boric acid (9.24). Therefore, the solutions were pH-buffered by the acid-base equilibrium between the anion (borate) and boric acid. Before the start of a DEMS measurement, the electrolyte was first saturated with CO. A 5 sccm flow rate of CO was maintained throughout the experiment.

Figure 4.1 shows the electrochemical current and the partial pressures of the two major products, hydrogen and ethylene, following two potential steps. The products were identified by their characteristic mass fragment/charge ratios (m/z) of 2 for H₂⁺ and 26 for C₂H₂⁺. Unless otherwise noted, all potentials in this work are referenced against the standard hydrogen electrode (SHE). The voltage was first stepped from -0.39 to -1.09 V (light gray shaded area), the potential at which the CO-saturation coverage on the Cu electrode is IR-spectroscopically observed (vide infra). After holding this voltage for one minute, the potential was decreased at a rate of 10 mV s⁻¹ to -1.29 V, which was maintained for five minutes (dark gray shaded area). As shown in Figure 4.1A, comparable electrochemical current densities are observed in the presence of methyl₄N⁺, ethyl₄N⁺, and propyl₄N⁺,

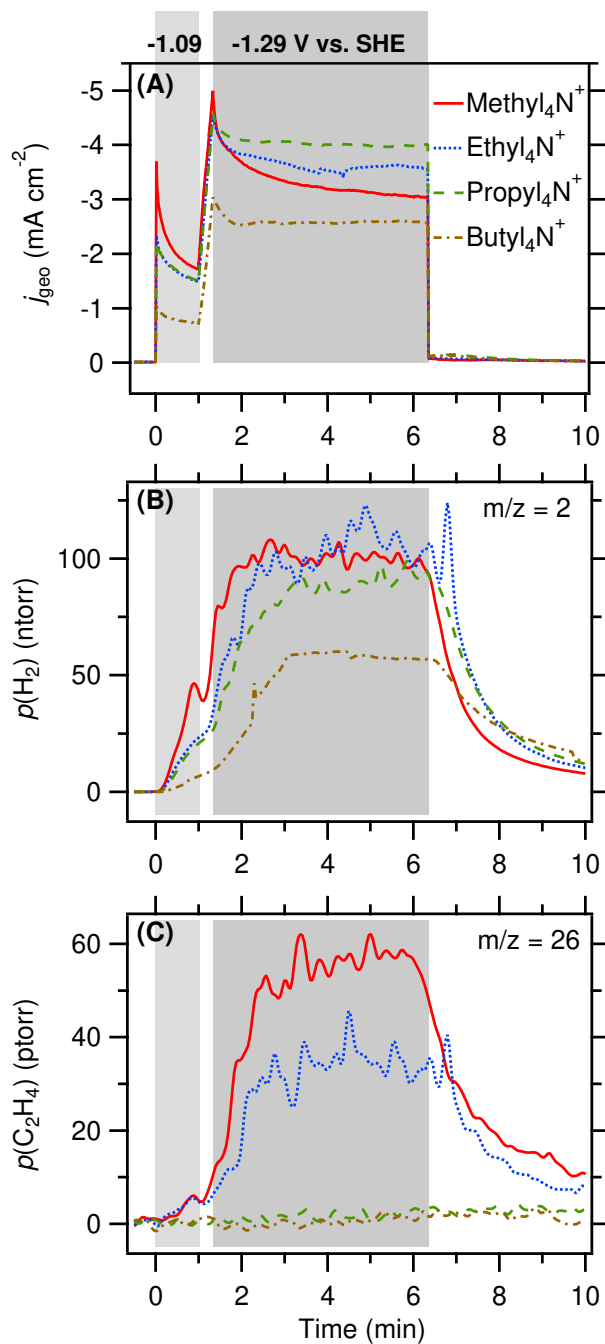


Figure 4.1: DEMS measurements. (A) Electrochemical current density based on the geometric area of the electrode, (B) H₂ partial pressure ($m/z = 2$ for H₂⁺), and (C) C₂H₄ partial pressure ($m/z = 26$ for C₂H₂⁺) recorded during the electroreduction of CO on Cu in the presence of different cations as indicated.

while a $\approx 30\%$ lower current is observed in the presence of butyl₄N⁺. The hydrogen partial pressure (Figure 4.1B) detected by DEMS closely follows these trends, suggesting that hydrogen is the major reduction product. As shown in Figure 4.1C, ethylene is observed in methyl₄N⁺- and ethyl₄N⁺-containing electrolytes, but this product is not observed in the presence of the two larger cations.

Like similar setups [64, 145], our DEMS instrument is not capable of making fully quantitative measurements of the reaction rates: The product collection efficiency is dependent on the tip-electrode distance, which is difficult to accurately reproduce between independent experiments. Due to the low solubility of CO in water (≈ 1 mM), the measured rates may also be limited by mass transport of CO to the electrode. Despite these limitations, we could reproducibly determine that ethylene is formed at detectable rates in the presence of methyl₄N⁺ and ethyl₄N⁺, whereas we did not observe any ethylene in propyl₄N⁺- and butyl₄N⁺-containing electrolytes.

To confirm that the observed signal at $m/z = 26$ is due to ethylene formed by the reaction of CO and water at the Cu electrode, we carried out a series of control experiments: No ethylene signal ($m/z = 26$) is detected in the presence of methyl₄N⁺ in Ar-purged electrolyte (Figure 4.2) or in CO-purged methyl₄N⁺-containing electrolyte when the electrode material is Pt (Figure 4.3). Further, ethylene and hydrogen evolution are virtually unchanged when switching from methyl₄N⁺ to its deuterated form, (CD₃)₄N⁺ (Figure 4.4).

These experiments conclusively demonstrate that the appearance of the $m/z = 26$ signal does not only require the presence of CO, but also necessitates the presence of a Cu electrode. Cu is the only pure metal that can reduce CO to ethylene at appreciable rates [16, 146, 147]. Therefore, the absence of this signal when a Pt electrode is used strongly supports its assignment to the C₂H₂⁺ mass fragment of ethylene. Further, the experiments demonstrate that the signal is not due to the decomposition of the organic

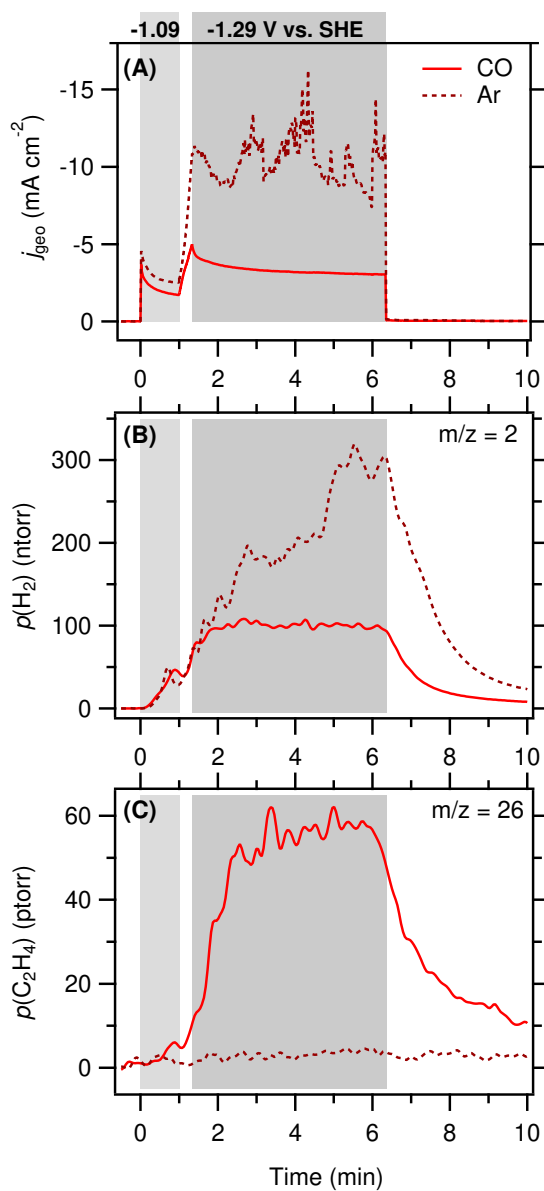


Figure 4.2: The $m/z = 26$ signal is absent in Ar-purged electrolyte. (A) Electrochemical current density during the DEMS measurements. (B) H_2 partial pressure, and (C) C_2H_4 partial pressure in the presence of aqueous solutions of 0.1 M methyl $_4\text{N}^+$ borate under 1 atm of CO (solid line) or Ar (dashed line). At high current densities ($\approx 10 \text{ mA cm}^{-2}$), hydrogen bubbles cover the electrode within a few seconds. Stochastic desorption of the bubbles causes the observed current density fluctuations. A significant fraction of the bubbles does not interact with the sampling tip. Therefore, a fraction of the hydrogen escapes mass spectrometric detection, giving rise to discrepancies between current density and detected hydrogen partial pressure.

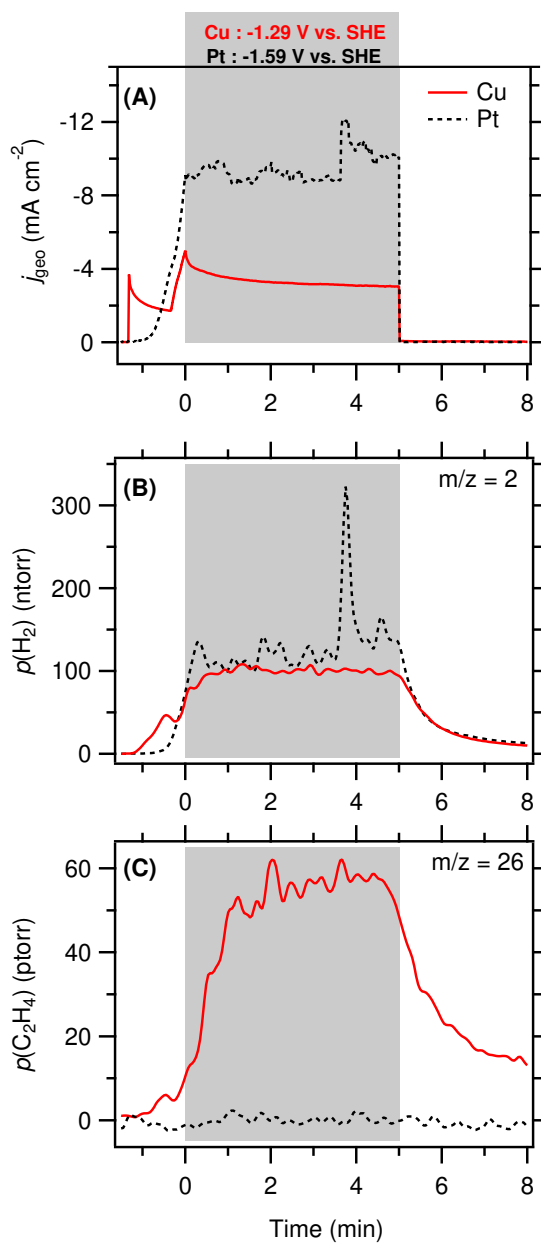


Figure 4.3: The $m/z = 26$ signal is absent when a Pt electrode is used. (A) Electrochemical current density during the DEMS measurements. (B) H₂ partial pressure, and (C) C₂H₄ partial pressure in the presence of aqueous solutions of 0.1 M methyl₄N⁺ borate under 1 atm of CO on Cu (solid line) or Pt (dashed line). Reaction potentials that gave the same amount of detected H₂ were chosen. The lower H₂ detection efficiency in the case of Pt compared to the experiments with Cu is attributed to differences in H₂ bubble nucleation, potentially due to differences in surface morphology. Further, the thin Pt foil has a higher propensity to warp. Therefore, the electrode-sampling tip distance for the experiments with Pt could not be precisely controlled, which impacts the collection efficiency.

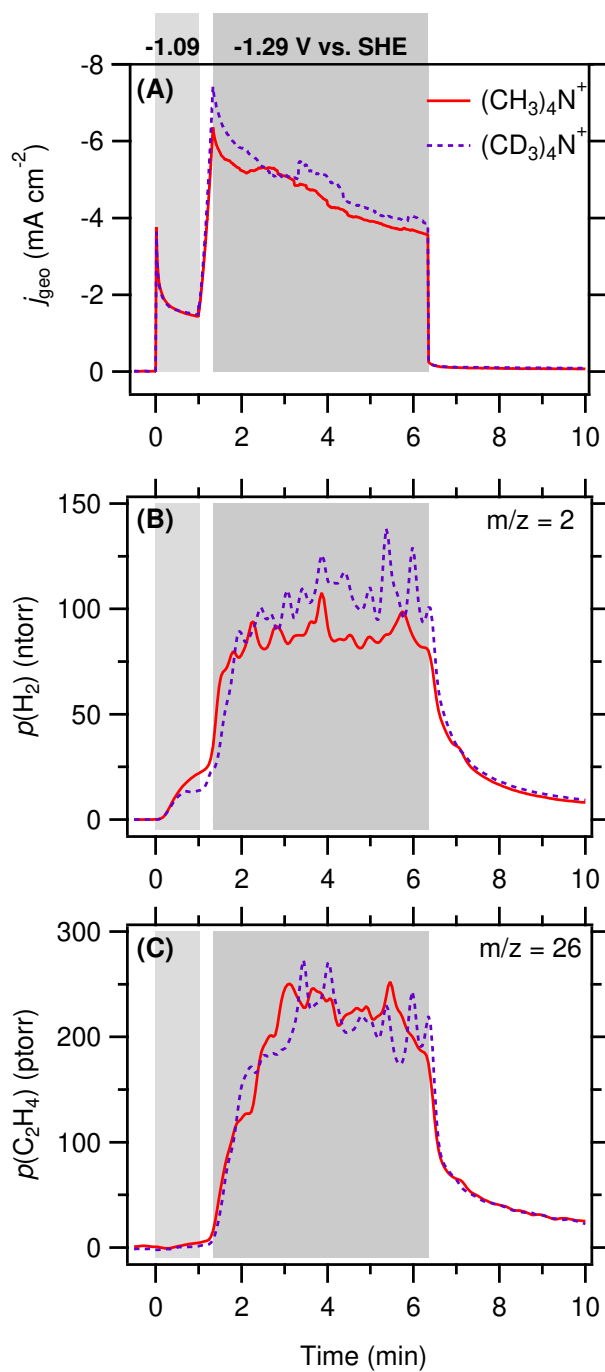


Figure 4.4: The $m/z = 26$ signal is unaffected by the use of deuterated alkyl₄N⁺. (A) Electrochemical current density during the DEMS measurements. (B) H₂ partial pressure, and (C) C₂H₄ partial pressure detected in the presence of aqueous solutions of 0.1 M (CH₃)₄N⁺ (solid line) and (CD₃)₄N⁺ chlorides (dashed line) under 1 atm CO.

cations or their reaction with CO_{ads} .

To confirm further this assignment, we examined the mass spectrum. Because some reactants and products yield ions with m/z values that overlap with the mass spectrum of ethylene (e.g. CO^+ and C_2H_4^+ both have $m/z = 28$), its full mass spectrum cannot be observed during a DEMS measurement. However, ethylene's m/z values of 25, 26, and 27 do not overlap with the mass spectra of any other major reduction product of CO on copper. As shown in Figure 4.5, the observed relative partial pressures at these three m/z values are in good agreement with those expected for ethylene. In addition, we confirmed the identity of ethylene with gas chromatography/mass spectrometry (GC-MS). An experiment with ^{13}C -labeled CO unequivocally established CO as the sole source of ethylene (Figure 4.6).

Alteration of molecular diffusion coefficients by the cations could result in cation-dependent product collection efficiencies. However, the comparable decay times of the hydrogen partial pressure (Figure 4.1B) following the step from -1.39 to -0.39 V at $t \approx 6.3$ min suggest that molecular diffusion coefficients are similar in the four electrolytes. Taken together, the data unambiguously demonstrate that the identity of the alkyl_4N^+ cation of the electrolyte profoundly influences the selectivity of the CO reduction process on the polycrystalline Cu electrode.

4.2.2 SEIRAS of the Cu/Electrolyte Interface

To identify the principal mechanism giving rise to the observed selectivity trend, we characterized the Cu/electrolyte interface under operating conditions, using SEIRAS in an attenuated total reflection (ATR) geometry. An electrolessly deposited polycrystalline Cu film on a Si ATR prism [50, 117, 134] formed the working electrode of a single-compartment spectro-electrochemical cell (Figure 4.8). Characterization of the Cu film by cyclic voltammetry, capacitance measurements and atomic force microscopy imaging are

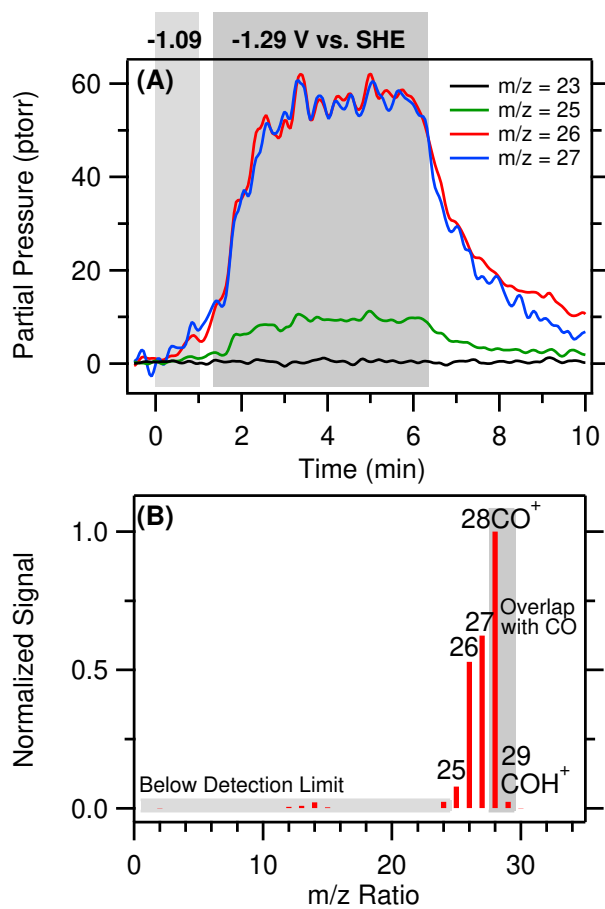


Figure 4.5: The relative partial pressures of the observable m/z values are consistent with the relative signal intensities of the standard mass spectrum of C_2H_4 . (A) $m/z = 23$, 25, 26, 27 signals for the 0.1 M methyl₄N⁺-experiment presented in Figure 1C of the main text. (B) Normalized standard mass spectrum of C_2H_4 from the NIST Chemistry Webbook[148]

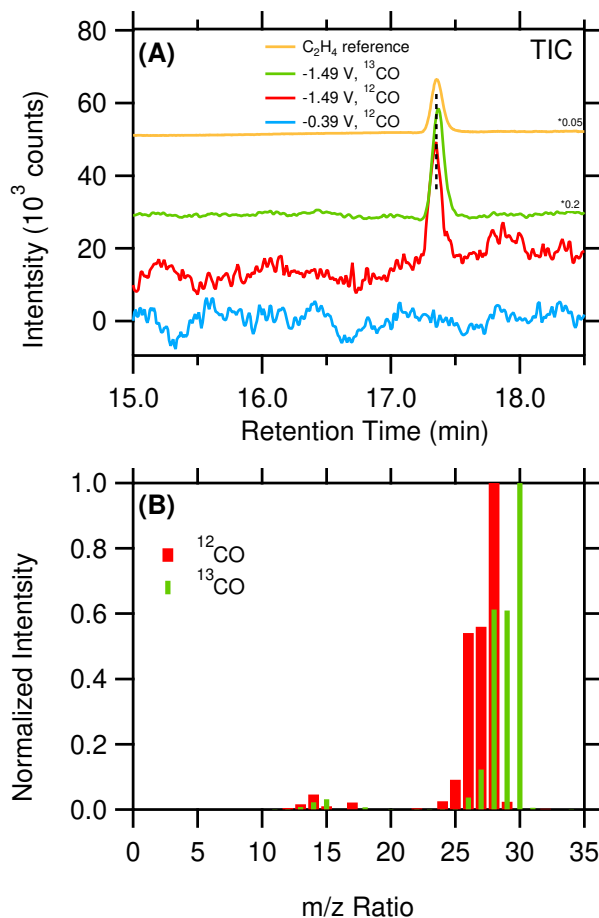


Figure 4.6: GC-MS confirms the formation of ethylene by CO reduction. (A) GC-MS total ion chromatograms (TIC) of a C₂H₄ standard sample and gaseous products of electrolysis in CO-saturated aqueous solutions of 0.1 M methyl₄N⁺ borate as indicated. (B) Mass spectra of the chromatogram peaks at 17.35 min obtained from the gaseous products collected during electrolysis at -1.49 V vs. SHE. GC-MS experiments were carried out in an H-cell. The cathode and anode compartments were separated by a Selemion AMV anion-exchange membrane (AGC Engineering Co.; Chiba, Japan). Each compartment contained 10 mL of electrolyte. Prior to the start of electrolysis, the electrolyte was saturated with CO and the cell was sealed. 100 μ L of gaseous sample from the headspace of the cell was injected into GC-MS after 40 min of electrolysis.

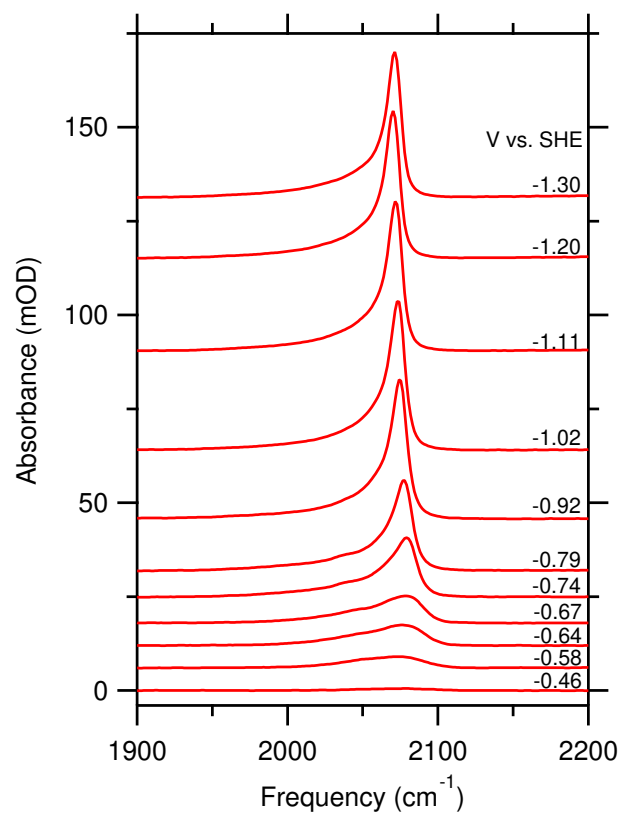


Figure 4.7: Representative C≡O stretch spectra of CO_{ads} as a function of applied potential in the presence of a solution of 0.1 M butyl₄N⁺ chloride in D₂O.

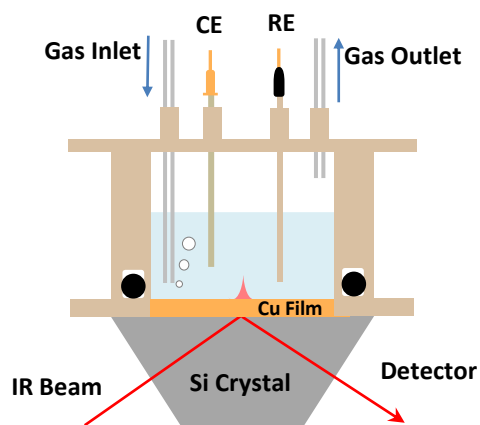


Figure 4.8: Scheme of spectroelectrochemical cell.

shown in figure 4.9 and 4.10.

We carried out the spectroscopic work in solutions of the chloride salts of the alkyl_4N^+ cations in heavy water (D_2O). Primarily, we chose these electrolyte conditions for the following reason: With increasing current density, the Cu thin films have an increasing propensity to delaminate from the Si crystal [117]. A significant component of the faradaic current originates from the hydrogen evolution reaction. To minimize the interference of hydrogen evolution with interfacial spectroscopy, we chose D_2O as the solvent. Due to the kinetic isotope effect, hydrogen evolution on Cu is substantially slower in D_2O compared to H_2O [150]. For DEMS, alkyl_4N^+ borate electrolytes were prepared by titration of the corresponding hydroxide solutions. Because alkyl_4N^+ hydroxides are only available as H_2O solutions, we could not employ this electrolyte preparation procedure for the spectroscopic experiments. Therefore, we chose to directly dissolve alkyl_4N^+ chlorides in D_2O . The pH of these solutions slightly drifts during the measurements. It is well-established that adsorption of CO on Cu is pH-independent [50, 117]. Further, our previous work has established that the CO stretch frequency is only slightly affected by pH [50]. Therefore, the following analyses are not impacted by this choice of electrolyte.

To connect rigorously the DEMS and spectroscopic experiments, we carried out the

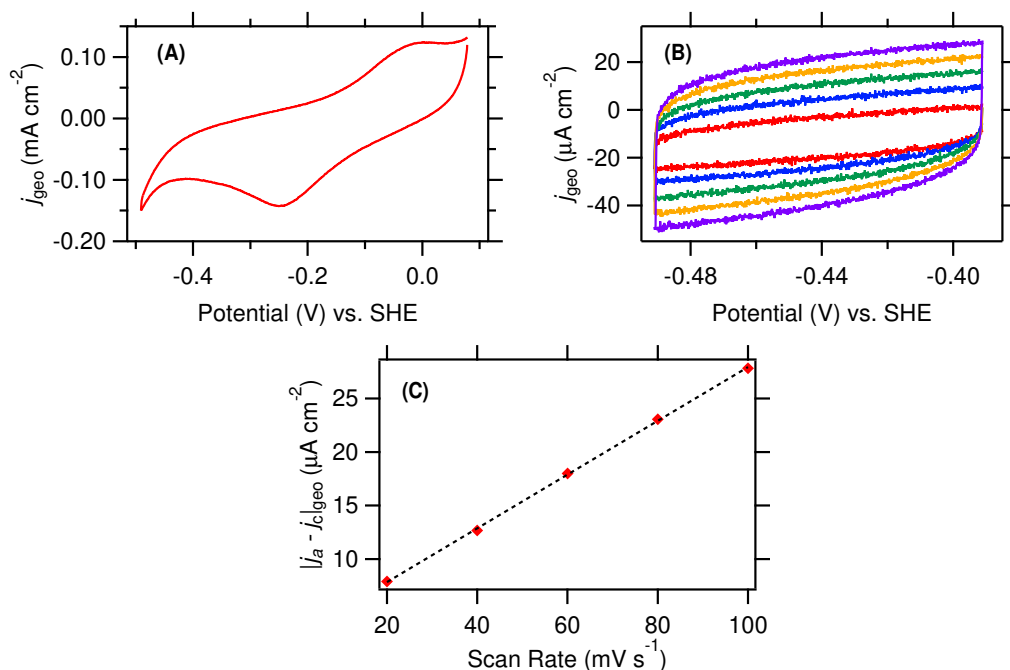


Figure 4.9: (A) Representative cyclic voltammogram obtained following five Cu film cleaning cycles from 0.08 to -0.49 V at a scan rate of 50 mV s^{-1} . (B) Representative CVs taken at scan rates of 20 (red), 40 (blue), 60 (green), 80 (yellow), and 100 mV s^{-1} (purple) to measure the double layer capacitance. (C) The double layer charging current vs. scan rate for the data shown in graph (B) (red squares) and the linear fit (black dotted line) to the data. The roughness of the film was calculated by dividing the slope of the fitted line in graph (C) by a factor of two and a reference double layer capacitance value of $28 \mu\text{F cm}^{-2}$ for a smooth Cu surface[149]

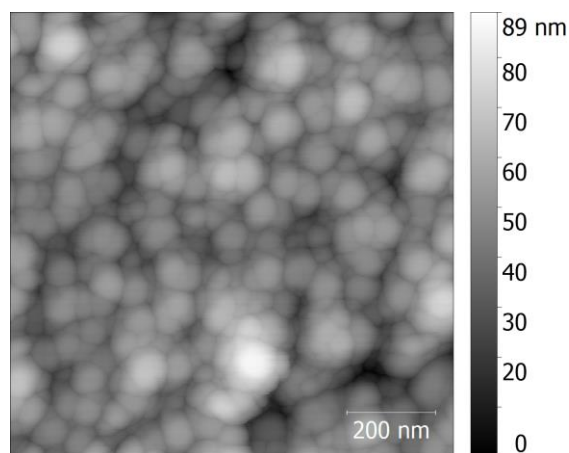


Figure 4.10: AFM image of an as-synthesized Cu film on a Si ATR crystal.

following control experiments: (1) DEMS results qualitatively similar to those presented above are also found in aqueous solutions of alkyl₄N⁺ chlorides (Figure 4.11). We emphasize that we only compare the qualitative trends because the reversible hydrogen electrode (RHE) potential is not well-defined in the latter measurements. (2) Additional spectroscopic experiments were carried out under electrolyte and potential conditions identical to those employed for the DEMS experiments (Figure 4.12). These experiments confirm that the cation-dependent trends in the CO_{ads}-H₂O interaction hold for both electrolytes (vide infra). In the following, we evaluate the effects of the cations on CO surface coverage, interfacial electric field, and interfacial water structure.

4.2.3 Insensitivity of the CO Surface-Coverage on Alkyl₄N⁺ Identity

Figure 4.7 shows representative spectra of the C≡O stretch band of CO_{ads} during a potential sweep from -0.39 to -1.39 V collected in butyl₄N⁺-containing electrolyte. Additional spectra collected in the presence of the other cations and the corresponding current densities are shown in Figures 4.13 and 4.14.

Figure 4.15 shows the dependence of the integrated C≡O stretch band area of CO_{ads} on applied potential in the presence of the different alkyl₄N⁺ cations. The integrated C≡O stretch band area is approximately proportional to the CO coverage on the electrode [72, 125]. Irrespective of the alkyl₄N⁺ cation of the electrolyte, comparable integrated band areas are observed, indicating that the same CO-saturation coverage is reached within the error of the measurement. It was suggested that organic cations, especially those with long hydrocarbon chains, may displace reactants from the electrode surface under certain conditions [34, 37]. Apparently, the Cu/CO interaction is sufficiently strong (compared to the Cu/alkyl₄N⁺ interaction) to prevent such displacement effects. Further, in contrast of recent findings of CO on Pt electrodes [151], no displacement of atop-bound CO (center frequency $\approx 2080\text{ cm}^{-1}$) to the bridge-bonded configuration (center frequency

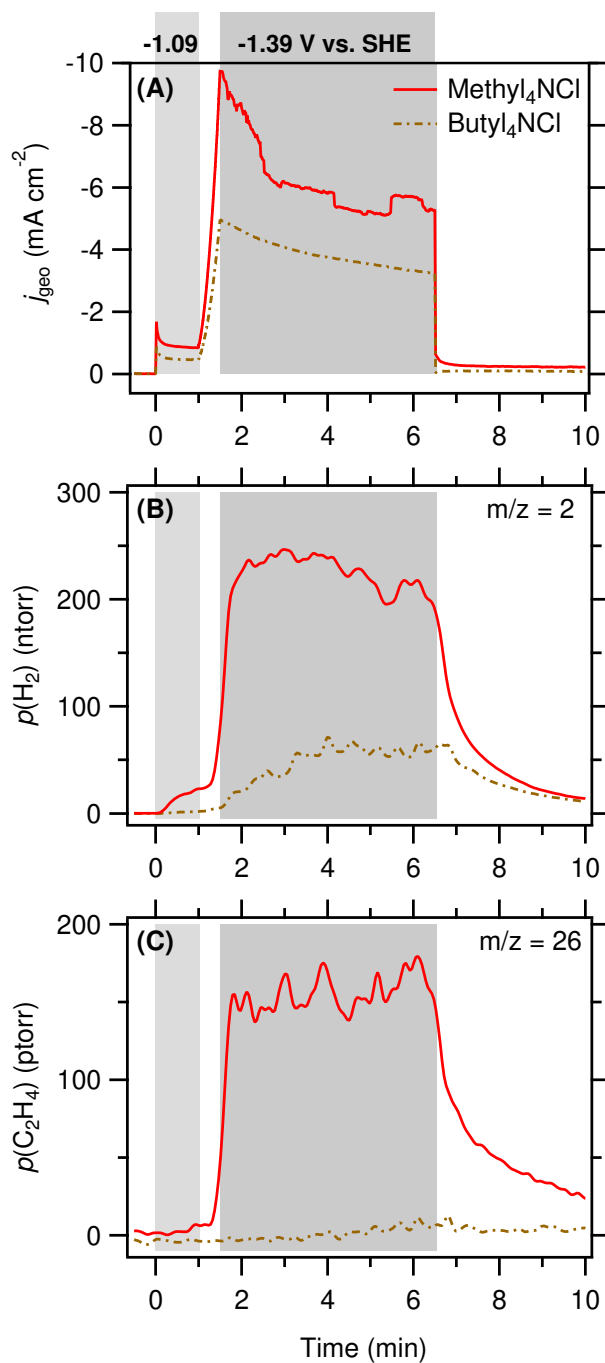


Figure 4.11: The observed trends in the $m/z = 26$ signal are also observed in the presence of the chloride anion. (A) Electrochemical current density during the DEMS measurements. (B) H₂ partial pressure, and (C) C₂H₄ partial pressure detected in the presence of aqueous solutions of 0.1 M methyl₄N⁺ chloride (solid line) and butyl₄N⁺ chloride (dashed line) under 1 atm CO.

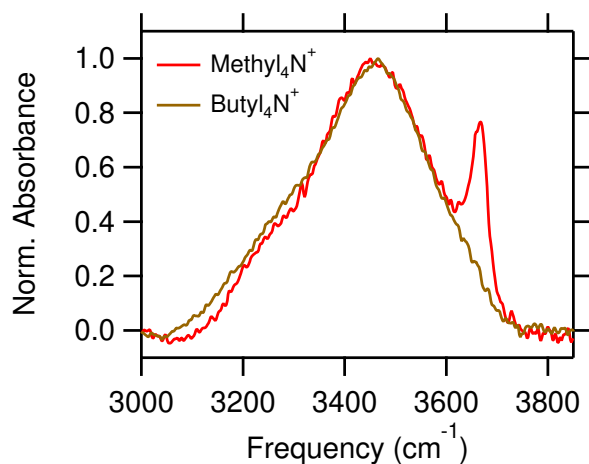


Figure 4.12: The normalized O–H stretch spectra in the presence of aqueous solutions of 0.1 M methyl₄N⁺ and butyl₄N⁺ borate at -1.29 V. The 3675 cm^{-1} band is prominent in methyl₄N⁺-containing electrolyte but absent in the presence of butyl₄N⁺.

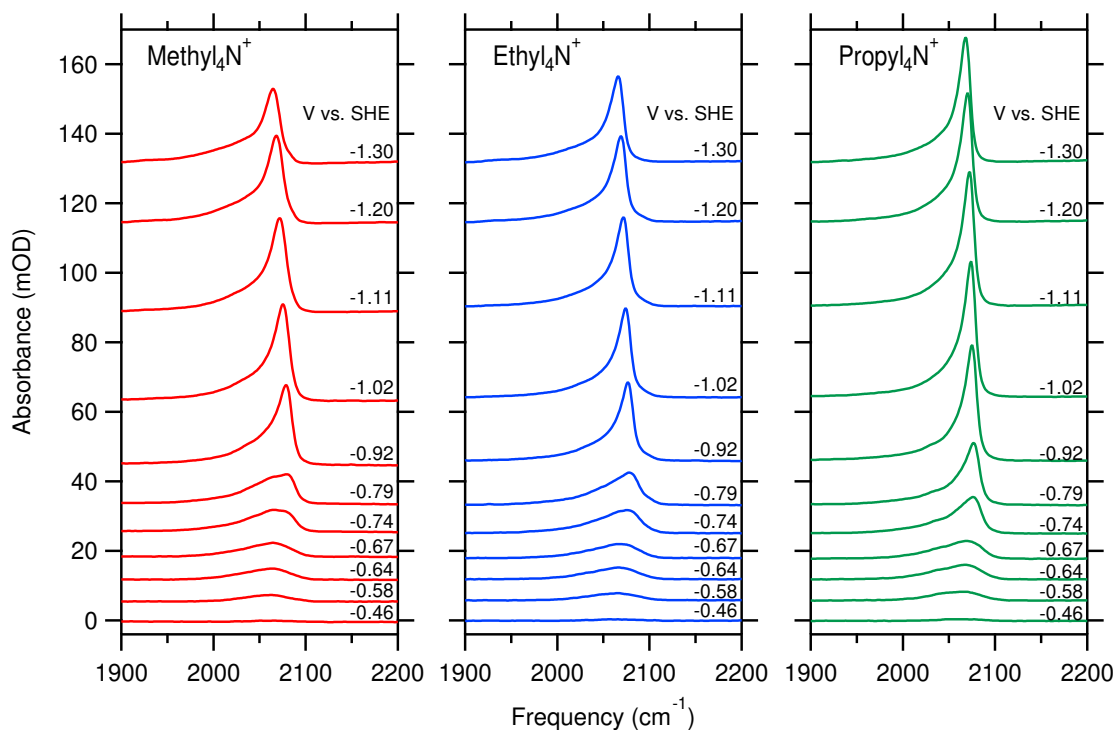


Figure 4.13: Representative C≡O stretch spectra in solutions of 0.1 M methyl₄N⁺, ethyl₄N⁺, and propyl₄N⁺ chloride in D₂O.

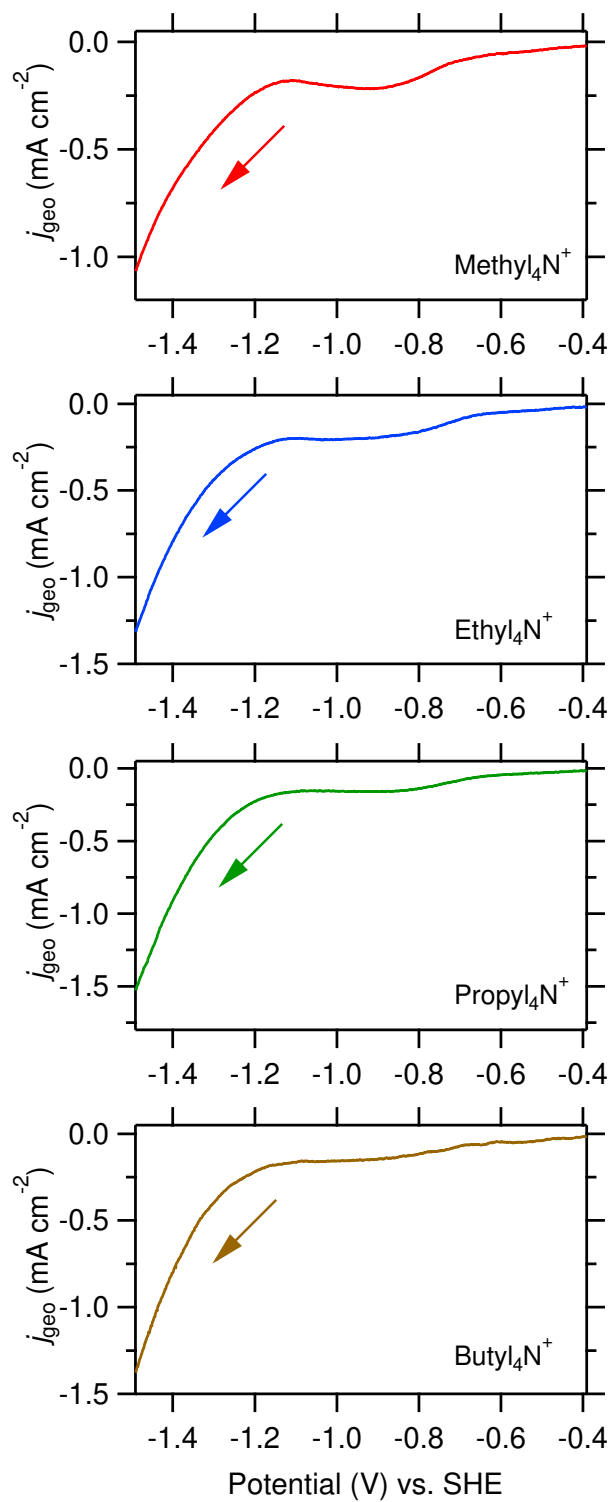


Figure 4.14: Linear sweep voltammetry current-voltage curves for the spectroscopic data presented above. Arrows indicate the sweep direction.

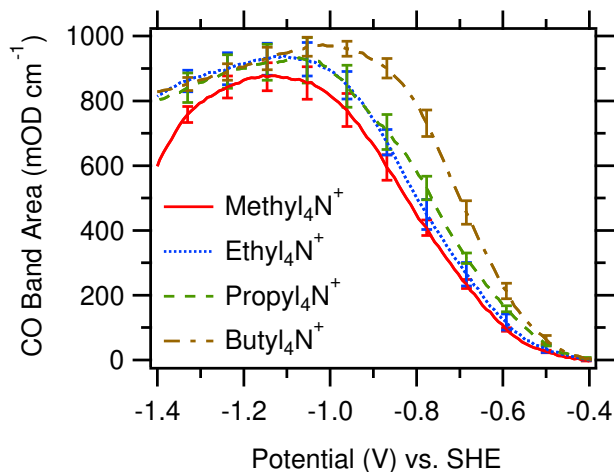


Figure 4.15: Integrated C≡O stretch band areas of CO_{ads} as a function of applied potential in the presence of different cations as indicated. Each trace is an average of three independent experiments. The standard errors are indicated.

$\approx 1800 - 1880 \text{ cm}^{-1}$ [55]) is observed (Figure 4.7 and 4.13). The results demonstrate that the changes in the rate of ethylene evolution with cation identity are not due to blocking of CO adsorption sites.

4.2.4 Cation-Dependent Interfacial Electric Field

Figure 4.16 shows the dependence of the peak frequency of the C≡O stretch band of CO_{ads} on applied potential. To minimize coverage-dependent frequency shifts [152], the analysis was restricted to a potential range in which the CO coverage is approximately constant. The dependence of the frequency (ω) on the applied potential (ϕ) arises from the vibrational Stark effect, i.e. the influence of the interfacial electric field ($\mathcal{E}(\phi)$) on the C≡O stretch mode [153–156]:

$$\omega(\phi) = \omega_{\text{PZC}} - \Delta\mu \mathcal{E}(\phi), \quad (4.1)$$

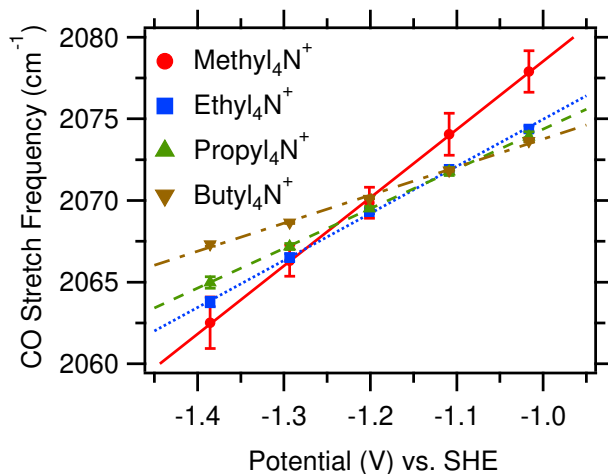


Figure 4.16: Peak frequencies of the C≡O stretch band of CO_{ads} as function of applied potential in the presence of different cations as indicated. The lines are linear fits to the data. The standard errors are indicated.

where ω_{PZC} is the C≡O stretch frequency in the absence of the interfacial electric field and $\Delta\mu$ represents the vibrational Stark tuning rate. By writing $\Delta\mu$ and \mathcal{E} in eq. 4.1 as scalar quantities, we implicitly assumed that the corresponding vectors are either parallel or antiparallel to each other. This assumption is reasonable for CO adsorbed on a metal surface [157]. However, it is an approximation as our electrodes are not atomically flat. We take $\Delta\mu$ and \mathcal{E} as a positive quantities when the corresponding vectors point from the electrolyte towards the metal surface. The $\Delta\mu$ vector of CO_{ads} points from O to C.

The vibrational Stark tuning rate for CO adsorbed on Cu is $1.3 \times 10^{-6} \text{ cm}^{-1}/(\text{V cm}^{-1})$ [158]. Although this value was derived from quantum mechanical calculations of CO on a Cu surface in vacuum, very similar values were estimated for CO adsorbed on various metal electrodes in an aqueous environment [157]. Further, experimental measurements of $\Delta\mu$ for CO adsorbed on various metals in vacuum also yielded comparable values [157].

The data in Figure 4.16 contain information on the structure of the electrochemical double layer. Inspection of this figure shows that the frequency linearly depends on the

applied potential. This observation implies that the interfacial electric field is also linearly related to the applied potential (eq. 4.1). One model of the electrochemical double layer that is consistent with this finding is the Helmholtz model [159]:

$$\mathcal{E}(\phi) = -\frac{\Delta\phi_{\text{M-EI}}}{d_{\text{H}}}, \quad (4.2)$$

where $\Delta\phi_{\text{M-EI}}$ is the interfacial potential drop, $\phi_{\text{M}} - \phi_{\text{EI}}$ (ϕ_{M} and ϕ_{EI} are the potentials of the metal and the bulk electrolyte, respectively). d_{H} is the width of the Helmholtz layer, i.e. the distance between the negatively charged electrode surface and the plane of the cationic counter charge (outer Helmholtz plane). Combining eqs. 4.1 and 4.2, we obtain

$$\omega(\phi) = \omega_{\text{PZC}} + \left(\frac{\Delta\mu}{d_{\text{H}}}\right) \Delta\phi_{\text{M-EI}}. \quad (4.3)$$

The width of the Helmholtz layer (d_{H}) is expected to increase with increasing cation size: With increasing cation size, the outer Helmholtz plane shifts further away from the electrode surface. Consistent with this expectation, the slopes of the lines in Figure 4.16, the electrochemical Stark tuning rates ($\Delta\mu/d_{\text{H}}$) [140, 160, 161], decrease with increasing cation size (Table 4.1). One may expect the extracted values of d_{H} to track the ionic radii of the cations. The radii of the cations (derived from the partial molar volumes of the cations in water [138]) are 3.2, 3.8, 4.4, and 4.7 Å for methyl₄N⁺, ethyl₄N⁺, propyl₄N⁺, and butyl₄N⁺, respectively. The extracted width increases at a larger rate with increasing cation size (Table 4.1) than that expected based on the radii of the cations. This observation suggests that the smaller cations fit between CO_{ads} molecules on the surface. This interpretation is reasonable because the CO-saturation coverage on Cu electrodes is estimated to be significantly less than one monolayer [162]. By contrast, the larger cations appear to reside at a distance from the electrode approximately equal to the distance between the surface of the electrode and the terminal oxygen of CO_{ads} (3.05 Å [163]) plus the radius

of the cation. Clearly, based on eq. 4.2, we therefore expect the interfacial electric field to decrease with increasing cation size for the same applied potential.

To extract the interfacial electric field from eq. 4.1, knowledge of the C≡O stretch frequency of CO_{ads} in the absence of the field (ω_{PZC}) is required. The interfacial electric field strength vanishes at the potential of zero charge (PZC) of the electrode. This potential can be estimated from Figure 4.16 [161]. Inspection of this figure shows that the lines obtained for ethyl₄N⁺, propyl₄N⁺, and butyl₄N⁺-containing electrolytes cross at ≈ -1.1 V. This crossing point indicates that CO_{ads} experiences the same interfacial electric field at this potential, irrespective of the electrolyte's cation. This condition can only be fulfilled when the electrode does not carry any net charge, i.e. when $\Delta\phi_{\text{M-EI}} = 0$ V (eq. 4.3). Therefore, this crossing point is the approximate PZC of the CO-covered Cu electrode in alkyl₄N⁺ chloride solutions. This PZC is more negative than the values obtained on Cu electrodes in contact with acidic and weakly adsorbing electrolytes (≈ -0.73 V; pH = 5.7; 0.01 M NaClO₄) [164]. The more negative value obtained here is consistent with the expectation that the PZC shifts negatively by ≈ 60 mV per one unit increase in pH [165]. Additionally, the specific adsorption of Cl⁻ on Cu may contribute to the more negative value.

The frequency/potential relationship obtained in the presence of methyl₄N⁺ does not cross with the other lines at ≈ -1.1 V (Figure 4.16). Although the measurement of the electrochemical Stark tuning slope in the presence of this cation was highly reproducible, the value of the y-axis intercept varied by as much as ≈ 5 cm⁻¹ over independent experiments. Although the Cu thin films were stable for all the presented measurements, we noticed a higher propensity of film delamination in the presence of methyl₄N⁺. Therefore, this cation may interact more strongly with the electrode than the other ones in this series. Because even a significant error of 0.2 V in the value of the PZC will not change our conclusions drawn from the analysis that follows, we will assume a PZC of ≈ -1.1 V of the Cu electrode for all of the four cations.

Table 4.1: Electrochemical Stark tuning rates ($\Delta\mu/d_H$) extracted from fitting a linear model to the data in Figure 4.16 and derived Helmholtz double layer widths (d_H). The standard deviations are indicated.

Cation	$\Delta\mu/d_H$ ($\text{V}^{-1} \text{cm}^{-1}$)	d_H (\AA)
methyl ₄ N ⁺	41.8 ± 0.6	3.1 ± 0.0
ethyl ₄ N ⁺	28.8 ± 0.4	4.5 ± 0.1
propyl ₄ N ⁺	24.3 ± 0.2	5.4 ± 0.0
butyl ₄ N ⁺	17.2 ± 0.6	7.6 ± 0.3

Using the extracted PZC and $\Delta\mu$, we evaluated the interfacial electric field (\mathcal{E}) according to eq. 4.1. We emphasize that the relationship between $\omega(\phi)$ and $\mathcal{E}(\phi)$ as defined in eq. 4.1 does not require the assumption of a particular model of the electrochemical double layer. Figure 4.17 shows the interfacial electric field experienced by CO_{ads} in the presence of different cations. The interfacial field decreases by a factor of ≈ 2.5 when going from methyl₄N⁺ to butyl₄N⁺-containing electrolyte. The obtained interfacial fields are on the order of 0.1 V \AA^{-1} . The electrostatic contribution to the CO-adsorption energy as a function of the local field is [166, 167]

$$E(\mathcal{E}) \approx -\mu\mathcal{E} - \frac{\alpha}{2}\mathcal{E}^2, \quad (4.4)$$

where μ , and α are the dipole moment and polarizability of CO_{ads} , respectively. CO is only weakly adsorbed on Cu and therefore is expected to exhibit little change in its dipole moment and polarizability with respect to the values of CO in the gas phase. With the gas-phase values of 0.0244 e\AA and $0.124 \text{ e\AA}^2 \text{ V}^{-1}$ for the dipole moment and polarizability of CO [168], respectively, and an applied potential of -1.3 V , eq. 4.4 predicts a minute change in the CO adsorption energy of $< 5 \text{ meV}$, which is negligible with respect to the adsorption energy of CO on Cu ($\approx -0.6 \text{ eV}$ [123, 169]).

The results suggest that the interfacial field at the Cu/electrolyte interface under the experimental conditions employed in this work are too small to have a significant effect

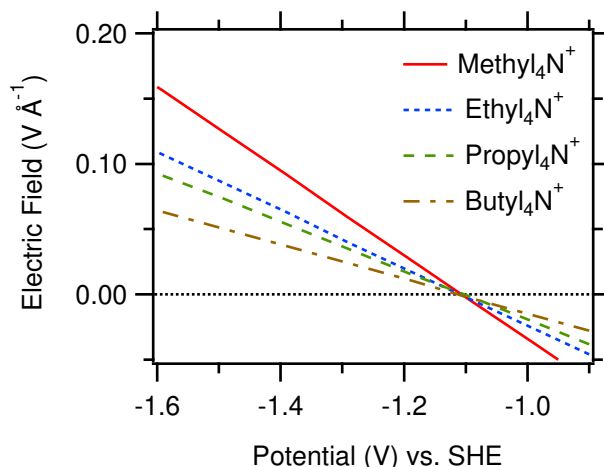


Figure 4.17: Dependence of the interfacial electric fields on applied potential in the presence of different electrolyte cations as indicated.

on the CO adsorption energy. This conclusion is consistent with DFT calculations demonstrating that an electric field of 0.1 V \AA^{-1} has negligible effect on the adsorption energy of CO on Cu [55].

The interfacial electric field will affect the rate of electron-transfer from the electrode to surface intermediates [33, 159]. However, ethylene is also not observed in the presence of butyl₄N⁺ when a potential of -1.39 V is applied (Figure 4.11). This observation demonstrates that, in the present case, the cation-specific selectivity for ethylene is likely unrelated to the strength of the interfacial electric field.

4.2.5 Dependence of the CO_{ads}-H₂O Interaction on Cation Identity

Interfacial water is the source of hydrogen in the electroreduction of CO_{ads} and provides the solvation environment for the reactants. Therefore, the structure and dynamics of interfacial water is expected to affect this process. To determine if the cations alter the structure of water near the electrode surface, we analyzed the dependence of the O–D stretch band of interfacial water at the CO-covered Cu electrode on the presence of the different cations (Figure 4.18). In the presence of methyl₄N⁺ and ethyl₄N⁺, a sharp and

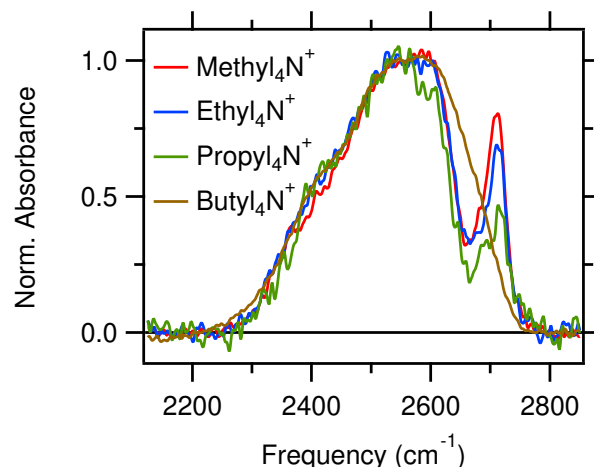


Figure 4.18: Normalized O–D stretch spectra recorded at a potential of -1.02 V in the presence of different cations as indicated. The unnormalized spectra are provided in the SI Appendix (Figure S14).

prominent band is observed at ≈ 2710 cm^{-1} on top of the broad O–D stretch band. The band is very weak in the presence of propyl $_4\text{N}^+$ and it is entirely absent in butyl $_4\text{N}^+$ -containing electrolyte. To confirm that these trends are also observable under electrolyte conditions identical to those employed in the DEMS study, we collected spectra in H_2O solutions of methyl $_4\text{N}^+$ and butyl $_4\text{N}^+$ borates. As shown in Figure 4.12, the spectrum collected in the presence of methyl $_4\text{N}^+$ borate exhibits a sharp band at 3675 cm^{-1} . The position of the band is in good agreement with the isotopic shift that is expected on the basis of a simple harmonic oscillator model of the O–D/H stretch mode. By contrast, the band is absent in solutions of butyl $_4\text{N}^+$ borate. These observations establish that the trends are also observable under the electrolyte conditions employed in the DEMS study.

Prior reports established that this band arises from interfacial waters that directly interact with CO_{ads} [44, 134, 170–174]. These waters, which are not directly adsorbed on the electrode surface, have their O–D bonds pointed towards the terminal oxygen of CO_{ads} [44, 172]. The integrated area of this band tracks the CO surface coverage (Figure 4.19). Further, the band is absent in Ar-purged methyl $_4\text{N}^+$ -containing electrolyte (Fig-

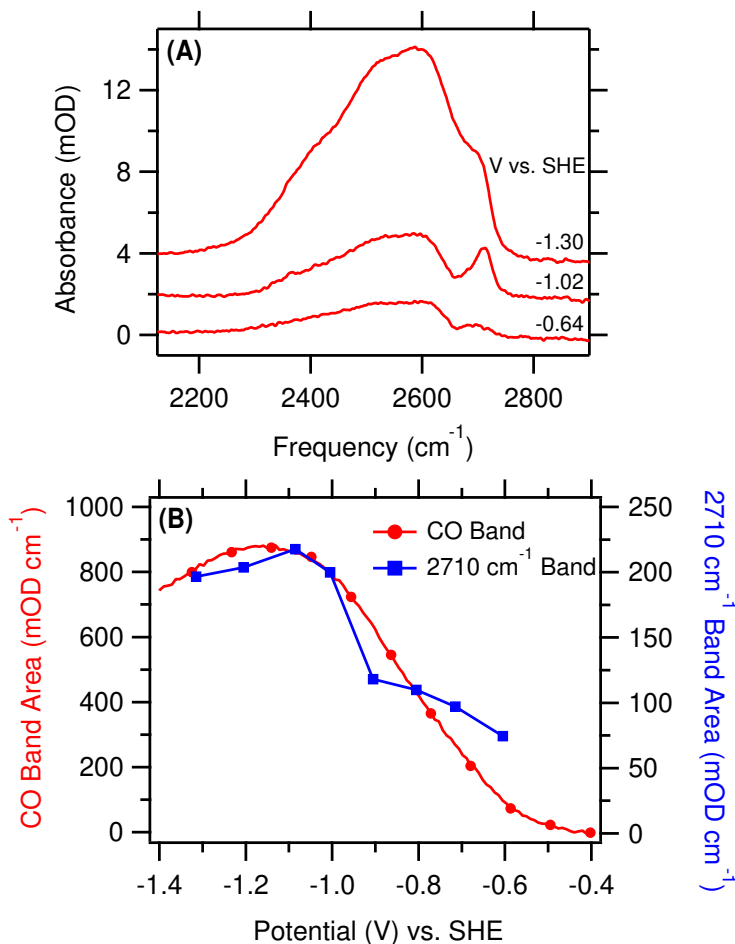


Figure 4.19: (A) Representative O–D stretch spectra in 0.1 M methyl₄N⁺ chloride in D₂O. (B) Integrated band areas of the C≡O stretch band (red circles) and O–D stretch band at 2710 cm⁻¹ (blue squares) as a function of applied potential.

ure 4.20). These findings confirm that the band originates from interfacial waters that interact with CO_{ads}.

The center frequency of this band is slightly red-shifted by a few tens of wavenumbers with respect to the frequency of the O–D stretch of an isolated water molecule [171, 173]. On the basis of this observation, the interaction of water with CO_{ads} is often considered to be weak [44, 172] compared to the hydrogen bonding in bulk water. However, it was shown that this interaction affects the electronic structure of the metal–CO bond [173], and it was suggested that the CO_{ads}–H₂O interaction may be stronger than previously

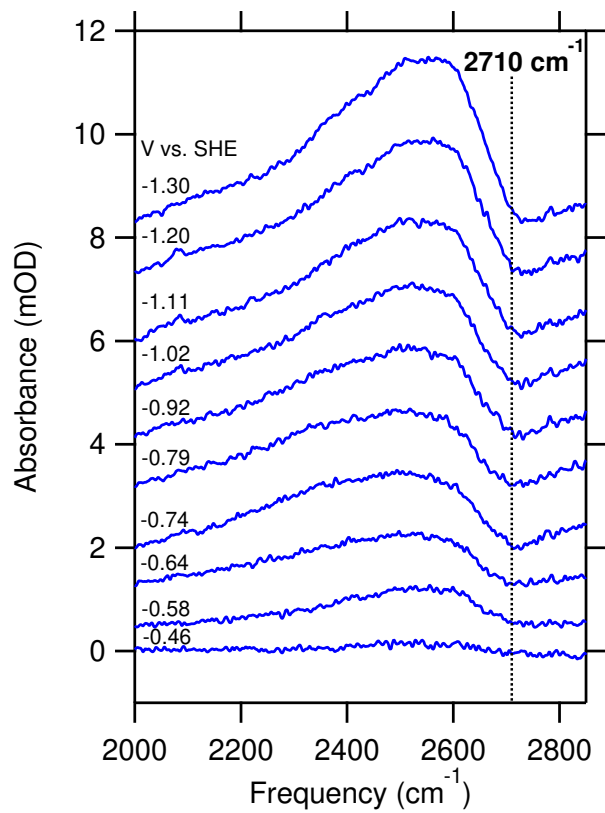


Figure 4.20: O–D stretch spectra in Ar-purged 0.1 M methyl₄N⁺ chloride electrolyte confirm that the 2710 cm⁻¹ band is only present for the CO-covered Cu electrode.

assumed [174]. Irrespective of this debate, our observations suggest that the two larger cations disrupt the $\text{CO}_{\text{ads}}-\text{H}_2\text{O}$ interaction. Due to their larger size and more hydrophobic nature compared to $\text{methyl}_4\text{N}^+$ and ethyl_4N^+ , they are expected to be more effective in displacing water molecules from the interface [43, 44].

Our findings suggest that ethylene evolution is shut down in the presence of $\text{propyl}_4\text{N}^+$ and butyl_4N^+ due to the disruption of the $\text{CO}_{\text{ads}}-\text{H}_2\text{O}$ interaction by these two cations. At moderate overpotentials and basic pH, computational models [128, 141–143, 175] and experimental evidence [145, 176] have suggested a surface-adsorbed CO dimer as an important intermediate in this reaction. Recent computational work predicts that hydrogen-bonding of interfacial waters to the oxygens of the CO dimer is required for its formation to be energetically favorable [143]. On the basis of these findings, we propose CO dimerization is impeded in the presence of $\text{propyl}_4\text{N}^+$ and butyl_4N^+ because these cations displace the water layer on top of CO_{ads} . Due to this displacement, these waters are not available to stabilize the CO dimer by hydrogen bonding to its terminal oxygens (Figure 4.21). This picture is also consistent with the cation-dependent structure of the double layer (Table 4.1). Our study provides the first experimental indication that this hydrogen bonding interaction is indeed critical for CO dimerization on Cu electrodes.

4.3 Conclusions

We investigated the effects of alkyl_4N^+ on the electroreduction of CO to ethylene on the polycrystalline Cu electrode in aqueous electrolytes. Using DEMS, we showed that ethylene is produced in the presence of $\text{methyl}_4\text{N}^+$ and ethyl_4N^+ , but this product is not observed in $\text{propyl}_4\text{N}^+$ - and butyl_4N^+ -containing electrolytes. Using SEIRAS, we comprehensively characterized the properties of the electrocatalytic interface in the presence of the four alkyl_4N^+ cations. Our spectroscopic results suggest that the change in ethylene se-

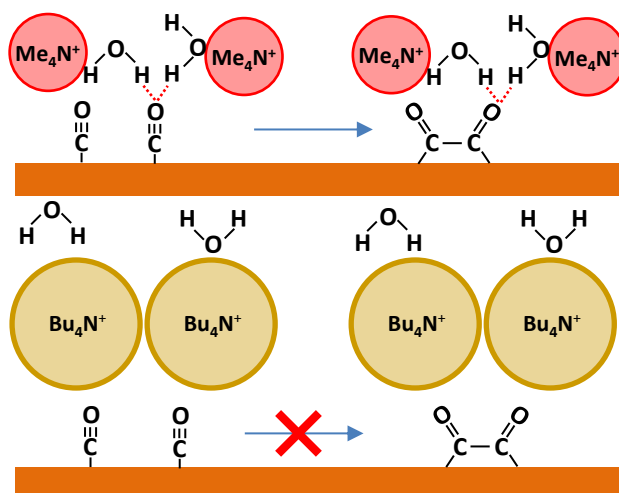


Figure 4.21: Possible CO_{ads} coupling mechanism on Cu(100), as proposed by Bagger et al. [143]. (A) In the presence of methyl $_4\text{N}^+$ (or ethyl $_4\text{N}^+$), interfacial waters are available to stabilize the CO dimer by hydrogen bonding. (B) In the presence of butyl $_4\text{N}^+$ (or propyl $_4\text{N}^+$), the formation of the CO dimer is blocked due to the displacement of interfacial water by these hydrophobic cations.

lectivity does not arise from blocking of CO adsorption sites or cation-dependent changes in the interfacial electric field strength. Analysis of the O–D stretch band of interfacial heavy water (D_2O) at the CO-covered electrode revealed a sharp band at $\approx 2710 \text{ cm}^{-1}$ in methyl $_4\text{N}^+$ - and ethyl $_4\text{N}^+$ -containing electrolytes. This band, which is due to water with its O–D bond directed towards the terminal oxygen of CO_{ads} , is weak in the presence of propyl $_4\text{N}^+$ and entirely absent in butyl $_4\text{N}^+$ -containing electrolyte. This observation demonstrates that these two cations displace the layer of waters on top of CO_{ads} . The waters identified by their characteristic O–D stretch frequency at $\approx 2710 \text{ cm}^{-1}$ are predisposed to hydrogen bond to the terminal oxygens of the CO dimer, a key intermediate in the formation of ethylene [128, 141–143, 145, 175, 176]. In line with recent theoretical predictions [143], our experimental results suggest that hydrogen bonding of water to the CO dimer is critical for its formation.

4.4 Experimental Procedures

4.4.1 Materials

For Cu thin film deposition on Si, NH_4F (40 wt.% in H_2O) and HF (48 wt.%) were purchased from Fisher Scientific (Waltham, MA). $\text{CuSO}_4 \cdot 5\text{H}_2\text{O}$ (99.999%; trace metal basis), EDTA-Na_2 (99.0 - 101.0%; ACS Reagent), 2,2-bipyridine ($\geq 99\%$; ReagentPlus), HCHO (35 wt.%; 10% methanol as stabilizer), and NaOH (99.99%; trace metals basis) were acquired from Sigma Aldrich (St. Louis, MO). Polycrystalline diamond pastes were procured from Ted Pella (Redding, CA) or Electron Microscopy Sciences (Hartfield, PA).

For electrolyte preparation, tetramethylammonium chloride ($\geq 98\%$; Acros Organics), tetraethylammonium chloride (98%; Alfa Aesar), tetramethylammonium hydroxide pentahydrate (98%; Acros Organics), tetraethylammonium hydroxide (35 w/w% aq soln; Alfa Aesar), tetrapropylammonium hydroxide (25% in water; Acros Organics), tetrabutylammonium hydroxide (40 wt.%; Acros Organics), boric acid (Puratronic 99.9995%; Alfa Aesar), and deuterium oxide (99.8 atom% D; Acros Organics) were purchased from Fisher Scientific. Tetrapropylammonium chloride (98%), tetrabutylammonium chloride ($\geq 97\%$) were obtained from Sigma Aldrich. Deuterated tetramethylammonium chloride (D12, $\geq 98\%$) was obtained from Cambridge Isotope Laboratories (Tewksbury, MA).

Ar (ultra high purity), N_2 (ultra high purity), and CO (99.999%) were obtained from Air Gas (Radnor, PA).

4.4.2 DEMS System

The details for the DEMS setup could be found in section 2.2. The reaction products that evolved from the electrode/electrolyte interface were collected by the sampling tip positioned ≈ 0.5 mm above the electrode surface.

4.4.3 Cu Foil Preparation

Before each DEMS measurement, the copper foil (Puratronic 99.999%, 1.0 mm; Alfa Aesar) was first polished with a 1500-grit sand paper to remove surface oxides. The surface was then hand-polished with 1.0 and 0.3 μm alumina slurries. After each 10-min polishing step, the electrode was thoroughly rinsed with high purity water. After 10 min of sonication in high purity water, the copper foil was electropolished in a H_3PO_4 , H_2O , and H_2SO_4 bath with volume ratio 10:5:2. The copper foil was subjected to a potential of 2.3 V vs. Cu for two sequential periods of 2 s, separated by an interval of 30 s at open circuit potential [177]. Finally, the copper foil was rinsed thoroughly with high purity water and blow-dried with N_2 . Before each DEMS experiment, the copper foil was subjected to cleaning voltammetric cycles. A surface roughness factor of ≈ 3 compared to a smooth Cu surface [149] was determined on the basis of electrochemical capacitance measurements. The electrochemical protocols are detailed in our prior report [55].

4.4.4 Electrochemical Methods for DEMS

Aqueous electrolytes containing 0.1 M alkyl_4N^+ hydroxide and 20 μM EDTA- Na_2 were titrated with H_3BO_3 to a pH of 9.5. The pH after the experiments was 9.5 ± 0.1 . Measurements were performed in a single-compartment electrochemical cell with an electrolyte volume of 3 mL. A VersaStat3 potentiostat (AMETEK; Berwyn, PA) controlled the potential. A Pt foil (Premion 99.99%, 0.025 mm; Alfa Aesar) and a leak-free Ag/AgCl electrode (ET072, 3.4 M KCl; eDAQ; Colorado Springs, CO) were employed as the counter and reference electrodes, respectively. Before each experiment, the Pt foil was soaked in an aqueous acid solution (30 wt.% H_2SO_4 , 30 wt.% HNO_3) for one hour, and was then rinsed with high purity water. The Ag/AgCl reference electrode was regularly calibrated with respect to a saturated calomel electrode (CHI 150; CH Instruments Inc.; Austin, TX). The mea-

sured potential was converted to the SHE scale according to $V_{\text{SHE}} = V_{\text{Ag/AgCl}} + 0.209 \text{ V}$. 76% of the solution resistance was compensated *in situ* with the VersaStat3 potentiostat. The geometric surface area of the electrode was $\approx 1.9 \text{ cm}^2$.

The sequence of potential steps during DEMS measurements is described in the main text. Prior to the potential jump ($t = 0 \text{ s}$ in Figure 4.1), the electrolyte was purged with Ar at a rate of 5 sccm for 10 min. A voltammetric cycle from -0.39 to -0.99 V with 10 mV s^{-1} was carried out, then the potential was held at -0.39 V for 20 min under CO purging at a rate of 5 sccm. Mass spectra were recorded with a time resolution of $\approx 3 \text{ s}$. For each partial pressure trace, the value that was recorded about 30 s before time zero (the time of the first potential step, Figure 4.1) was subtracted from the trace to zero out the baseline. Each trace in Figure 4.1 was smoothed by a binomial algorithm and is the average of two independent measurements. The background-subtracted, unsmoothed raw data are shown in Figures 4.22,4.23,4.24,4.25.

4.4.5 Cu Thin Film Preparation for SEIRAS

Thin polycrystalline Cu films were deposited on a reflecting facet of a 60° Si prism (Pike Technologies; Madison WI) by an electroless deposition procedure and characterized as described in our previous report [55]. The film roughness factor was ≈ 13 . The roughness of the films was maintained between $\pm 20\%$ of the original value after the spectroelectrochemical measurements.

4.4.6 Electrochemical Methods for SEIRAS

For the spectroelectrochemical measurements shown in the main text, the electrolyte was prepared with D_2O . The initial pH of the electrolyte was 9.7 ± 0.5 . After the experiments, the pH typically decreased by $\approx 10\%$. Measurements were performed in a single-

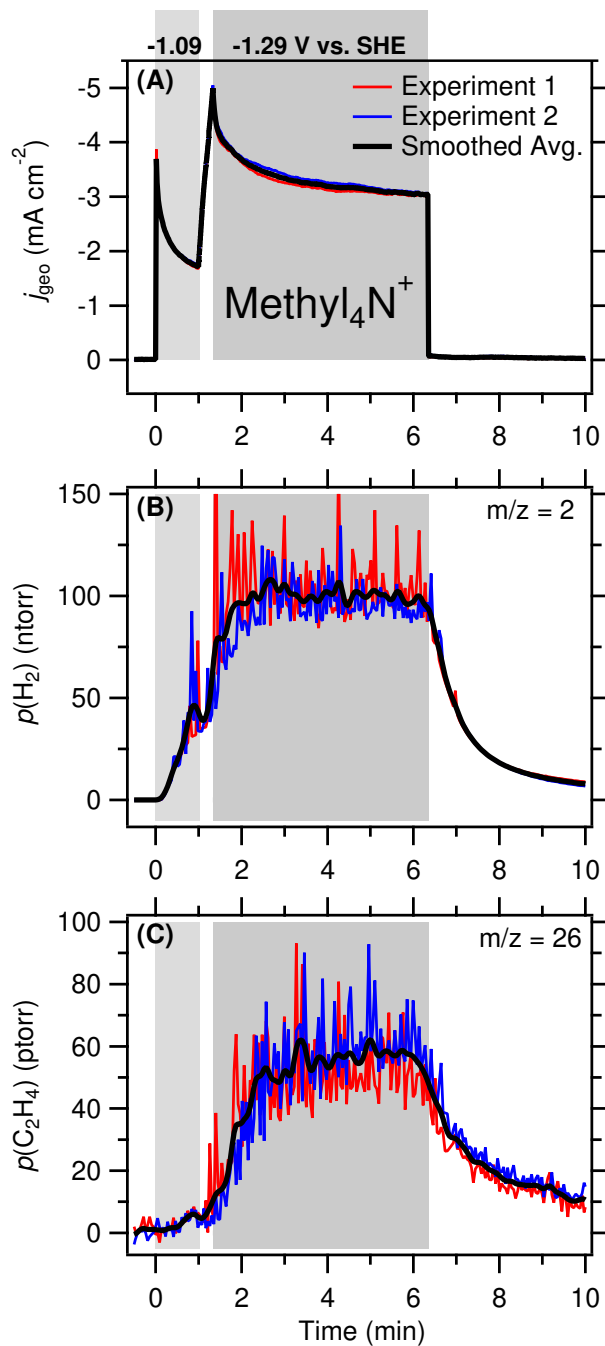


Figure 4.22: Raw DEMS data for methyl₄N⁺. (A) Electrochemical current density, (B) H₂ partial pressure, and (C) C₂H₄ partial pressure recorded during two independent experiments (thin red and blue traces) of CO electroreduction on Cu. The thick black trace represents the smoothed average of the two experiments.

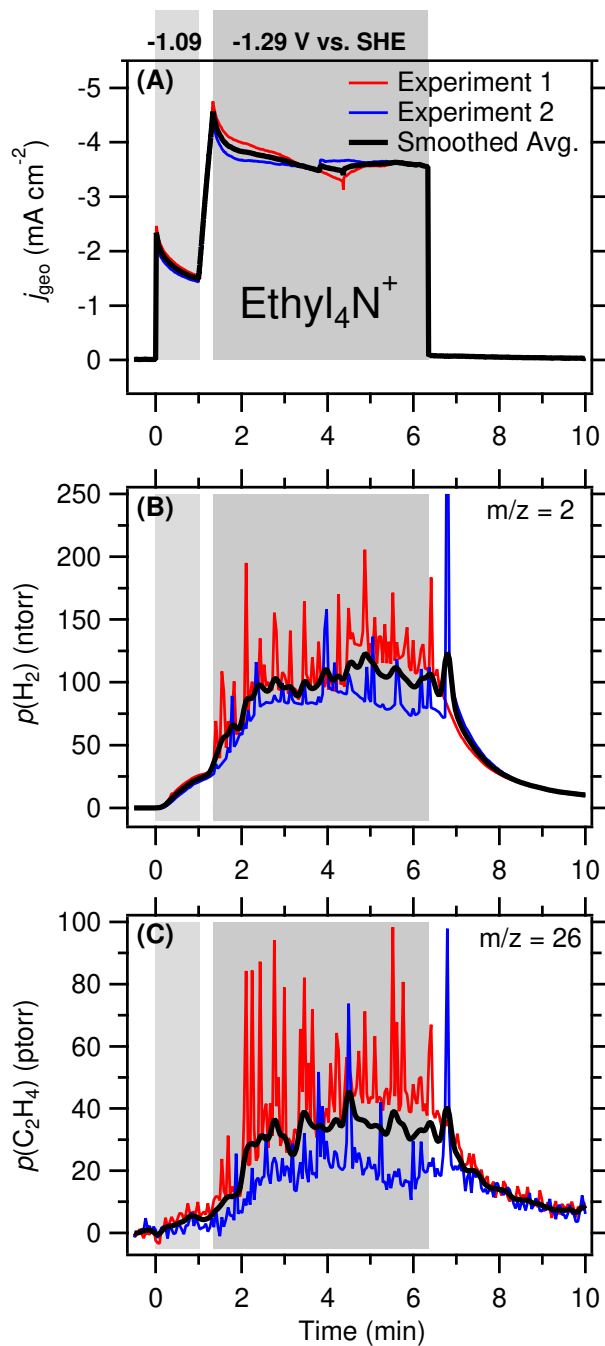


Figure 4.23: Raw DEMS data for ethyl₄N⁺. (A) Electrochemical current density, (B) H₂ partial pressure, and (C) C₂H₄ partial pressure recorded during two independent experiments (thin red and blue traces) of CO electroreduction on Cu. The thick black trace represents the smoothed average of the two experiments.

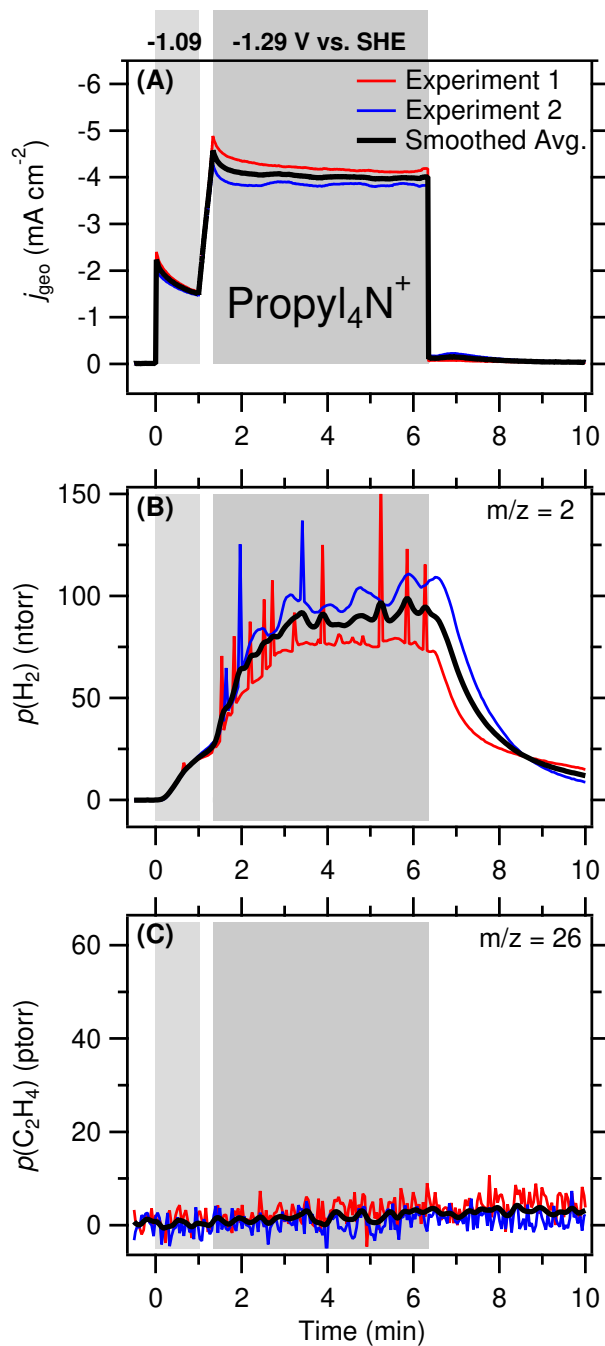


Figure 4.24: Raw DEMS data for propyl₄N⁺. (A) Electrochemical current density, (B) H₂ partial pressure, and (C) C₂H₄ partial pressure recorded during two independent experiments (thin red and blue traces) of CO electroreduction on Cu. The thick black trace represents the smoothed average of the two experiments.

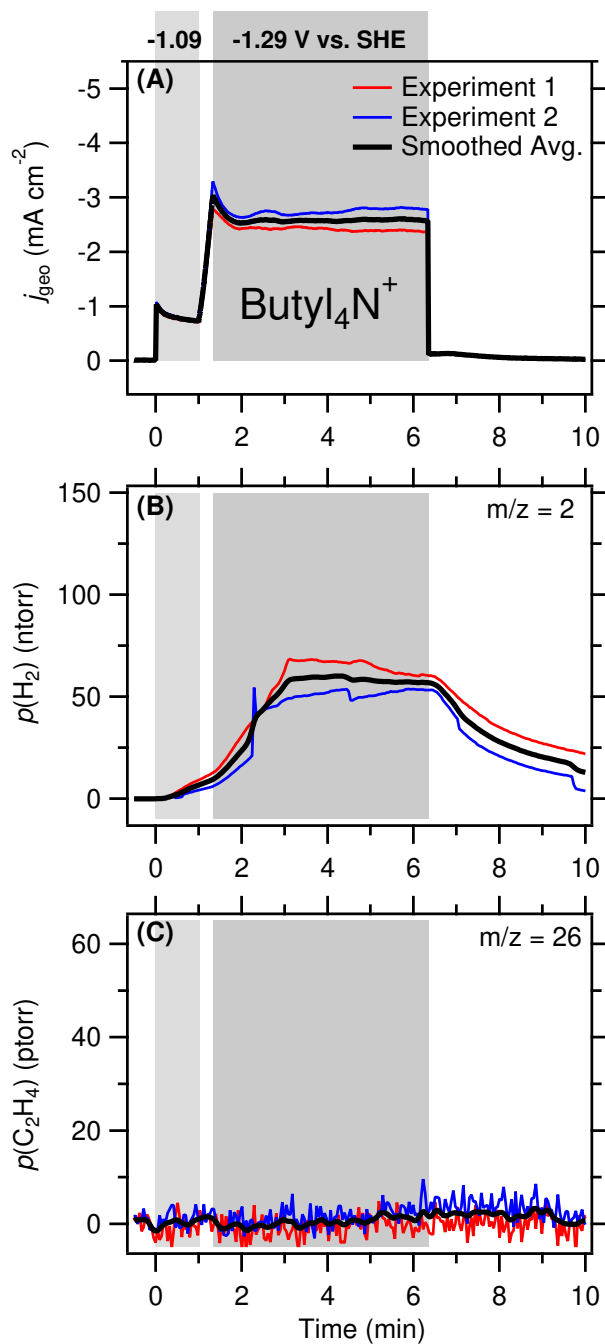


Figure 4.25: Raw DEMS data for butyl₄N⁺. (A) Electrochemical current density, (B) H₂ partial pressure, and (C) C₂H₄ partial pressure recorded during two independent experiments (thin red and blue traces) of CO electroreduction on Cu. The thick black trace represents the smoothed average of the two experiments.

compartment electrochemical cell with 4 mL electrolyte. The electrical connection from the film to the potentiostat was made by sandwiching a ring of Cu foil (Puratronic 99.999%, 0.025 mm; Alfa Aesar) between the circular edge of the film and a Viton O-ring from the PEEK electrochemical cell. A Au wire (99.999%, 0.5 mm; Alfa Aesar) and a Ag/AgCl electrode (RE-5B, 3 M NaCl; BASi Inc; West Lafayette, IN) were employed as the counter and reference electrodes, respectively. The Cu ring and Au wire were polished with 0.3 μm alumina slurry for 5 min and were then rinsed with high purity water. The Ag/AgCl reference electrode was calibrated as described above. The geometric surface area of the Cu thin film was $\approx 1.9 \text{ cm}^2$. The Cu thin film was first held at -0.39 V for 20 min for CO saturation, and the potential was then linearly swept to -1.49 V at a rate of 2 mV s^{-1} . The cell resistance was not compensated.

4.4.7 SEIRAS Measurements

The Si crystal coated with the Cu thin film was assembled into a PEEK electrochemical cell, which was placed on an ATR accessory (VeeMax III; Pike Technologies; Madison, WI). Spectra were recorded with a nitrogen-purged Bruker Vertex 70 FTIR spectrometer (Billerica, MA) equipped with a liquid nitrogen-cooled photoconductive MCT detector (FTIR-16; Infrared Associates; Stuart, FL). Spectra were collected every 4.61 s with a spectral resolution of 4 cm^{-1} and a scanner velocity of 40 kHz. The change in optical density was calculated according to $\text{mOD} = -10^3 \cdot \log(S/R)$, with S and R referring to the single beam sample spectrum and single beam reference spectrum, respectively. The reference potential was -0.39 V . To determine accurately the peak frequency, a cubic spline was employed to interpolate between recorded data points (Figure 4.26).

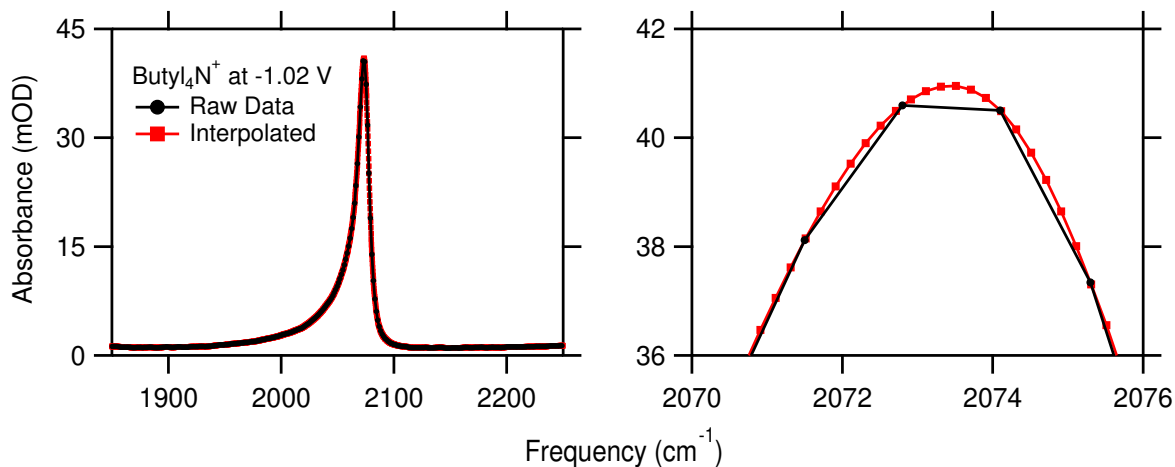


Figure 4.26: An example of FTIR data interpolation. The data presented was collected in the presence of 0.1 M butyl₄N⁺ in D₂O at potential of -1.02 V. The interpolated data (red) captures the CO peak frequency more accurately than the raw data (black).

4.5 Acknowledgements

This work was supported by the National Science Foundation (Award No.: CHE-1565948). We thank Prof. Udayan Mohanty for helpful discussions about the electrostatics of the electrochemical interface and Prof. Dunwei Wang for critically reading the manuscript.

4.6 Original Publication

This chapter has been published: Li J,* Li X,* Li J, Gunathunge C M, & Waegele, M. M. Hydrogen bonding steers the product selectivity of electrocatalytic CO reduction. *Proceedings of the National Academy of Sciences*, **116**, 9220-9229 (2019).

Chapter 5

Impact of Alkali Metal Cations and Iron Impurities on the Evolution of Hydrogen on Cu Electrodes in Alkaline Electrolytes

5.1 Introduction

In this chapter, we studied the HER on a polycrystalline Cu rotating disk electrode (RDE) in Na^+ and Cs^+ -containing electrolytes under alkaline conditions. We found that trace amounts of iron impurities in hydroxide salts of the highest commercially available purity grades substantially increase the rate of the HER at a pH of 13. Specifically, in 0.1 M CsOH, the HER current density increased by a factor of five over the course of eleven cyclic voltammograms (CV) due to the deposition of iron on the Cu RDE. Without iron impurities, the HER currents in 0.1 M NaOH and CsOH electrolytes are virtually the same, indicating the absence of a measurable cation effect on the HER. With density functional theory (DFT), it is proved that the hydrogen binding energy to Cu(100) is only slightly perturbed in the presence of co-adsorbed alkali metal cations. Further, the cations would need to induce large changes of about $\geq 0.3 \text{ V \AA}^{-1}$ in the local electric field to impact the activation barrier of the Volmer step of the HER. Because Cs^+ is known to promote CO_2/CO reduction on Cu electrodes [22, 50, 145, 162], our observations suggest that Cs^+

can be utilized to selectively enhance this desired reaction over the HER. Optimal catalytic performance in alkali metal hydroxides can only be achieved by efficient removal of iron impurities prior to electrolysis.

5.2 Results and Discussion

5.2.1 Effect of Trace Iron and Nickel Impurities on the HER on Cu Electrodes

We first measured the rates of the HER on a polycrystalline Cu RDE in 0.1 M aqueous solutions of NaOH and CsOH during eleven consecutive CVs with turning potentials of 0.15 and ≈ -0.65 V versus RHE. All potentials were corrected for the iR -drop and were referenced against RHE, unless otherwise noted. The real cathodic turning potentials slightly varied for consecutive CVs because 15% of the iR -drop was corrected post run. The scan rate of the electrode potential was 10 mV s^{-1} and the rotation rate of the RDE was 2500 rpm. For this set of measurements, the electrolytes were prepared by dissolving the as-received hydroxide salts in high-purity water. The purities of NaOH and CsOH were 99.99% and 99.95%, respectively.

Figure 5.1 shows representative CVs of Cu in the two electrolytes. For clarity, the most anodic potential in the graphs is -0.2 V, but the anodic turning potentials of the CVs was $+0.15$ V. The current density increases with increasing cycle number in both electrolytes. However, whereas the current density approximately doubles in 0.1 M NaOH over the course of the eleven CVs, it increases by about a factor of five in 0.1 M CsOH. The steady-state current densities, which were taken right after completion of the eleven CVs, closely coincide with the final CVs. These data indicate that the electrode undergoes more substantial, irreversible changes in 0.1 M CsOH than in 0.1 M NaOH.

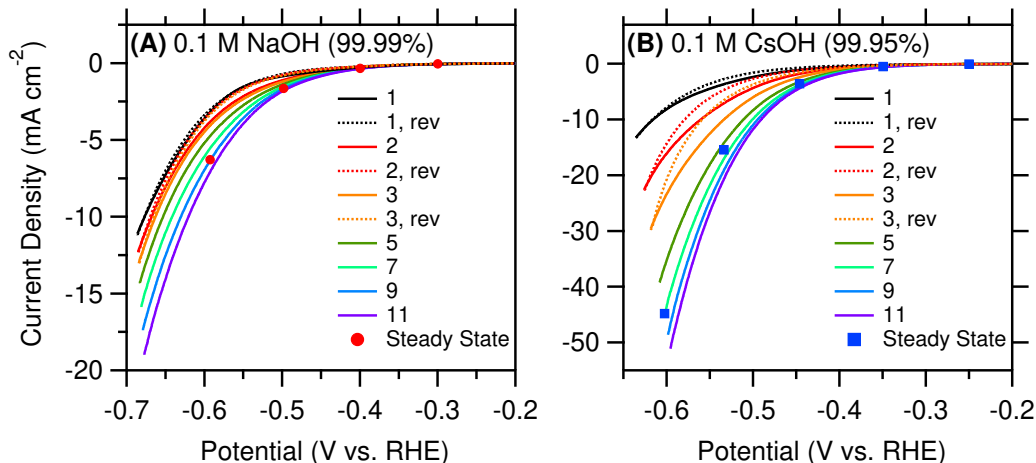


Figure 5.1: Consecutive CVs of a polycrystalline Cu RDE in 0.1 M solutions of as-received (A) NaOH (99.99%) and (B) CsOH (99.95%). The CVs were taken at a scan rate of 10 mV s^{-1} and a rotation rate of 2500 rpm of the RDE. The purity of each salt is indicated in the parenthesis in each panel. The numbers in the panels refer to the cycle number and “rev” denotes the respective reverse (anodic) scan. For clarity, the reverse scans of the other cycles are not shown. Steady state measurements were collected right after the eleventh CV.

The increase in the HER rate could arise from a number of different reasons, including cationic corrosion [178], oxidation/reduction-induced surface reconstruction [179], adsorbate-induced reconstruction [180], or deposition of trace elements from the electrolyte on the electrode [181].

Cationic corrosion is expected to require significantly more cathodic potentials (-1.0 V versus RHE) and higher electrolyte concentrations ($\geq 1 \text{ M}$) compared to those employed here [178]. Electrolyte-induced surface reconstructions can also occur during oxidation/reduction cycles [179]. However, during our CVs, the electrodes are never exposed to oxidizing conditions. Moreover, cationic corrosion and electrolyte-induced restructuring typically result in substantially roughened surfaces. However, in the present case, the electric double layer capacitance increased by only $\approx 10\%$ over the course of the CVs, suggesting that the roughness of the electrode did not significantly change. On the basis of prior work, we expect that residual surface oxides and hydroxides will be almost com-

Table 5.1: Nanomolar (nM) concentrations of iron and nickel in 0.1 M solutions of the as-received alkali metal hydroxides.

Electrolyte	Fe (nM)	Ni (nM)
0.1 M NaOH (99.99%)	40	180
0.1 M CsOH (99.95%)	240	/

pletely removed after the first CV [55]. For these reasons, we exclude these two processes as the underlying reason for the increase in HER activity.

While reconstructions on the nano- and micro-scales apparently do not occur to any significant extent under our reaction conditions, changes of the predominant surface adsorbates with potential may affect the surface at the atomic level. Surface-reconstructions due to the adsorption of hydrogen have been reported for Cu(100) electrodes at pH values < 3 , but no such changes in the surface were found at higher pH values [180]. At pH 13, the (100) facet is remarkably stable and the major surface facet on polycrystalline Cu [51]. Therefore, it is unlikely that atomic-level reconstructions are the origin of the changes in catalytic activity.

Lastly, the change in catalytic activity could arise from the deposition of trace metal impurities, as was reported for other electrocatalytic processes [181, 182]. Although the used hydroxides are of the highest purity grades that are commercially available, they contain trace amounts of nickel and iron. Table 5.1 shows that both alkali metal hydroxides contain a significant amount of iron and/or nickel. No detectable amount of nickel was found in CsOH. The values in Table 5.1 are based on the analyses provided by the manufacturers of the salts. We obtained virtually the same values from the analyses of the electrolytes by ICP-AES. The full elemental analyses from the manufacturers are provided in Table 5.2. Other major impurities are alkali and earth alkaline ions, which cannot be reduced on the Cu electrode under our experimental conditions. Iron species are the only trace metal impurities that occur at detectable levels in both electrolytes and are expected to be readily reduced at the most cathodic potentials accessed in this study. Nickel and iron

Table 5.2: Full Elemental Analyses of NaOH and CsOH from the Manufacturers.

	NaOH (99.99%; MilliporeSigma)	CsOH (99.95%; Acros Organics)
	(ppm)	(ppm)
Boron (B)	1.0	/
Calcium (Ca)	0.9	0.6
Copper (Cu)	0.1	/
Iron (Fe)	0.6	0.8
Manganese (Mn)	2.1	/
Nickel (Ni)	2.7	/
Cesium (Cs)	1.6	/
Potassium (K)	26.7	12
Lithium (Li)	0.8	≤ 0.2
Rubidium (Rb)	0.4	4
Sodium (Na)	/	22
Magnesium (Mg)	/	0.1
Barium (Ba)	/	8
Strontium (Sr)	/	2
Aluminium (Al)	/	0.3
Chromium (Cr)	/	0.3

are substantially better electrocatalysts for the HER than Cu: Their polarization curves are shifted by ≈ 250 mV more anodically relative to the HER polarization curve for Cu [183]. Therefore, deposition of either of the species on the Cu electrode is expected to enhance the rate of the HER.

To test if iron and nickel deposit on the Cu RDE during electrolysis, we examined the electrode with XPS following 1.9 h of electrolysis at a potential of -0.68 V for 0.1 M NaOH and -0.60 V for 0.1 M CsOH. The RDE was removed from the electrolyte under applied bias to minimize dissolution of the deposit into the electrolyte. The electrochemical currents as a function of time are provided in Figure 5.2.

As shown in Figure 5.3, following electrolysis in 0.1 M CsOH (99.95%), the RDE exhibits the characteristic peaks of iron. Iron deposits after electrolysis in 0.1 M NaOH (99.99%) were below the detection limit of the XPS instrument. Interestingly, even though this electrolyte contains a significant amount of nickel (Table 5.1), nickel deposits were

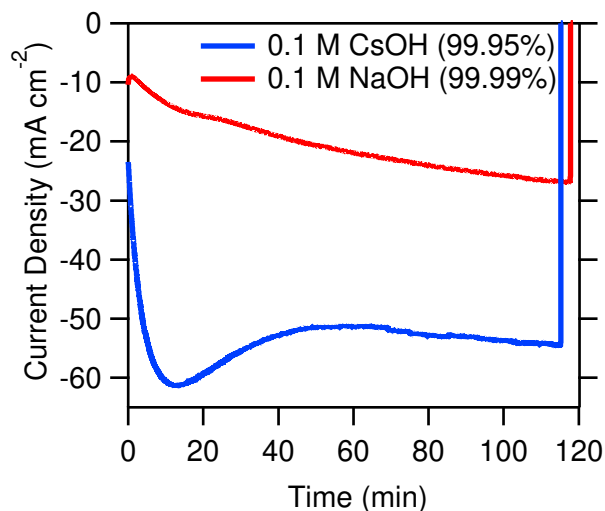


Figure 5.2: Current densities at constant applied potentials (-0.60 V vs. RHE for 0.1 M CsOH and -0.68 V vs. RHE for 0.1 M NaOH) prior to the interrogation of the Cu RDE with XPS.

below the detection limit.

The amount of iron that deposits during the measurement depends on the diffusion flux of iron species to the RDE, $J = Dc_b/\delta$ [184], where D , c_b , and δ are the diffusion coefficient, the bulk concentration of iron, and the diffusion layer thickness, respectively. Assuming $D = 1 \times 10^{-5} \text{ cm}^2 \text{ s}^{-1}$, $c_b = 240 \text{ nM}$, and $\delta = 10 \text{ }\mu\text{m}$, and that a monolayer is approximately equal to 2 nmol cm^{-2} , we find that a complete monolayer forms within ≈ 15 min. For this rough estimate, we assumed that every reducible ion that arrives at the electrode deposits on it. Although the electrode potential may not be sufficiently negative at all times to reduce iron impurities during the CV measurements, this result is a useful order-of-magnitude estimate. Because electrocatalytic processes can be affected by coverages well below a monolayer, this order-of-magnitude estimate shows that significant amounts of iron can deposit over the course of the CV experiments.

In summary, 0.1 M CsOH (99.95%) contains about six times more iron than 0.1 M NaOH (99.99%) (Table 5.1). A larger enhancement of the HER over the course of eleven CVs occurs in the former electrolyte (Figure 5.1). XPS confirms the presence of iron on the

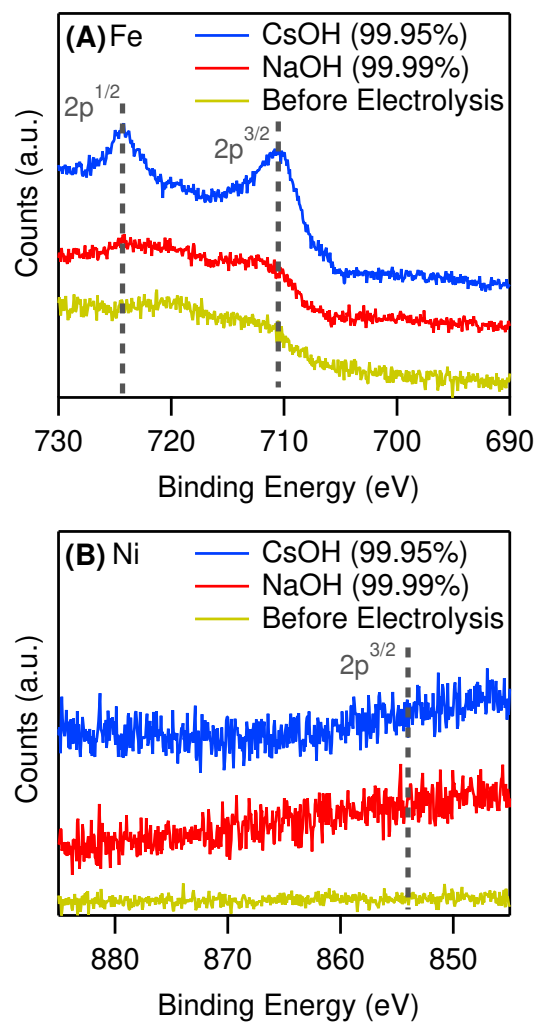


Figure 5.3: X-ray photoelectron spectra of the Cu RDE before and after 1.9 h of electrolysis in the regions for (A) Fe and (B) Ni.

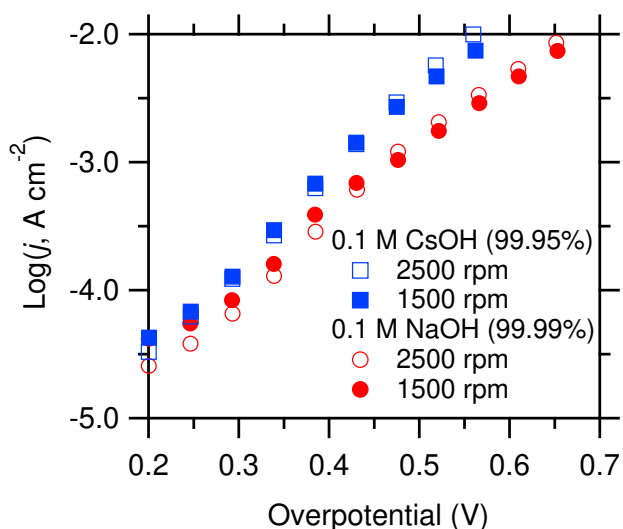


Figure 5.4: Logarithmic current densities as a function of overpotential during the cathodic forward scan of the second CV for each electrolyte at RDE rotation rates of 1500 rpm (solid markers) and 2500 rpm (hollow markers).

Cu RDE following prolonged electrolysis in 0.1 M CsOH (99.95%). Taken together, these findings show that the deposition of iron impurities is likely the origin of the HER activity changes during the CVs. It is probable that nickel also contributes to the enhancement, but this impurity apparently does not deposit as efficiently on the Cu RDE.

5.2.2 Impact of Iron Deposits on Tafel Slopes and Exchange Currents

To understand better how the trace iron impurities affect the HER on the Cu electrode, we conducted Tafel analyses of the current densities. Following established procedures [113], we restricted the analysis of the Tafel slope to overpotentials significantly larger than 1/2 of the absolute value of the Tafel slope (0.2 V), and to sufficiently small current densities at which no apparent mass transport limitations are expected ($< 10 \text{ mA cm}^{-2}$). Comparison of data collected at 1500 and 2500 rpm indicates the absence of transport limitations (Figure 5.4).

Figure 5.5 shows the 10-based logarithm of the current density as a function of overpo-

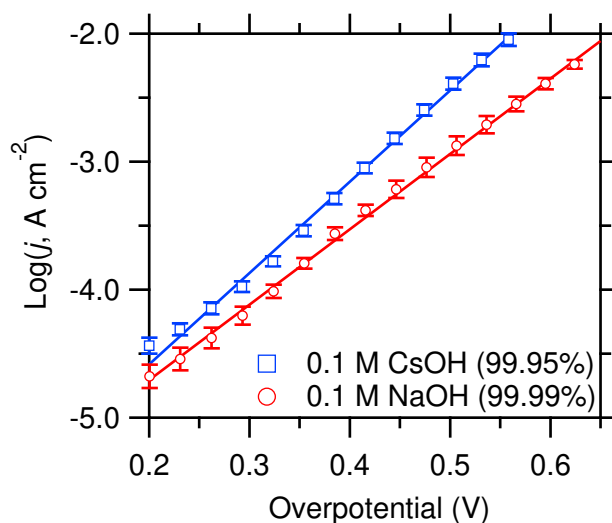


Figure 5.5: Tafel plots for the forward (cathodic) scans of the second CVs. The data represent the average of six independent experiments for each electrolyte. The error bars represent one standard deviation. For clarity, only a subset of the collected data points is shown on the plot. The Tafel plots for the 6th and 11th cycles are reported in Figure 5.6

tential during the cathodic forward scan of the second CV for each electrolyte. As shown in Table 5.3, the Tafel slope decreases with increasing cycle number in both electrolytes. Irrespective of the cycle number, the Tafel slope for the HER in CsOH (99.95%) is consistently smaller by $35 \pm 5 \text{ mV dec}^{-1}$ compared to that for the reaction in NaOH (99.99%). Interestingly, the exchange current densities slightly decrease by a factor of 2-3 over the course of the eleven CVs. Although this decrease may be an artifact of the extrapolation, it unequivocally shows that the promotion of the HER with cycle number is due to a decrease in the Tafel slope as iron deposits on the Cu electrode.

The Tafel slope is a function of the symmetry factor of the rate-determining step (RDS) of the reaction and the coverage of surface-adsorbed species [185]. It is possible that the deposition of iron switches the RDS to a different elementary step in the reaction mechanism or alters the value of the symmetry factor for the same RDS. However, the deposition of iron on the Cu electrode is also expected to significantly change the surface coverage of hydrogen. The absolute value of the binding energy of hydrogen to iron is

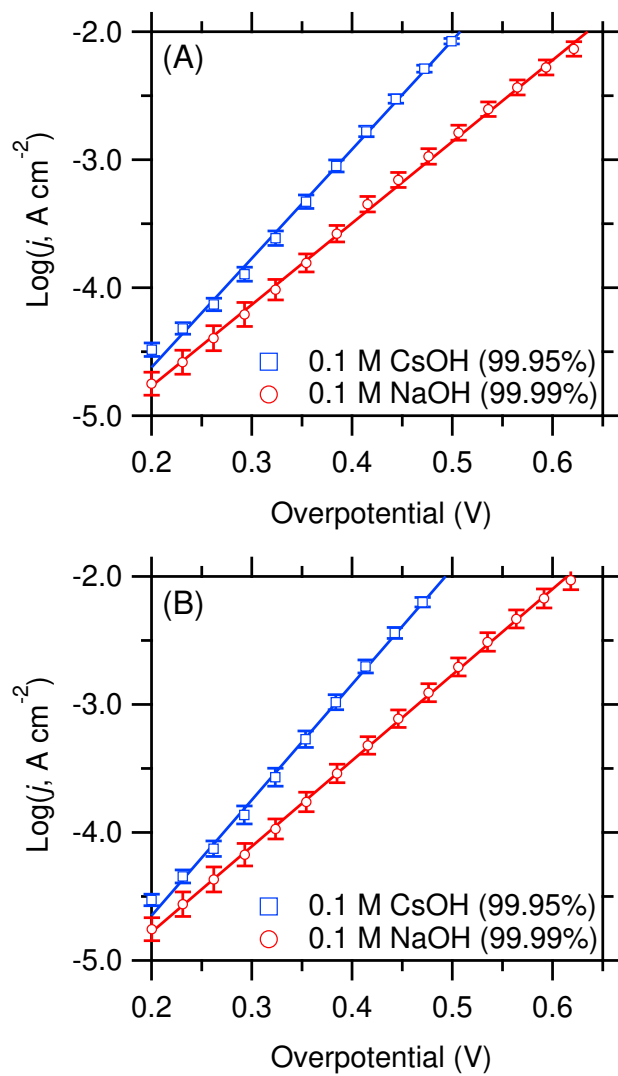


Figure 5.6: Tafel plots for the forward (cathodic) scans of the (A) 6th and (B) 11th CVs at pH 13.

Table 5.3: Tafel slopes and exchange current densities for the HER on Cu. The standard deviations are based on six independent measurements for each 0.1 M electrolyte prepared from the as-received hydroxide salts (NaOH (99.99%) and CsOH (99.95%)). The reported data were derived from the forward scan of the CVs.

Cycle	Tafel Slopes (mV dec ⁻¹)		log (j_0 , A cm ⁻²)	
	NaOH	CsOH	NaOH	CsOH
2	170 ± 7	140 ± 6	-5.88 ± 0.12	-6.01 ± 0.11
6	157 ± 5	117 ± 2	-6.12 ± 0.23	-6.33 ± 0.08
11	149 ± 5	111 ± 1	-6.12 ± 0.12	-6.46 ± 0.08

about 0.4 eV larger than the corresponding value for Cu [183]. If it is assumed that the RDS of the reaction is the Volmer step and that the reaction proceeds via the Volmer-Heyrovsky pathway, it is straightforward to show that the apparent transfer coefficient is $\alpha = \beta + \theta_{\text{H}}$, where β is the symmetry factor of the Volmer step and θ_{H} is the surface coverage of hydrogen. The Tafel slope is inversely proportional to the apparent transfer coefficient [185]. Therefore, the observed decrease in the Tafel slope with cycle number is consistent with an increase of the surface-coverage of hydrogen upon deposition of iron on the Cu electrode.

5.2.3 Impact of Iron on the HER at pH 9

To test if the enhancement of the HER by iron impurities also occurs at a lower pH, we prepared 0.1 M solutions of Na⁺ and Cs⁺ at a pH of 9 from the as-received alkali metal hydroxide salts. The pH of the solutions was adjusted with boric acid. In contrast to the observations at pH 13, the CVs were relatively stable with cycle number (Figure 5.7). The Tafel slopes of the HER in Na⁺- and Cs⁺-containing electrolytes at a pH of 9 are essentially identical (Figure 5.8). However, in comparison to the CVs, the steady-state current density in the electrolyte prepared from CsOH (99.95%) is significantly shifted towards more anodic potentials (Figure 5.7). This observation suggests that the deposition of iron on the Cu RDE is slower at pH 9 than at pH 13. The slower kinetics of iron deposition

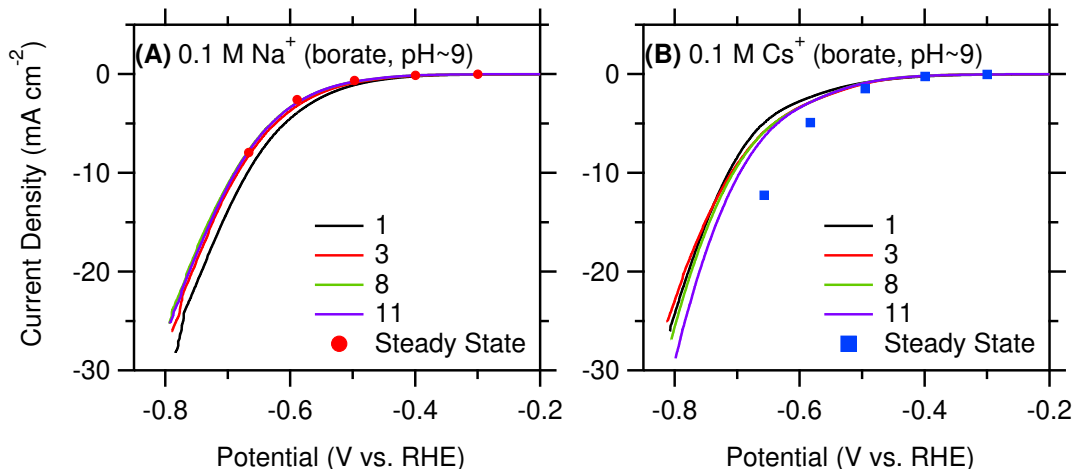


Figure 5.7: Consecutive CVs of a polycrystalline Cu RDE in 0.1 M (A) Na⁺ and (B) Cs⁺ electrolytes (pH \approx 9) prepared from NaOH (99.99%) and CsOH (99.95%) and boric acid. For clarity, only the forward scans of the CVs are shown. Steady state measurements were collected right after the eleventh CV.

could arise from a number of factors, including the presence of different predominant iron species in solution or pH-dependent electric double layer properties that render the deposition of iron on the electrode kinetically less favorable. These results show that for a given concentration of iron impurities, the rate enhancement of the HER increases with increasing pH.

5.2.4 Effects of Cations on the HER

To test if the HER is promoted by Cs⁺ relative to the reaction in Na⁺-containing electrolyte, we purified the alkali metal hydroxide solutions by pre-electrolysis. Details of the pre-electrolysis protocol are provided in the experimental procedures section. Figure 5.9 shows that the CVs of the polycrystalline Cu electrodes do not significantly change as a function of cycle number in the pre-electrolyzed electrolytes. This observation suggests that the pre-electrolysis procedure successfully removed trace impurities of iron. With ICP-AES, we confirmed that the concentration of iron in the pre-electrolyzed electrolytes was typically < 25 nM.

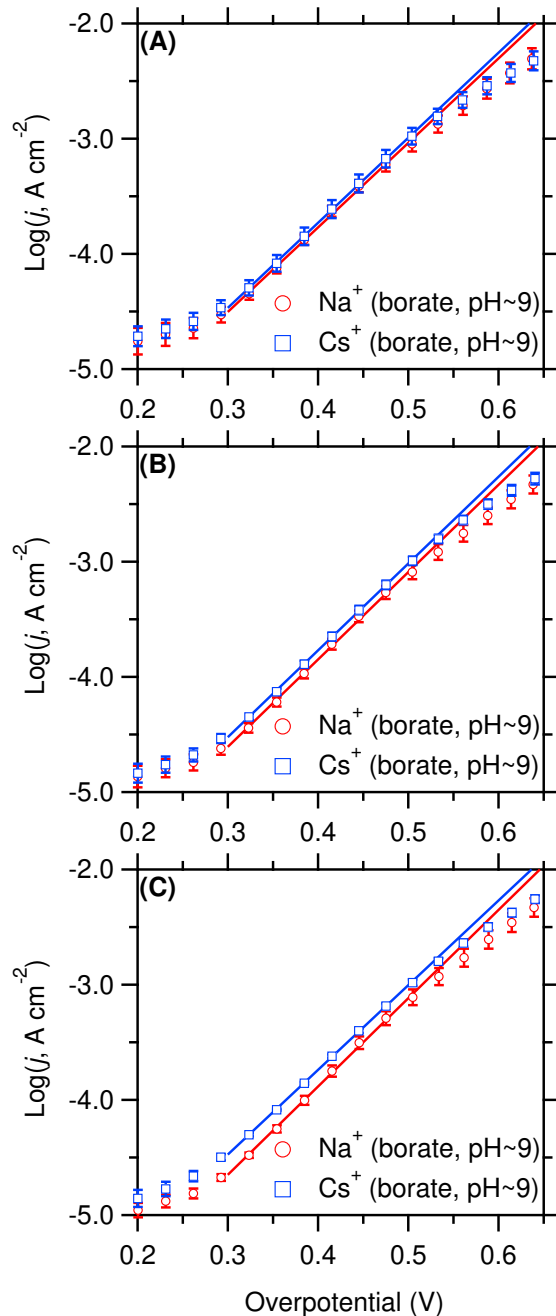


Figure 5.8: Tafel plots for the forward (cathodic) scans of the (A) 2nd, (B) 6th, and (C) 11th CVs in 0.1 M alkali metal borate electrolytes ($\text{pH} \approx 9$). The data represent the average of six independent experiments for each electrolyte. The error bars represent one standard deviation. For clarity, only a subset of the collected data points is shown on the plots.

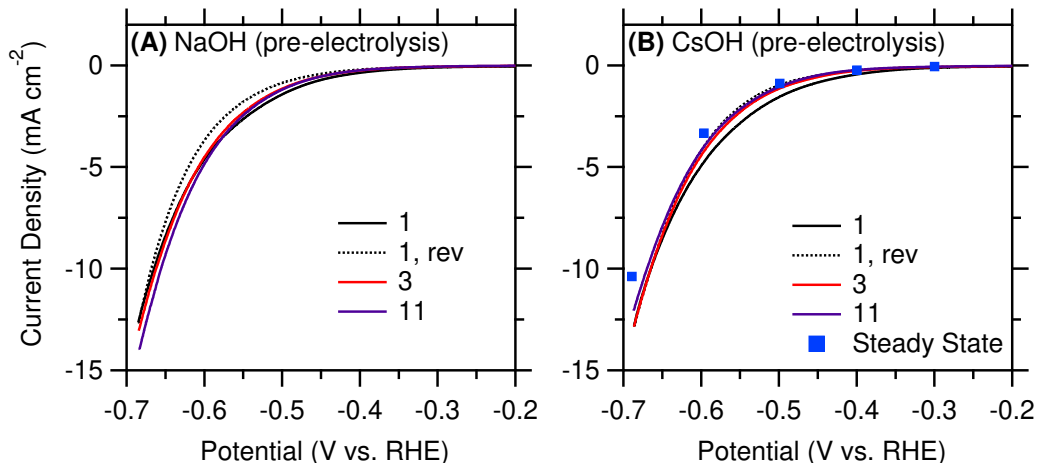


Figure 5.9: Consecutive CVs of a polycrystalline Cu RDE in 0.1 M solutions of pre-electrolyzed (A) NaOH and (B) CsOH. The CVs were taken at a scan rate of 10 mV s^{-1} and a rotation rate of 2500 rpm of the RDE. The numbers in the panels refer to the cycle number and “rev” denotes the respective reverse (anodic) scan. For clarity, the reverse scans of the other cycles are not shown. Steady state measurements in 0.1 M CsOH were collected right after the eleventh CV.

Comparison of the current densities in Figure 5.9A and B reveals that the HER proceeds at nearly the same rates in Na^+ - and Cs^+ -containing electrolytes. Indeed, the Tafel plots for the HER current densities in the two electrolytes mostly overlap (Figure 5.10). The extracted Tafel slopes ($163 \pm 3 \text{ mV dec}^{-1}$ in NaOH and $173 \pm 13 \text{ mV dec}^{-1}$ in CsOH) and exchange current densities ($\log[j_0, \text{A cm}^{-2}] = -6.05 \pm 0.09$ in NaOH and -5.83 ± 0.17 in CsOH) for the two different electrolytes are statistically not significantly different, indicating the absence of a detectable cation effect.

The observation that the switch from Na^+ - to Cs^+ -containing electrolyte has no measurable effect on the rate of the HER is surprising for the following reasons: First, the rates of other small-molecule electrocatalytic reactions are strongly affected when switching the cation of the supporting electrolyte from Na^+ to Cs^+ [27]. For example, the rate of ethylene formation during the reduction of CO_2 is enhanced by a factor of ≈ 6 in the presence of Cs^+ relative to that in Na^+ -containing electrolyte [22]. Cs^+ also shifts the half-wave potential of the oxygen evolution reaction on Pt by $\approx 50 \text{ mV}$ in the cathodic

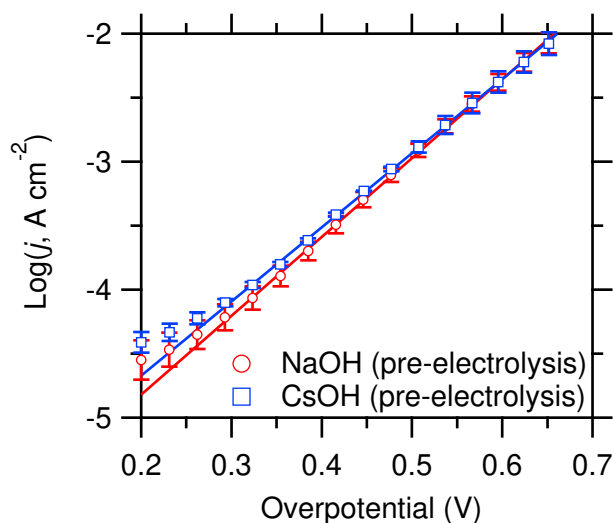


Figure 5.10: Tafel plots for the forward (cathodic) scans of the second CV in pre-electrolyzed electrolytes. The data represent the average of three independent experiments for each electrolyte. The error bars represent one standard deviation. For clarity, only a subset of the collected data points is shown on the plot.

direction relative to that in the presence of Na^+ [40]. These examples demonstrate that the two cations have the potential to structure the electric double layer in distinct ways that result in different electrocatalytic properties of the interface. Second, water has a large electric dipole moment (1.9 Debye) [168]. DFT models show that Cs^+ retains more charge upon its specific adsorption on metal surfaces compared to Na^+ [186]. Therefore, the water dissociation steps (Volmer and Heyrovsky reactions), which may involve water in the hydration shells of cations, are expected to be differently impacted by Cs^+ and Na^+ . Third, the concentration of hydronium ions is negligible at pH 13. As a result, alkali metal cations provide the counter charge in the electric double layer during cathodic polarization of the electrode. Fourth, low concentrations (10^{-2} - 10^{-4} M) of Li^+ and Ba^{2+} were shown to enhance the HER on Ir/Ru alloy electrodes in 0.1 M KOH by up to nearly a factor of two [187]. Similar enhancements of the HER on Pt were found when switching from 0.1 M CsOH to LiOH electrolyte [188]. Therefore, the absence of a measurable cation effect on the HER is not necessarily expected.

As discussed in a recent review article [27], there are numerous mechanisms by which cations can impact electrocatalytic processes. The predominant mechanism depends on the reaction conditions and electrode [27]. The prior observations of the dependence of the rate of the HER on cation identity are therefore not in contradiction of the results presented herein. Specifically, Danilovic *et al.* suggested that the hydrated cations are quasi-specifically adsorbed via surface-adsorbed hydroxide (OH_{ads}) on Ir/Ru alloys [187]. They hypothesized that these quasi-specifically adsorbed cations promote the HER by facilitating the dissociation of interfacial water. Such a mechanism is unlikely to be able to operate in the present case because the onset potential of the HER on Cu is about ≈ 300 mV more cathodic than on the Ir/Ru alloys. Under these cathodic potentials, the coverage of hydroxide on Cu is expected to be small [55].

DFT models suggest that the specific adsorption of cations is possible under the experimental conditions employed in this work [162, 186]. The absence of a measurable difference in the rate of the HER in Na^+ - versus Cs^+ -containing electrolyte suggests that the cation-specific electric fields are not significantly different from the perspective of the reacting water and/or that the surface-coverage of cations is not sufficiently large to impact the catalytic turnover.

5.2.5 DFT Examination of the Effects of Cations on HER Elementary Processes

To rationalize further our experimental findings, our collaborator N. Agrawal, H. Montalvo-Castro and M. J. Janik used DFT calculations to examine possible impacts of alkali metal cations on HER elementary processes. They found that the presence of alkali metal cations has minor impact on H interaction with the Cu surface. Further, an electric field difference of $0.3 \text{ V } \text{\AA}^{-1}$ would be needed to produce a change in Volmer step barrier of ≈ 0.06 eV.

The electric field resulting from Na^+ and Cs^+ cations adsorbed on the Cu(100) surface was mapped, suggesting the Volmer step would need to occur at distances closer than the first hydration shell of the cations to experience electric fields sufficient to alter the HER kinetics. These DFT results corroborate the reported experimental results that alkali metal cations have insignificant impact on HER kinetics on Cu electrodes.

5.3 Conclusions

Herein, we investigated the effects of trace iron impurities and alkali metal cations on the HER on polycrystalline Cu electrodes in alkaline conditions. We found that iron impurities in commercially available hydroxide salts of the highest purity grades deposit on a Cu RDE over a timescale of tens of minutes. The deposition of iron leads to a substantial acceleration of the rate of the HER in 0.1 M CsOH (99.95%) by up to a factor of five over the course of eleven CVs. By contrast, at a lower pH of 9, the rate of iron deposition from an electrolyte of the same purity is markedly slower. The iron impurities can be effectively removed by pre-electrolyzing the solutions. In purified 0.1 M NaOH and CsOH, the HER current densities are almost identical, indicating the absence of a significant cation effect on the HER on Cu. In line with this experimental observation, DFT model indicates that the surface binding energy of hydrogen, a descriptor of the HER, is only minimally perturbed by 1/9 of a monolayer of co-adsorbed cations. Further, the activation barrier of the Volmer elementary step of the HER is relatively insensitive to changes in the local electric field below $\approx 0.3 \text{ V \AA}^{-1}$. Our findings show that Cs^+ can be employed to selectively promote desirable reaction, such as CO_2 reduction, in alkaline conditions. The thorough removal of trace iron impurities is essential for the effective suppression of the HER.

5.4 Experimental Procedures

5.4.1 Materials

Sodium hydroxide (99.99%) was obtained from MilliporeSigma. Cesium hydroxide monohydrate (99.95%; Acros Organics), nitric acid (TraceMetal grade, 67-70%; Fisher) and boric acid (Puratronic 99.9995%; Alfa Aesar) were acquired from Fisher Scientific. Ar (ultra high purity) was obtained from Air Gas (Radnor, PA).

5.4.2 Electrode Preparation

The custom-built RDE consisted of a Cu rod (5 mm diameter, 99.999%, Fisher Scientific; Waltham, MA) that was installed in a polyether ether ketone (PEEK) holder. The RDE was polished to a mirror finish with 1 μm diamond paste (Ted Pella; Redding, CA) for 10 min and 0.3 μm alumina slurry (Electron Microscopy Sciences; Hartfield, PA) for 3 min. Then, the RDE was sonicated in high-purity water for 10 min and dried under a stream of ultra high-purity N_2 . The RDE was then electropolished in a mixture of H_3PO_4 (85 wt.%) : H_2O : H_2SO_4 (95 wt.%) (volume ratio of 10:5:2) [177]. The electropolishing protocol consisted of two independent segments of chronopotentiometry for 2 s at a current density of 100 $\mu\text{A cm}^{-2}$ and a 30 s interval at open circuit potential in between them. Then, the RDE was thoroughly rinsed with high-purity water and installed in the electrochemical cell.

5.4.3 Electrochemical Measurements

Electrochemical measurements were carried out in a two-compartment As-free glass cell separated by a Selemion AHO ion exchange membrane (AGC Engineering Co.; Chiba, Japan). 65 ml and 15 ml of electrolyte were used for the working and counter electrode

compartments, respectively. 0.1 M NaOH or CsOH electrolyte was freshly prepared right before each experiment from the corresponding 1 M stock solution that was stored in a plastic bottle. The pH of the bulk electrolyte was ≈ 12.8 for 0.1 M NaOH and ≈ 12.9 for 0.1 M CsOH. The electrolyte of pH 9 was prepared by titrating the corresponding alkali hydroxide solution with boric acid. The final concentration of alkali cations was 0.1 M. Data collection was typically completed within one hour.

The electrolyte was purged with ultra high-purity Ar at a flow rate of 30 standard cubic centimeters per minute (sccm) in the working electrode compartment and 10 sccm in the counter electrode compartment for 15 min before the start of the measurement. Purging was continued until completion of the experiment. An Au wire (Premion 99.999%, 0.5 mm diameter; Alfa Aesar) was used as the counter electrode and an Hg/HgO electrode (EF1369, 1 M NaOH; BASi Inc.; West Lafayette, IN) was used as the reference electrode. The potential of the Hg/HgO reference electrode was routinely checked against a saturated calomel electrode to ensure electrode stability. A VSP electrochemical workstation (Biologic; Knoxville, TN) was used to control the potential. The surface roughness of the electrode was determined by electrochemical capacitance measurements [55].

Eleven consecutive CVs with turning potentials of 0.15 and ≈ -0.65 V versus RHE at a scan rate of 10 mV s^{-1} were carried out in 0.1 M NaOH and CsOH. For Na^+ and Cs^+ -containing electrolytes at a pH of 9, CVs from 0.0 to ≈ -0.9 V versus RHE were carried out. The 2nd, 6th, and 11th cycles were used for Tafel analysis. The real cathodic turning potentials slightly varied for consecutive CVs because 15% of the iR -drop was manually corrected following the measurements. Following the CVs, steady state measurements were carried out. Five potential steps were selected. At each potential step, the potential was held for 3 min and the average of the last minute was used for analysis.

The applied potential versus the Hg/HgO electrode was converted to the RHE scale by application of the equation: $E_{\text{RHE}} = E_{\text{Hg/HgO}} + 0.147 \text{ V} + \text{pH} \times 0.059 \text{ V}$. The solution

resistance between reference and working electrodes was ≈ 40 Ohms for 0.1 M alkali metal hydroxide electrolytes and ≈ 110 Ohms for pH 9 electrolytes. 85% of the iR -drop was compensated by the potentiostat during the experiment. The remaining 15% of the iR drop was manually corrected after completion of the experiment according to: $E_{\text{real}} = E_{\text{measured}} - iR_{\text{u}}$, where R_{u} is the uncompensated resistance. All reported current densities are based on the geometric area of the RDE.

5.4.4 Pre-electrolysis

80 ml of 0.1 M NaOH or CsOH electrolyte was prepared from the corresponding 1 M stock solution. Two pieces of Cu foil (Puratronic 99.999%, 0.025 mm; Alfa Aesar) were used as working and counter electrodes. The surface area of the working electrode was 12.5 cm². The electrolysis was carried out in a polypropene bottle under stirring of the electrolyte at 200 rpm and under purging of the electrolyte with Ar at 10 sccm. The applied potential was -2 V versus a Cu rod. The electrodes were removed from the electrolyte under applied bias after ≈ 20 hours. Deep red precipitate (Cu oxides from oxidation of the Cu anode) was removed by filtration of the electrolyte with a 0.22 μm polytetrafluoroethylene syringe filter (Fisherbrand).

5.4.5 X-ray Photoelectron Spectroscopy (XPS)

The X-ray photoelectron spectra were collected on a Surface Science S-Probe ESCA with an Al K α X-ray source. Narrow scans over peaks of interest were collected with a step size of 0.065 eV. The operating pressure was $\approx 10^{-7}$ torr. The X-ray spot was 300 μm in diameter. The X-ray source was operated at 5 mA and 10 kV.

5.4.6 Inductively Coupled Plasma - Atomic Emission Spectroscopy (ICP-AES)

Samples were prepared by adding 86 μl of 70% HNO_3 to 3 ml of the 0.1 M alkali metal hydroxide solution. The samples were analyzed on an Agilent 5100 ICP-AES instrument. Calibration curves for Ni and Fe were derived from standard solutions (25, 50, 100, 250, 500, 1000 nM) of the corresponding salts.

5.5 Acknowledgements

This work was supported by a CAREER award from the National Science Foundation (Award No.: CHE-1847841).

5.6 Original Publication

This chapter has been published: Li X,* Gunathunge C M, Agrawal N, Montalvo-Castro H, Jin J, Janik M J & Waagele, M. M. Impact of alkali metal cations and iron impurities on the evolution of hydrogen on Cu electrodes in alkaline electrolytes *Journal of The Electrochemical Society*, **167**, 106505 (2020).

Chapter 6

Summary and Future Perspective

In this thesis, we have revealed that the electrode surface morphology is subject to reversible reconstruction under the CO₂ reduction reaction conditions and the effect of interfacial electric field and interfacial water on CO reduction product selectivity. We utilized adsorbed CO, which is a key intermediate for CO/CO₂ reduction, as the *in-situ* molecular probe in both surface-enhanced infrared absorption spectroscopy and surface-enhanced Raman spectroscopy. By analyzing the potential-dependent lineshape and peak frequency for the probe molecule, the properties of the electrode/electrolyte interface have been investigated. We have also connected the interfacial properties to the electrocatalytic performance of the Cu electrode for CO reduction. We have utilized differential electrochemical mass spectrometry to realize the online detection of the product generated at the vicinity of the Cu electrode.

We have shown evidence of Cu electrode surface morphology being subject to reversible surface reconstruction under the CO₂ reduction conditions. This reconstruction is induced by the adsorbed CO intermediate. The newly generated adsorption sites by the reconstruction shows $\approx 30 \text{ cm}^{-1}$ difference in the vibrational frequency of CO_{ads} to the original adsorption sites. Such a significant difference is expected to have profound effects on the electrocatalytic properties of the Cu electrode. Apart from the electrode surface morphology, cations in the supporting electrolyte also play a key role in the elec-

trocatalysis. We have demonstrated that interfacial water molecules at Cu electrodes can be displaced by propyl₄N⁺ and butyl₄N⁺, which disturbs the interaction between the interfacial H₂O and CO_{ads}. This interaction is supposed to stabilize a key intermediate, the CO dimer, for ethylene evolution. The presence of propyl₄N⁺ or butyl₄N⁺ in the interfacial region destroys the stabilization and then blocks ethylene evolution. We have also revealed that the hydrogen evolution on the Cu electrodes occurs at essentially identical rates in Na⁺ and Cs⁺-containing electrolytes under alkaline conditions. This finding suggests Cs⁺ can be employed to selectively promote desirable reaction, such as CO₂ reduction.

Here we propose some possible directions that may help to further understanding the relationship of the interface properties and the electrocatalytic performance:

- The Cu film used for CO₂/CO reduction investigation by SEIRAS is mainly polycrystalline Cu. Development of new techniques that allows *in-situ* intermediate detection on specific Cu facets will help to gather more supportive evidence.
- CO_{ads} is a powerful probe molecule for the electrode/electrolyte interfacial properties for both SEIRAS and Raman spectroscopy. However, CO_{ads} is also an on-pathway intermediate for CO/CO₂ reduction. The CO_{ads} coverage changes with the applied potential, which can introduce coverage-dependent shift of the CO peak frequency. In the further investigation, if any electrochemical inert surface-adsorbed molecules can be used as the probe molecule, it will provide a wider potential range to analyze the interfacial properties. For example, Sorenson et al. have employed 4-mercaptobenzonitrile to learn the interfacial electric field by vibrational sum frequency generation on the Au surface [154]. Similar molecules with the nitrile (CN) functional group can also be used in the study with SEIRAS and Raman spectroscopy.

Bibliography

1. Orella, M. J., Román-Leshkov, Y. & Brushett, F. R. Emerging opportunities for electrochemical processing to enable sustainable chemical manufacturing. *Current Opinion in Chemical Engineering* **20**. Nanotechnology / Separation Engineering, 159–167. ISSN: 2211-3398. <http://www.sciencedirect.com/science/article/pii/S2211339817300977> (2018).
2. Van der Ham, C. J. M., Koper, M. T. M. & Hetterscheid, D. G. H. Challenges in reduction of dinitrogen by proton and electron transfer. *Chem. Soc. Rev.* **43**, 5183–5191. <http://dx.doi.org/10.1039/C4CS00085D> (15 2014).
3. Suryanto, B. H. R., Du, H.-L., Wang, D., Chen, J., Simonov, A. N. & MacFarlane, D. R. Challenges and prospects in the catalysis of electroreduction of nitrogen to ammonia. *Nature Catalysis* **2**, 290–296. ISSN: 2520-1158. <https://doi.org/10.1038/s41929-019-0252-4> (2019).
4. Bushuyev, O. S., Luna, P. D., Dinh, C. T., Tao, L., Saur, G., van de Lagemaat, J., Kelley, S. O. & Sargent, E. H. What Should We Make with CO₂ and How Can We Make It? *Joule* **2**, 825–832. <http://www.sciencedirect.com/science/article/pii/S2542435117300764> (2018).
5. Denholm, P., Clark, K. & O’Connell, M. *On the path to sunshot-emerging issues and challenges in integrating high levels of solar into the electrical generation and transmission system* tech. rep. (EERE Publication and Product Library, 2016).

6. Energy, G. *Western wind and solar integration study* tech. rep. (National Renewable Energy Lab.(NREL), Golden, CO (United States), 2010).
7. Kortlever, R., Shen, J., Schouten, K. J. P., Calle-Vallejo, F. & Koper, M. T. M. Catalysts and Reaction Pathways for the Electrochemical Reduction of Carbon Dioxide. *The Journal of Physical Chemistry Letters* **6**, 4073–4082. <https://doi.org/10.1021/acs.jpcclett.5b01559> (2015).
8. Lu, Q. & Jiao, F. Electrochemical CO₂ reduction: Electrocatalyst, reaction mechanism, and process engineering. *Nano Energy* **29**. Electrocatalysis, 439–456. ISSN: 2211-2855. <http://www.sciencedirect.com/science/article/pii/S2211285516300568> (2016).
9. Nwabara, U. O., Cofell, E. R., Verma, S., Negro, E. & Kenis, P. J. A. Durable Cathodes and Electrolyzers for the Efficient Aqueous Electrochemical Reduction of CO₂. *ChemSusChem* **13**, 855–875. eprint: <https://chemistry-europe.onlinelibrary.wiley.com/doi/pdf/10.1002/cssc.201902933>. <https://chemistry-europe.onlinelibrary.wiley.com/doi/abs/10.1002/cssc.201902933> (2020).
10. Kibria, M. G., Edwards, J. P., Gabardo, C. M., Dinh, C.-T., Seifitokaldani, A., Sinton, D. & Sargent, E. H. Electrochemical CO₂ Reduction into Chemical Feedstocks: From Mechanistic Electrocatalysis Models to System Design. *Advanced Materials* **31**, 1807166. eprint: <https://onlinelibrary.wiley.com/doi/pdf/10.1002/adma.201807166>. <https://onlinelibrary.wiley.com/doi/abs/10.1002/adma.201807166> (2019).
11. Montoya, J. H., Seitz, L. C., Chakthranont, P., Vojvodic, A., Jaramillo, T. F. & Nørskov, J. K. Materials for solar fuels and chemicals. *Nature Materials* **16**, 70–81. ISSN: 1476-4660. <https://doi.org/10.1038/nmat4778> (2017).

12. Dinh, C.-T., Burdyny, T., Kibria, M. G., Seifitokaldani, A., Gabardo, C. M., García de Arquer, F. P., Kiani, A., Edwards, J. P., De Luna, P., Bushuyev, O. S., Zou, C., Quintero-Bermudez, R., Pang, Y., Sinton, D. & Sargent, E. H. CO₂ electroreduction to ethylene via hydroxide-mediated copper catalysis at an abrupt interface. *Science* **360**, 783–787. ISSN: 0036-8075. eprint: <https://science.sciencemag.org/content/360/6390/783.full.pdf>. <https://science.sciencemag.org/content/360/6390/783> (2018).
13. Horn, E. J., Rosen, B. R. & Baran, P. S. Synthetic Organic Electrochemistry: An Enabling and Innately Sustainable Method. *ACS Central Science* **2**, 302–308. ISSN: 2374-7943. <https://doi.org/10.1021/acscentsci.6b00091> (2016).
14. Yan, M., Kawamata, Y. & Baran, P. S. Synthetic Organic Electrochemical Methods Since 2000: On the Verge of a Renaissance. *Chemical Reviews* **117**, 13230–13319. ISSN: 0009-2665. <https://doi.org/10.1021/acs.chemrev.7b00397> (2017).
15. Popović, S., Smiljanić, M., Jovanović, P., Vavra, J., Buonsanti, R. & Hodnik, N. Stability and Degradation Mechanisms of Copper-Based Catalysts for Electrochemical CO₂ Reduction. *Angewandte Chemie International Edition* **59**, 14736–14746. eprint: <https://onlinelibrary.wiley.com/doi/pdf/10.1002/anie.202000617>. <https://onlinelibrary.wiley.com/doi/abs/10.1002/anie.202000617> (2020).
16. Kuhl, K. P., Cave, E. R., Abram, D. N. & Jaramillo, T. F. New insights into the electrochemical reduction of carbon dioxide on metallic copper surfaces. *Energy Environ. Sci.* **5**, 7050–7059. <http://dx.doi.org/10.1039/C2EE21234J> (5 2012).

17. Li, C. W. & Kanan, M. W. CO₂ Reduction at Low Overpotential on Cu Electrodes Resulting from the Reduction of Thick Cu₂O Films. *Journal of the American Chemical Society* **134**, 7231–7234. ISSN: 0002-7863. <https://doi.org/10.1021/ja3010978> (2012).
18. Hori, Y., Konishi, H., Futamura, T., Murata, A., Koga, O., Sakurai, H. & Oguma, K. “Deactivation of copper electrode” in electrochemical reduction of CO₂. *Electrochimica Acta* **50**, 5354–5369. ISSN: 0013-4686. <http://www.sciencedirect.com/science/article/pii/S0013468605002410> (2005).
19. Roberts, F. S., Kuhl, K. P. & Nilsson, A. Electroreduction of Carbon Monoxide Over a Copper Nanocube Catalyst: Surface Structure and pH Dependence on Selectivity. *ChemCatChem* **8**, 1119–1124. eprint: <https://chemistry-europe.onlinelibrary.wiley.com/doi/pdf/10.1002/cctc.201501189>. <https://chemistry-europe.onlinelibrary.wiley.com/doi/abs/10.1002/cctc.201501189> (2016).
20. Pérez-Gallent, E., Marcandalli, G., Figueiredo, M. C., Calle-Vallejo, F. & Koper, M. T. M. Structure- and Potential-Dependent Cation Effects on CO Reduction at Copper Single-Crystal Electrodes. *Journal of the American Chemical Society* **139**, 16412–16419. ISSN: 0002-7863. <https://doi.org/10.1021/jacs.7b10142> (2017).
21. Arán-Ais, R. M., Gao, D. & Roldan Cuenya, B. Structure- and Electrolyte-Sensitivity in CO₂ Electroreduction. *Accounts of Chemical Research* **51**, 2906–2917. ISSN: 0001-4842. <https://doi.org/10.1021/acs.accounts.8b00360> (2018).
22. Resasco, J., Chen, L. D., Clark, E., Tsai, C., Hahn, C., Jaramillo, T. F., Chan, K. & Bell, A. T. Promoter Effects of Alkali Metal Cations on the Electrochemical Re-

- duction of Carbon Dioxide. *Journal of the American Chemical Society* **139**, 11277–11287. ISSN: 0002-7863. <https://doi.org/10.1021/jacs.7b06765> (2017).
23. Nesselberger, M., Roefzaad, M., Fayçal Hamou, R., Ulrich Biedermann, P., Schweinberger, F. F., Kunz, S., Schloegl, K., Wiberg, G. K. H., Ashton, S., Heiz, U., Mayrhofer, K. J. J. & Arenz, M. The effect of particle proximity on the oxygen reduction rate of size-selected platinum clusters. *Nature Materials* **12**, 919–924. <https://doi.org/10.1038/nmat3712> (2013).
24. Bumroongsakulsawat, P. & Kelsall, G. Effect of solution pH on CO: formate formation rates during electrochemical reduction of aqueous CO₂ at Sn cathodes. *Electrochimica Acta* **141**, 216–225. ISSN: 0013-4686. <http://www.sciencedirect.com/science/article/pii/S0013468614014492> (2014).
25. Gonçalves, M., Gomes, A., Condeço, J., Fernandes, T., Pardal, T., Sequeira, C. & Branco, J. Electrochemical conversion of CO₂ to C₂ hydrocarbons using different ex situ copper electrodeposits. *Electrochimica Acta* **102**, 388–392. ISSN: 0013-4686. <http://www.sciencedirect.com/science/article/pii/S0013468613006506> (2013).
26. Schouten, K. J. P., Qin, Z., Pérez Gallent, E. & Koper, M. T. M. Two Pathways for the Formation of Ethylene in CO Reduction on Single-Crystal Copper Electrodes. *Journal of the American Chemical Society* **134**, 9864–9867. ISSN: 0002-7863. <https://doi.org/10.1021/ja302668n> (2012).
27. Waegele, M. M., Gunathunge, C. M., Li, J. & Li, X. How cations affect the electric double layer and the rates and selectivity of electrocatalytic processes. *The Journal of Chemical Physics* **151**, 160902. eprint: <https://doi.org/10.1063/1.5124878>. <https://doi.org/10.1063/1.5124878> (2019).

28. De Luna, P., Quintero-Bermudez, R., Dinh, C.-T., Ross, M. B., Bushuyev, O. S., Todorovic, P., Regier, T., Kelley, S. O., Yang, P. & Sargent, E. H. Catalyst Electrodeposition Controls Morphology and Oxidation State for Selective Carbon Dioxide Reduction. *Nat. Catal.* **1**, 103–110. ISSN: 2520-1158. <https://doi.org/10.1038/s41929-017-0018-9> (2018).
29. Paik, W., Andersen, T. & Eyring, H. Kinetic studies of the electrolytic reduction of carbon dioxide on the mercury electrode. *Electrochimica Acta* **14**, 1217–1232. ISSN: 0013-4686. <http://www.sciencedirect.com/science/article/pii/0013468669870192> (1969).
30. Hori, Y. & Suzuki, S. Electrolytic Reduction of Carbon Dioxide at Mercury Electrode in Aqueous Solution. *Bulletin of the Chemical Society of Japan* **55**, 660–665. eprint: <https://doi.org/10.1246/bcsj.55.660>. <https://doi.org/10.1246/bcsj.55.660> (1982).
31. Murata, A. & Hori, Y. Product Selectivity Affected by Cationic Species in Electrochemical Reduction of CO₂ and CO at a Cu Electrode. *Bulletin of the Chemical Society of Japan* **64**, 123–127. eprint: <https://doi.org/10.1246/bcsj.64.123>. <https://doi.org/10.1246/bcsj.64.123> (1991).
32. Thorson, M. R., Siil, K. I. & Kenis, P. J. A. Effect of Cations on the Electrochemical Conversion of CO₂ to CO. *Journal of The Electrochemical Society* **160**, F69–F74. <https://doi.org/10.1149/2.052301jes> (2012).
33. Frumkin, A. N. Influence of cation adsorption on the kinetics of electrode processes. *Trans. Faraday Soc.* **55**, 156–167. <http://dx.doi.org/10.1039/TF9595500156> (0 1959).
34. McCrum, I. T., Hickner, M. A. & Janik, M. J. Quaternary Ammonium Cation Specific Adsorption on Platinum Electrodes: A Combined Experimental and Density

- Functional Theory Study. *Journal of The Electrochemical Society* **165**, F114–F121. <https://doi.org/10.1149/2.1351802jes> (2018).
35. Feaster, J. T., Jongerius, A. L., Liu, X., Urushihara, M., Nitopi, S. A., Hahn, C., Chan, K., Nørskov, J. K. & Jaramillo, T. F. Understanding the Influence of [EMIM]Cl on the Suppression of the Hydrogen Evolution Reaction on Transition Metal Electrodes. *Langmuir* **33**, 9464–9471. ISSN: 0743-7463. <https://doi.org/10.1021/acs.langmuir.7b01170> (2017).
36. Herasymenko, P & Šlendyk, I. Wasserstoffüberspannung und adsorption der ionen [Hydrogen evolution overpotential and adsorption of ions]. *Z Phys Chem A* **149**, 123–139 (1930).
37. Ikeda, O., Tamura, H. & Matsuda, Y. Specific adsorption effects of organic cation on the electroreduction of dimethylfumarate. *Journal of Electroanalytical Chemistry and Interfacial Electrochemistry* **111**, 345–358. ISSN: 0022-0728. <http://www.sciencedirect.com/science/article/pii/S0022072880800556> (1980).
38. Fawcett, W. R., Fedurco, M. & Opallo, M. The inhibiting effects of tetraalkylammonium cations on simple heterogeneous electron transfer reactions in polar aprotic solvents. *The Journal of Physical Chemistry* **96**, 9959–9964. ISSN: 0022-3654. <https://doi.org/10.1021/j100203a069> (1992).
39. Strmcnik, D., Kodama, K., van der Vliet, D., Greeley, J., Stamenkovic, V. R. & Marković, N. M. The role of non-covalent interactions in electrocatalytic fuel-cell reactions on platinum. *Nature Chemistry* **1**, 466–472. ISSN: 1755-4349. <https://doi.org/10.1038/nchem.330> (2009).
40. Strmcnik, D., van der Vliet, D. F., Chang, K.-C., Komanicky, V., Kodama, K., You, H., Stamenkovic, V. R. & Marković, N. M. Effects of Li⁺, K⁺, and Ba²⁺ Cations on

- the ORR at Model and High Surface Area Pt and Au Surfaces in Alkaline Solutions. *The Journal of Physical Chemistry Letters* **2**, 2733–2736. <https://doi.org/10.1021/jz201215u> (2011).
41. Singh, M. R., Kwon, Y., Lum, Y., Ager, J. W. & Bell, A. T. Hydrolysis of Electrolyte Cations Enhances the Electrochemical Reduction of CO₂ over Ag and Cu. *Journal of the American Chemical Society* **138**, 13006–13012. ISSN: 0002-7863. <https://doi.org/10.1021/jacs.6b07612> (2016).
 42. Ayemoba, O. & Cuesta, A. Spectroscopic Evidence of Size-Dependent Buffering of Interfacial pH by Cation Hydrolysis during CO₂ Electroreduction. *ACS Applied Materials & Interfaces* **9**, 27377–27382. ISSN: 1944-8244. <https://doi.org/10.1021/acsami.7b07351> (2017).
 43. Yamakata, A., Soeta, E., Ishiyama, T., Osawa, M. & Morita, A. Real-Time Observation of the Destruction of Hydration Shells under Electrochemical Force. *Journal of the American Chemical Society* **135**, 15033–15039. ISSN: 0002-7863. <https://doi.org/10.1021/ja408326d> (2013).
 44. Yamakata, A. & Osawa, M. Cation-dependent restructure of the electric double layer on CO-covered Pt electrodes: Difference between hydrophilic and hydrophobic cations. *Journal of Electroanalytical Chemistry* **800**. Special Issue in honor of Masatoshi Osawa, 19–24. ISSN: 1572-6657. <http://www.sciencedirect.com/science/article/pii/S1572665716307366> (2017).
 45. Fedurco, M., Kedzierzawski, P. & Augustynski, J. Effect of Multivalent Cations upon Reduction of Nitrate Ions at the Ag Electrode. *Journal of The Electrochemical Society* **146**, 2569–2572. <https://doi.org/10.1149/1.1391973> (1999).
 46. Stoffelsma, C., Rodriguez, P., Garcia, G., Garcia-Araez, N., Strmcnik, D., Marković, N. M. & Koper, M. T. M. Promotion of the Oxidation of Carbon Monoxide at

- Stepped Platinum Single-Crystal Electrodes in Alkaline Media by Lithium and Beryllium Cations. *Journal of the American Chemical Society* **132**, 16127–16133. ISSN: 0002-7863. <https://doi.org/10.1021/ja106389k> (2010).
47. Subbaraman, R., Tripkovic, D., Strmcnik, D., Chang, K.-C., Uchimura, M., Paulikas, A. P., Stamenkovic, V. & Markovic, N. M. Enhancing Hydrogen Evolution Activity in Water Splitting by Tailoring Li⁺-Ni(OH)₂-Pt Interfaces. *Science* **334**, 1256–1260. ISSN: 0036-8075. eprint: <https://science.sciencemag.org/content/334/6060/1256.full.pdf>. <https://science.sciencemag.org/content/334/6060/1256> (2011).
48. Suntivich, J., Perry, E. E., Gasteiger, H. A. & Shao-Horn, Y. The Influence of the Cation on the Oxygen Reduction and Evolution Activities of Oxide Surfaces in Alkaline Electrolyte. *Electrocatalysis* **4**, 49–55. ISSN: 1868-5994. <https://doi.org/10.1007/s12678-012-0118-x> (2013).
49. van der Vliet, D. F. & Koper, M. T. Electrochemistry of Pt (100) in alkaline media: A voltammetric study. *Surface Science* **604**, 1912–1918. ISSN: 0039-6028. <http://www.sciencedirect.com/science/article/pii/S0039602810003134> (2010).
50. Gunathunge, C. M., Ovalle, V. J. & Waagele, M. M. Probing promoting effects of alkali cations on the reduction of CO at the aqueous electrolyte/copper interface. *Phys. Chem. Chem. Phys.* **19**, 30166–30172. <http://dx.doi.org/10.1039/C7CP06087D> (44 2017).
51. Kim, Y.-G., Baricuatro, J. H., Javier, A., Gregoire, J. M. & Soriaga, M. P. The Evolution of the Polycrystalline Copper Surface, First to Cu(111) and Then to Cu(100), at a Fixed CO₂RR Potential: A Study by Operando EC-STM. *Langmuir* **30**, 15053–15056. ISSN: 0743-7463. <https://doi.org/10.1021/la504445g> (2014).

52. Ryu, J. & Surendranath, Y. Polarization-Induced Local pH Swing Promotes Pd-Catalyzed CO₂ Hydrogenation. *Journal of the American Chemical Society* **142**, 13384–13390. ISSN: 0002-7863. <https://doi.org/10.1021/jacs.0c01123> (2020).
53. Zhang, F. & Co, A. C. Direct Evidence of Local pH Change and the Role of Alkali Cation during CO₂ Electroreduction in Aqueous Media. *Angewandte Chemie International Edition* **59**, 1674–1681. eprint: <https://onlinelibrary.wiley.com/doi/pdf/10.1002/anie.201912637>. <https://onlinelibrary.wiley.com/doi/abs/10.1002/anie.201912637> (2020).
54. Koper, M. T. M. Theory of Multiple Proton-Electron Transfer Reactions and Its Implications for Electrocatalysis. *Chem. Sci.* **4**, 2710–2723. <http://dx.doi.org/10.1039/C3SC50205H> (2013).
55. Gunathunge, C. M., Ovalle, V. J., Li, Y., Janik, M. J. & Waagele, M. M. Existence of an Electrochemically Inert CO Population on Cu Electrodes in Alkaline pH. *ACS Catal.* **8**, 7507–7516. eprint: <https://doi.org/10.1021/acscatal.8b01552>. <https://doi.org/10.1021/acscatal.8b01552> (2018).
56. Zhao, Y., Chang, X., Malkani, A. S., Yang, X., Thompson, L., Jiao, F. & Xu, B. Speciation of Cu Surfaces During the Electrochemical CO Reduction Reaction. *Journal of the American Chemical Society* **142**, 9735–9743. ISSN: 0002-7863. <https://doi.org/10.1021/jacs.0c02354> (2020).
57. Chou, T.-C., Chang, C.-C., Yu, H.-L., Yu, W.-Y., Dong, C.-L., Velasco-Vélez, J.-J., Chuang, C.-H., Chen, L.-C., Lee, J.-F., Chen, J.-M. & Wu, H.-L. Controlling the Oxidation State of the Cu Electrode and Reaction Intermediates for Electrochemical CO₂ Reduction to Ethylene. *Journal of the American Chemical Society* **142**, 2857–

2867. ISSN: 0002-7863. <https://doi.org/10.1021/jacs.9b11126> (2020).
58. Tang, W., Peterson, A. A., Varela, A. S., Jovanov, Z. P., Bech, L., Durand, W. J., Dahl, S., Nørskov, J. K. & Chorkendorff, I. The importance of surface morphology in controlling the selectivity of polycrystalline copper for CO₂ electroreduction. *Phys. Chem. Chem. Phys.* **14**, 76–81. <http://dx.doi.org/10.1039/C1CP22700A> (1 2012).
59. Li, C. W., Ciston, J. & Kanan, M. W. Electroreduction of carbon monoxide to liquid fuel on oxide-derived nanocrystalline copper. *Nature* **508**, 504–507. ISSN: 1476-4687. <https://doi.org/10.1038/nature13249> (2014).
60. Reske, R., Mistry, H., Behafarid, F., Roldan Cuenya, B. & Strasser, P. Particle Size Effects in the Catalytic Electroreduction of CO₂ on Cu Nanoparticles. *Journal of the American Chemical Society* **136**, 6978–6986. ISSN: 0002-7863. <https://doi.org/10.1021/ja500328k> (2014).
61. Manthiram, K., Beberwyck, B. J. & Alivisatos, A. P. Enhanced Electrochemical Methanation of Carbon Dioxide with a Dispersible Nanoscale Copper Catalyst. *Journal of the American Chemical Society* **136**, 13319–13325. ISSN: 0002-7863. <https://doi.org/10.1021/ja5065284> (2014).
62. Sen, S., Liu, D. & Palmore, G. T. R. Electrochemical Reduction of CO₂ at Copper Nanofoams. *ACS Catalysis* **4**, 3091–3095. <https://doi.org/10.1021/cs500522g> (2014).
63. Raciti, D., Livi, K. J. & Wang, C. Highly Dense Cu Nanowires for Low-Overpotential CO₂ Reduction. *Nano Letters* **15**, 6829–6835. ISSN: 1530-6984. <https://doi.org/10.1021/acs.nanolett.5b03298> (2015).

64. Roberts, F. S., Kuhl, K. P. & Nilsson, A. High Selectivity for Ethylene from Carbon Dioxide Reduction over Copper Nanocube Electrocatalysts. *Angewandte Chemie International Edition* **54**, 5179–5182. <https://onlinelibrary.wiley.com/doi/abs/10.1002/anie.201412214> (2015).
65. Verdaguer-Casadevall, A., Li, C. W., Johansson, T. P., Scott, S. B., McKeown, J. T., Kumar, M., Stephens, I. E. L., Kanan, M. W. & Chorkendorff, I. Probing the Active Surface Sites for CO Reduction on Oxide-Derived Copper Electrocatalysts. *Journal of the American Chemical Society* **137**, 9808–9811. ISSN: 0002-7863. <https://doi.org/10.1021/jacs.5b06227> (2015).
66. Kas, R., Kortlever, R., Yilmaz, H., Koper, M. T. M. & Mul, G. Manipulating the Hydrocarbon Selectivity of Copper Nanoparticles in CO₂ Electroreduction by Process Conditions. *ChemElectroChem* **2**, 354–358. <https://chemistry-europe.onlinelibrary.wiley.com/doi/abs/10.1002/celc.201402373> (2015).
67. Feng, X., Jiang, K., Fan, S. & Kanan, M. W. Grain-Boundary-Dependent CO₂ Electroreduction Activity. *Journal of the American Chemical Society* **137**, 4606–4609. ISSN: 0002-7863. <https://doi.org/10.1021/ja5130513> (2015).
68. Loiudice, A., Lobaccaro, P., Kamali, E. A., Thao, T., Huang, B. H., Ager, J. W. & Buonsanti, R. Tailoring Copper Nanocrystals towards C₂ Products in Electrochemical CO₂ Reduction. *Angewandte Chemie International Edition* **55**, 5789–5792. eprint: <https://onlinelibrary.wiley.com/doi/pdf/10.1002/anie.201601582>. <https://onlinelibrary.wiley.com/doi/abs/10.1002/anie.201601582> (2016).
69. Ma, M., Djanashvili, K. & Smith, W. A. Controllable Hydrocarbon Formation from the Electrochemical Reduction of CO₂ over Cu Nanowire Arrays. *Angewandte*

- Chemie International Edition* **55**, 6680–6684. eprint: <https://onlinelibrary.wiley.com/doi/pdf/10.1002/anie.201601282>. <https://onlinelibrary.wiley.com/doi/abs/10.1002/anie.201601282> (2016).
70. Li, Y., Cui, F., Ross, M. B., Kim, D., Sun, Y. & Yang, P. Structure-Sensitive CO₂ Electroreduction to Hydrocarbons on Ultrathin 5-fold Twinned Copper Nanowires. *Nano Letters* **17**, 1312–1317. ISSN: 1530-6984. <https://doi.org/10.1021/acs.nanolett.6b05287> (2017).
71. Durand, W. J., Peterson, A. A., Studt, F., Abild-Pedersen, F. & Nørskov, J. K. Structure effects on the energetics of the electrochemical reduction of CO₂ by copper surfaces. *Surface Science* **605**, 1354–1359. ISSN: 0039-6028. <http://www.sciencedirect.com/science/article/pii/S0039602811001658> (2011).
72. Hori, Y., Koga, O., Yamazaki, H. & Matsuo, T. Infrared spectroscopy of adsorbed CO and intermediate species in electrochemical reduction of CO₂ to hydrocarbons on a Cu electrode. *Electrochimica Acta* **40**, 2617–2622. ISSN: 0013-4686. <http://www.sciencedirect.com/science/article/pii/001346869500239B> (1995).
73. Hori, Y., Takahashi, I., Koga, O. & Hoshi, N. Selective Formation of C₂ Compounds from Electrochemical Reduction of CO₂ at a Series of Copper Single Crystal Electrodes. *The Journal of Physical Chemistry B* **106**, 15–17. ISSN: 1520-6106. <https://doi.org/10.1021/jp013478d> (2002).
74. Hori, Y., Takahashi, I., Koga, O. & Hoshi, N. Electrochemical reduction of carbon dioxide at various series of copper single crystal electrodes. *Journal of Molecular Catalysis A: Chemical* **199**. Special Issue dedicated to Professor Juro Horiuti in commemoration of his centennial birthday and his contribution to science., 39 –

47. ISSN: 1381-1169. <http://www.sciencedirect.com/science/article/pii/S1381116903000165> (2003).
75. Schouten, K. J. P., Pérez Gallent, E. & Koper, M. T. M. Structure Sensitivity of the Electrochemical Reduction of Carbon Monoxide on Copper Single Crystals. *ACS Catalysis* **3**, 1292–1295. <https://doi.org/10.1021/cs4002404> (2013).
76. Luo, W., Nie, X., Janik, M. J. & Asthagiri, A. Facet Dependence of CO₂ Reduction Paths on Cu Electrodes. *ACS Catalysis* **6**, 219–229. <https://doi.org/10.1021/acscatal.5b01967> (2016).
77. Huang, Y., Handoko, A. D., Hirunsit, P. & Yeo, B. S. Electrochemical Reduction of CO₂ Using Copper Single-Crystal Surfaces: Effects of CO* Coverage on the Selective Formation of Ethylene. *ACS Catalysis* **7**, 1749–1756. <https://doi.org/10.1021/acscatal.6b03147> (2017).
78. Somorjai, G. A. & Li, Y. *Introduction to surface chemistry and catalysis* (John Wiley & Sons, 2010).
79. Kim, Y.-G., Javier, A., Baricuatro, J. H., Torelli, D., Cummins, K. D., Tsang, C. F., Hemminger, J. C. & Soriaga, M. P. Surface reconstruction of pure-Cu single-crystal electrodes under CO-reduction potentials in alkaline solutions: A study by serial ECSTM-DEMS. *Journal of Electroanalytical Chemistry* **780**, 290–295. ISSN: 1572-6657. <http://www.sciencedirect.com/science/article/pii/S1572665716304866> (2016).
80. Eren, B., Zherebetsky, D., Patera, L. L., Wu, C. H., Bluhm, H., Africh, C., Wang, L.-W., Somorjai, G. A. & Salmeron, M. Activation of Cu(111) surface by decomposition into nanoclusters driven by CO adsorption. *Science* **351**, 475–478. ISSN: 0036-8075. eprint: <https://science.sciencemag.org/content/>

351/6272/475.full.pdf. <https://science.sciencemag.org/content/351/6272/475> (2016).

81. Eren, B., Liu, Z., Stacchiola, D., Somorjai, G. A. & Salmeron, M. Structural Changes of Cu(110) and Cu(110)-(2 × 1)-O Surfaces under Carbon Monoxide in the Torr Pressure Range Studied with Scanning Tunneling Microscopy and Infrared Reflection Absorption Spectroscopy. *The Journal of Physical Chemistry C* **120**, 8227–8231. ISSN: 1932-7447. <https://doi.org/10.1021/acs.jpcc.6b02143> (2016).
82. Bare, S. R., Hofmann, P. & King, D. A. Vibrational studies of the surface phases of CO on Pt110 at 300 K. *Surface Science* **144**, 347–369. ISSN: 0039-6028. <http://www.sciencedirect.com/science/article/pii/0039602884901067> (1984).
83. Chang, S.-C. & Weaver, M. J. In-situ infrared spectroscopy of CO adsorbed at ordered Pt(110)-aqueous interfaces. *Surface Science* **230**, 222–236. ISSN: 0039-6028. <http://www.sciencedirect.com/science/article/pii/003960289090030C> (1990).
84. Zou, S., Gómez, R. & Weaver, M. J. Infrared spectroscopy of carbon monoxide at the ordered palladium (110)-aqueous interface: evidence for adsorbate-induced surface reconstruction. *Surface Science* **399**, 270–283. ISSN: 0039-6028. <http://www.sciencedirect.com/science/article/pii/S0039602897008261> (1998).
85. Ferri, D., Bürgi, T. & Baiker, A. Pt and Pt/Al₂O₃ Thin Films for Investigation of Catalytic SolidLiquid Interfaces by ATR-IR Spectroscopy: CO Adsorption, H₂-Induced Reconstruction and Surface-Enhanced Absorption. *The Journal of Physi-*

- cal Chemistry B* **105**, 3187–3195. ISSN: 1520-6106. <https://doi.org/10.1021/jp002268i> (2001).
86. Ferraro, J. R., Nakamoto, K. & Brown, C. W. *Introductory Raman Spectroscopy* (Academic press, 2003).
87. Harris, D. C. & Bertolucci, M. D. *Symmetry and spectroscopy: an introduction to vibrational and electronic spectroscopy* (Courier Corporation, 1989).
88. RAMAN, C. V. & KRISHNAN, K. S. The Negative Absorption of Radiation. *Nature* **122**, 12–13. ISSN: 1476-4687. <https://doi.org/10.1038/122012b0> (1928).
89. Fleischmann, M., Hendra, P. & McQuillan, A. Raman spectra of pyridine adsorbed at a silver electrode. *Chemical Physics Letters* **26**, 163 –166. ISSN: 0009-2614. <http://www.sciencedirect.com/science/article/pii/0009261474853881> (1974).
90. Kneipp, K., Moskovits, M. & Kneipp, H. *Surface-enhanced Raman scattering: physics and applications* (Springer Science & Business Media, 2006).
91. Campion, A. & Kambhampati, P. Surface-enhanced Raman scattering. *Chem. Soc. Rev.* **27**, 241–250. <http://dx.doi.org/10.1039/A827241Z> (4 1998).
92. Willets, K. A. & Van Duyne, R. P. Localized Surface Plasmon Resonance Spectroscopy and Sensing. *Annual Review of Physical Chemistry* **58**. PMID: 17067281, 267–297. eprint: <https://doi.org/10.1146/annurev.physchem.58.032806.104607>. <https://doi.org/10.1146/annurev.physchem.58.032806.104607> (2007).
93. Guillot, N. & de la Chapelle, M. L. The electromagnetic effect in surface enhanced Raman scattering: Enhancement optimization using precisely controlled nanostruc-

- tures. *Journal of Quantitative Spectroscopy and Radiative Transfer* **113**. Electro-magnetic and Light Scattering by non-spherical particles XIII, 2321–2333. ISSN: 0022-4073. <http://www.sciencedirect.com/science/article/pii/S0022407312002403> (2012).
94. Kneipp, K., Wang, Y., Kneipp, H., Perelman, L. T., Itzkan, I., Dasari, R. R. & Feld, M. S. Single Molecule Detection Using Surface-Enhanced Raman Scattering (SERS). *Phys. Rev. Lett.* **78**, 1667–1670. <https://link.aps.org/doi/10.1103/PhysRevLett.78.1667> (9 1997).
95. Nie, S. & Emory, S. R. Probing Single Molecules and Single Nanoparticles by Surface-Enhanced Raman Scattering. *Science* **275**, 1102–1106. ISSN: 0036-8075. eprint: <https://science.sciencemag.org/content/275/5303/1102.full.pdf>. <https://science.sciencemag.org/content/275/5303/1102> (1997).
96. Yonzon, C. R., Haynes, C. L., Zhang, X., Walsh, J. T. & Van Duyne, R. P. A Glucose Biosensor Based on Surface-Enhanced Raman Scattering: Improved Partition Layer, Temporal Stability, Reversibility, and Resistance to Serum Protein Interference. *Analytical Chemistry* **76**, 78–85. ISSN: 0003-2700. <https://doi.org/10.1021/ac035134k> (2004).
97. Lyandres, O., Shah, N. C., Yonzon, C. R., Walsh, J. T., Glucksberg, M. R. & Van Duyne, R. P. Real-Time Glucose Sensing by Surface-Enhanced Raman Spectroscopy in Bovine Plasma Facilitated by a Mixed Decanethiol/Mercaptohexanol Partition Layer. *Analytical Chemistry* **77**, 6134–6139. ISSN: 0003-2700. <https://doi.org/10.1021/ac051357u> (2005).
98. Lin, X.-F., Ren, B. & Tian, Z.-Q. Electrochemical and Surface-Enhanced Raman Spectroscopic Studies on the Adsorption and Electrooxidation of C1 Molecules on

- a Roughened Rh Electrode. *The Journal of Physical Chemistry B* **108**, 981–986. ISSN: 1520-6106. <https://doi.org/10.1021/jp035433d> (2004).
99. Cui, L., Liu, Z., Duan, S., Wu, D.-Y., Ren, B., Tian, Z.-Q. & Zou, S.-Z. Orientation Change of Adsorbed Pyrazine on Roughened Rhodium Electrodes as Probed by Surface-Enhanced Raman Spectroscopy. *The Journal of Physical Chemistry B* **109**, 17597–17602. ISSN: 1520-6106. <https://doi.org/10.1021/jp052983y> (2005).
100. Cao, P., Sun, Y. & Gu, R. Surface-Enhanced Raman Spectroscopy Studies on the Adsorption and Electrooxidation of Carbon Monoxide at the Platinum/Formic Acid Interface. *The Journal of Physical Chemistry B* **108**, 4716–4722. ISSN: 1520-6106. <https://doi.org/10.1021/jp035324z> (2004).
101. Zheng, J.-Z., Ren, B., Wu, D.-Y. & Tian, Z.-Q. Thiourea adsorption on a Pt surface as detected by electrochemical methods and surface-enhanced Raman spectroscopy. *Journal of Electroanalytical Chemistry* **574**, 285–289. ISSN: 1572-6657. <http://www.sciencedirect.com/science/article/pii/S0022072804004358> (2005).
102. Gómez, R., Solla-Gullón, J., Pérez, J. M. & Aldaz, A. Surface-Enhanced Raman Spectroscopy Study of Ethylene Adsorbed on a Pt Electrode Decorated with Pt Nanoparticles. *ChemPhysChem* **6**, 2017–2021. eprint: <https://chemistry-europe.onlinelibrary.wiley.com/doi/pdf/10.1002/cphc.200500168>. <https://chemistry-europe.onlinelibrary.wiley.com/doi/abs/10.1002/cphc.200500168> (2005).
103. Baltruschat, H. Differential electrochemical mass spectrometry. *Journal of the American Society for Mass Spectrometry* **15**, 1693–1706. ISSN: 1044-0305. <https://pubs.acs.org/doi/abs/10.1021/jasms.8b02092> (2004).

104. Bruckenstein, S. & Gadde, R. R. Use of a porous electrode for in situ mass spectrometric determination of volatile electrode reaction products. *Journal of the American Chemical Society* **93**, 793–794. ISSN: 0002-7863. <https://doi.org/10.1021/ja00732a049> (1971).
105. Eggert, G. & Heitbaum, J. Electrochemical reactions of propylenecarbonate and electrolytes solved therein—a dems study. *Electrochimica Acta* **31**, 1443–1448. ISSN: 0013-4686. <http://www.sciencedirect.com/science/article/pii/0013468686870578> (1986).
106. Hartung, T. & Baltruschat, H. Differential electrochemical mass spectrometry using smooth electrodes: adsorption and hydrogen/deuterium exchange reactions of benzene on platinum. *Langmuir* **6**, 953–957. ISSN: 0743-7463. <https://doi.org/10.1021/la00095a012> (1990).
107. Baltruschat, H. & Schmiemann, U. The Adsorption of Unsaturated Organic Species at Single Crystal Electrodes Studied by Differential Electrochemical Mass Spectrometry. *Berichte der Bunsengesellschaft für physikalische Chemie* **97**, 452–460. eprint: <https://onlinelibrary.wiley.com/doi/pdf/10.1002/bbpc.19930970337>. <https://onlinelibrary.wiley.com/doi/abs/10.1002/bbpc.19930970337> (1993).
108. Wonders, A. H., Housmans, T. H. M., Rosca, V. & Koper, M. T. M. On-line mass spectrometry system for measurements at single-crystal electrodes in hanging meniscus configuration. *Journal of Applied Electrochemistry* **36**, 1215–1221. ISSN: 1572-8838. <https://doi.org/10.1007/s10800-006-9173-4> (2006).
109. Jambunathan, K. & Hillier, A. C. Measuring Electrocatalytic Activity on a Local Scale with Scanning Differential Electrochemical Mass Spectrometry. *J. Electrochem. Soc.* **150**, E312–E320. eprint: <http://jes.ecsdl.org/content/>

- 150/6/E312.full.pdf+html. <http://jes.ecsdl.org/content/150/6/E312.abstract> (2003).
110. Blessing, J. E., Ellefson, R. E., Raby, B. A., Brucker, G. A. & Waits, R. K. Recommended practice for process sampling for partial pressure analysis. *Journal of Vacuum Science & Technology A* **25**, 167–186. eprint: <https://doi.org/10.1116/1.2364001>. <https://doi.org/10.1116/1.2364001> (2007).
111. Grote, J.-P., Zeradjanin, A. R., Cherevko, S. & Mayrhofer, K. J. J. Coupling of a Scanning Flow Cell with Online Electrochemical Mass Spectrometry for Screening of Reaction Selectivity. *Rev. Sci. Instrum.* **85**, 104101. eprint: <https://doi.org/10.1063/1.4896755>. <https://doi.org/10.1063/1.4896755> (2014).
112. Levich, V. G. *Physicochemical hydrodynamics* (1962).
113. Bard, A. J. & Faulkner, L. R. *Electrochemical Methods: Fundamentals and Applications, 2nd Ed.* (John Wiley & Sons, New York, NY, 2000).
114. Gileadi, E. *Physical electrochemistry: fundamentals, techniques and applications* (2011).
115. Allen, J. B. & Larry, R. F. *Electrochemical methods fundamentals and applications* (John Wiley & Sons, 2001).
116. Nie, X., Esopi, M. R., Janik, M. J. & Asthagiri, A. Selectivity of CO₂ Reduction on Copper Electrodes: The Role of the Kinetics of Elementary Steps. *Angewandte Chemie International Edition* **52**, 2459–2462. eprint: <https://onlinelibrary.wiley.com/doi/pdf/10.1002/anie.201208320>. <https://onlinelibrary.wiley.com/doi/abs/10.1002/anie.201208320> (2013).

117. Wuttig, A., Liu, C., Peng, Q., Yaguchi, M., Hendon, C. H., Motobayashi, K., Ye, S., Osawa, M. & Surendranath, Y. Tracking a Common Surface-Bound Intermediate during CO₂-to-Fuels Catalysis. *ACS Central Science* **2**, 522–528. ISSN: 2374-7943. <https://doi.org/10.1021/acscentsci.6b00155> (2016).
118. Hori, Y., Koga, O., Watanabe, Y. & Matsuo, T. FTIR measurements of charge displacement adsorption of CO on poly- and single crystal (100) of Cu electrodes. *Electrochimica Acta* **44**, 1389–1395. ISSN: 0013-4686. <http://www.sciencedirect.com/science/article/pii/S0013468698002618> (1998).
119. Hirschmugl, C. J., Williams, G. P., Hoffmann, F. M. & Chabal, Y. J. Adsorbate-substrate resonant interactions observed for CO on Cu(100) in the far infrared. *Phys. Rev. Lett.* **65**, 480–483. <https://link.aps.org/doi/10.1103/PhysRevLett.65.480> (4 1990).
120. Akemann, W. & Otto, A. Vibrational modes of CO adsorbed on disordered copper films. *Journal of Raman Spectroscopy* **22**, 797–803. eprint: <https://onlinelibrary.wiley.com/doi/pdf/10.1002/jrs.1250221212>. <https://onlinelibrary.wiley.com/doi/abs/10.1002/jrs.1250221212> (1991).
121. Hollins, P., Davies, K. & Pritchard, J. Infrared spectra of CO chemisorbed on a surface vicinal to Cu(110): The influence of defect sites. *Surface Science* **138**, 75–83. ISSN: 0039-6028. <http://www.sciencedirect.com/science/article/pii/0039602884904965> (1984).
122. Hollins, P. & Pritchard, J. Infrared studies of chemisorbed layers on single crystals. *Progress in Surface Science* **19**, 275–349. ISSN: 0079-6816. <http://www.sciencedirect.com/science/article/pii/0079681685900152> (1985).

123. Vollmer, S., Witte, G. & Wöll, C. Determination of Site Specific Adsorption Energies of CO on Copper. *Catalysis Letters* **77**, 97–101. ISSN: 1572-879X. <https://doi.org/10.1023/A:1012755616064> (2001).
124. Bagus, P. & Pacchioni, G. Electric field effects on the surface—adsorbate interaction: cluster model studies. *Electrochimica Acta* **36**, 1669–1675. ISSN: 0013-4686. <http://www.sciencedirect.com/science/article/pii/S0013468691850242> (1991).
125. Koga, O., Teruya, S., Matsuda, K., Minami, M., Hoshi, N. & Hori, Y. Infrared spectroscopic and voltammetric study of adsorbed CO on stepped surfaces of copper monocrystalline electrodes. *Electrochimica Acta* **50**, 2475–2485. ISSN: 0013-4686. <http://www.sciencedirect.com/science/article/pii/S001346860401076X> (2005).
126. Heyes, J., Dunwell, M. & Xu, B. CO₂ Reduction on Cu at Low Overpotentials with Surface-Enhanced in Situ Spectroscopy. *The Journal of Physical Chemistry C* **120**, 17334–17341. ISSN: 1932-7447. <https://doi.org/10.1021/acs.jpcc.6b03065> (2016).
127. Pérez-Gallent, E., Figueiredo, M. C., Calle-Vallejo, F. & Koper, M. T. M. Spectroscopic Observation of a Hydrogenated CO Dimer Intermediate During CO Reduction on Cu(100) Electrodes. *Angewandte Chemie International Edition* **56**, 3621–3624. eprint: <https://onlinelibrary.wiley.com/doi/pdf/10.1002/anie.201700580>. <https://onlinelibrary.wiley.com/doi/abs/10.1002/anie.201700580> (2017).
128. Goodpaster, J. D., Bell, A. T. & Head-Gordon, M. Identification of Possible Pathways for C–C Bond Formation during Electrochemical Reduction of CO₂: New Theoretical Insights from an Improved Electrochemical Model. *The Journal of*

- Physical Chemistry Letters* **7**, 1471–1477. <https://doi.org/10.1021/acs.jpcllett.6b00358> (2016).
129. Herlihy, D. M., Waagele, M. M., Chen, X., Pemmaraju, C. D., Prendergast, D. & Cuk, T. Detecting the oxyl radical of photocatalytic water oxidation at an n-SrTiO₃/aqueous interface through its subsurface vibration. *Nature Chemistry* **8**, 549–555. ISSN: 1755-4349. <https://doi.org/10.1038/nchem.2497> (2016).
130. Akhade, S. A., Luo, W., Nie, X., Bernstein, N. J., Asthagiri, A. & Janik, M. J. Poisoning effect of adsorbed CO during CO₂ electroreduction on late transition metals. *Phys. Chem. Chem. Phys.* **16**, 20429–20435. <http://dx.doi.org/10.1039/C4CP03340J> (38 2014).
131. Mistry, H., Reske, R., Zeng, Z., Zhao, Z.-J., Greeley, J., Strasser, P. & Cuenya, B. R. Exceptional Size-Dependent Activity Enhancement in the Electroreduction of CO₂ over Au Nanoparticles. *Journal of the American Chemical Society* **136**, 16473–16476. ISSN: 0002-7863. <https://doi.org/10.1021/ja508879j> (2014).
132. Hori, Y., Murata, A., Tsukamoto, T., Wakebe, H., Koga, O. & Yamazaki, H. Adsorption of carbon monoxide at a copper electrode accompanied by electron transfer observed by voltammetry and IR spectroscopy. *Electrochimica Acta* **39**, 2495 – 2500. ISSN: 0013-4686. <http://www.sciencedirect.com/science/article/pii/0013468694002592> (1994).
133. Smith, B. D., Irish, D. E., Kedzierzawski, P. & Augustynski, J. A Surface Enhanced Raman Scattering Study of the Intermediate and Poisoning Species Formed during the Electrochemical Reduction of CO₂ on Copper. *Journal of The Electrochemical Society* **144**, 4288–4296. <https://doi.org/10.1149/1.1838180> (1997).

134. Wang, H.-F., Yan, Y.-G., Huo, S.-J., Cai, W.-B., Xu, Q.-J. & Osawa, M. Seeded growth fabrication of Cu-on-Si electrodes for in situ ATR-SEIRAS applications. *Electrochimica Acta* **52**, 5950–5957. ISSN: 0013-4686. <http://www.sciencedirect.com/science/article/pii/S0013468607004161> (2007).
135. Giorgetti, M., Passerini, S., Smyrl, W. H., Mukerjee, S., Yang, X. Q. & McBreen, J. In Situ X-Ray Absorption Spectroscopy Characterization of V₂O₅ Xerogel Cathodes upon Lithium Intercalation. *Journal of The Electrochemical Society* **146**, 2387–2392. <https://doi.org/10.1149/1.1391946> (1999).
136. Kuhl, K. P., Hatsukade, T., Cave, E. R., Abram, D. N., Kibsgaard, J. & Jaramillo, T. F. Electrocatalytic Conversion of Carbon Dioxide to Methane and Methanol on Transition Metal Surfaces. *Journal of the American Chemical Society* **136**, 14107–14113. ISSN: 0002-7863. <https://doi.org/10.1021/ja505791r> (2014).
137. Stancik, A. L. & Brauns, E. B. A simple asymmetric lineshape for fitting infrared absorption spectra. *Vibrational Spectroscopy* **47**, 66–69. ISSN: 0924-2031. <http://www.sciencedirect.com/science/article/pii/S0924203108000453> (2008).
138. Marcus, Y. Tetraalkylammonium Ions in Aqueous and Non-Aqueous Solutions. *J. Solution Chem.* **37**, 1071–1098. <https://doi.org/10.1007/s10953-008-9291-1> (2008).
139. Pearson, R. G. Absolute Electronegativity and Hardness: Application to Inorganic Chemistry. *Inorg. Chem.* **27**, 734–740. eprint: <https://doi.org/10.1021/ic00277a030>. <https://doi.org/10.1021/ic00277a030> (1988).
140. Roth, J. D. & Weaver, M. J. Role of the Double-Layer Cation on the Potential-Dependent Stretching Frequencies and Binding Geometries of Carbon Monoxide at Platinum-Nonaqueous Interfaces. *Langmuir* **8**, 1451–1458. eprint: <https://doi.org/10.1021/la00057a011> (1992).

- doi.org/10.1021/la00041a034. <https://doi.org/10.1021/la00041a034> (1992).
141. Calle-Vallejo, F. & Koper, M. Theoretical Considerations on the Electroreduction of CO to C₂ Species on Cu(100) Electrodes. *Angew. Chem. Int. Ed.* **52**, 7282–7285. <http://dx.doi.org/10.1002/anie.201301470> (2013).
142. Xiao, H., Cheng, T. & Goddard, W. A. Atomistic Mechanisms Underlying Selectivities in C₁ and C₂ Products from Electrochemical Reduction of CO on Cu(111). *J. Am. Chem. Soc.* **139**, 130–136. eprint: <http://dx.doi.org/10.1021/jacs.6b06846>. <http://dx.doi.org/10.1021/jacs.6b06846> (2017).
143. Bagger, A., Arnarson, L., Hansen, M. H., Spohr, E. & Rossmeisl, J. Electrochemical CO Reduction: A Property of the Electrochemical Interface. *J. Am. Chem. Soc.* **141**, 1506–1514. eprint: <https://doi.org/10.1021/jacs.8b08839>. <https://doi.org/10.1021/jacs.8b08839> (2019).
144. Wuttig, A. & Surendranath, Y. Impurity Ion Complexation Enhances Carbon Dioxide Reduction Catalysis. *ACS Catal.* **5**, 4479–4484. <http://dx.doi.org/10.1021/acscatal.5b00808> (2015).
145. Pérez-Gallent, E., Marcandalli, G., Figueiredo, M. C., Calle-Vallejo, F. & Koper, M. T. M. Structure- and Potential-Dependent Cation Effects on CO Reduction at Copper Single-Crystal Electrodes. *J. Am. Chem. Soc.* **139**, 16412–16419. eprint: <https://doi.org/10.1021/jacs.7b10142>. <https://doi.org/10.1021/jacs.7b10142> (2017).
146. Hori, Y., Murata, A., Takahashi, R. & Suzuki, S. Electrochemical Reduction of Carbon Monoxide to Hydrocarbons at Various Metal Electrodes in Aqueous Solution.

- Chem. Lett.* **16**, 1665–1668. ISSN: 1348-0715. <http://www.journal.csj.jp/doi/citedby/10.1246/cl.1987.1665> (1987).
147. White, J. L., Baruch, M. F., Pander, J. E., Hu, Y., Fortmeyer, I. C., Park, J. E., Zhang, T., Liao, K., Gu, J., Yan, Y., Shaw, T. W., Abelev, E. & Bocarsly, A. B. Light-Driven Heterogeneous Reduction of Carbon Dioxide: Photocatalysts and Photoelectrodes. *Chem. Rev.* **115**, 12888–12935. eprint: <http://dx.doi.org/10.1021/acs.chemrev.5b00370>. <http://dx.doi.org/10.1021/acs.chemrev.5b00370> (2015).
148. Wallace, W. E. in (National Institute of Standards and Technology, Gaithersburg MD, 20899, 2019). <https://doi.org/10.18434/T4D303>.
149. Waszczuk, P., Zelenay, P. & Sobkowski, J. Surface Interaction of Benzoic Acid with a Copper Electrode. *Electrochim. Acta* **40**, 1717–1721. ISSN: 0013-4686. <http://www.sciencedirect.com/science/article/pii/001346869500088V> (1995).
150. Conway, B. E. Kinetics of Electrolytic Hydrogen and Deuterium Evolution. *Proc. R. Soc. London, Ser. A* **256**, 128–144. eprint: <https://royalsocietypublishing.org/doi/pdf/10.1098/rspa.1960.0097>. <https://royalsocietypublishing.org/doi/abs/10.1098/rspa.1960.0097> (1960).
151. Dunwell, M., Wang, J., Yan, Y. & Xu, B. Surface Enhanced Spectroscopic Investigations of Adsorption of Cations on Electrochemical Interfaces. *Phys. Chem. Chem. Phys.* **19**, 971–975. <http://dx.doi.org/10.1039/C6CP07207K> (2017).
152. Ueba, H. Chemical Effects on Vibrational Properties of Adsorbed Molecules on Metal Surfaces: Coverage Dependence. *Surf. Sci.* **188**, 421–455. ISSN: 0039-6028. <http://www.sciencedirect.com/science/article/pii/S003960288780198X> (1987).

153. Bublitz, G. U. & Boxer, S. G. Stark Spectroscopy: Applications in Chemistry, Biology, and Materials Science. *Annu. Rev. Phys. Chem.* **48**, 213–242. eprint: <https://doi.org/10.1146/annurev.physchem.48.1.213>. <https://doi.org/10.1146/annurev.physchem.48.1.213> (1997).
154. Sorenson, S. A., Patrow, J. G. & Dawlaty, J. M. Solvation Reaction Field at the Interface Measured by Vibrational Sum Frequency Generation Spectroscopy. *J. Am. Chem. Soc.* **139**, 2369–2378. eprint: <https://doi.org/10.1021/jacs.6b11940>. <https://doi.org/10.1021/jacs.6b11940> (2017).
155. Ge, A., Videla, P. E., Lee, G. L., Rudshiteyn, B., Song, J., Kubiak, C. P., Batista, V. S. & Lian, T. Interfacial Structure and Electric Field Probed by in Situ Electrochemical Vibrational Stark Effect Spectroscopy and Computational Modeling. *J. Phys. Chem. C* **121**, 18674–18682. eprint: <https://doi.org/10.1021/acs.jpcc.7b05563>. <https://doi.org/10.1021/acs.jpcc.7b05563> (2017).
156. Clark, M. L., Ge, A., Videla, P. E., Rudshiteyn, B., Miller, C. J., Song, J., Batista, V. S., Lian, T. & Kubiak, C. P. CO₂ Reduction Catalysts on Gold Electrode Surfaces Influenced by Large Electric Fields. *J. Am. Chem. Soc.* **140**, 17643–17655. eprint: <https://doi.org/10.1021/jacs.8b09852>. <https://doi.org/10.1021/jacs.8b09852> (2018).
157. Lambert, D. K. Vibrational Stark Effect of CO on Ni(100), and CO in the Aqueous Double Layer: Experiment, Theory, and Models. *J. Chem. Phys.* **89**, 3847–3860. eprint: <https://doi.org/10.1063/1.454860>. <https://doi.org/10.1063/1.454860> (1988).
158. Bagus, P. S., Nelin, C. J., Müller, W., Philpott, M. R. & Seki, H. Field-Induced Vibrational Frequency Shifts of CO and CN Chemisorbed on Cu(100). *Phys. Rev. Lett.*

- 58**, 559–562. <https://link.aps.org/doi/10.1103/PhysRevLett.58.559> (1987).
159. Vetter, K. J. *Electrochemical Kinetics, Theoretical Aspects*; Academic Press; New York, NY (1967).
160. Anderson, M. R. & Huang, J. The Influence of Cation Size upon the Infrared Spectrum of Carbon Monoxide Adsorbed on Platinum Electrodes. *J. Electroanal. Chem.* **318**, 335–347. <http://www.sciencedirect.com/science/article/pii/002207289185315G> (1991).
161. Jiang, X. & Weaver, M. J. The Role of Interfacial Potential in Adsorbate Bonding: Electrode Potential-Dependent Infrared Spectra for Saturated CO Adlayers on Pt(110) and Related Electrochemical Surfaces in Varying Solvent Environments. *Surf. Sci.* **275**, 237–252. <http://www.sciencedirect.com/science/article/pii/003960289290797A> (1992).
162. Akhade, S. A., McCrum, I. T. & Janik, M. J. The Impact of Specifically Adsorbed Ions on the Copper-Catalyzed Electroreduction of CO₂. *Journal of The Electrochemical Society* **163**, F477–F484. <https://doi.org/10.1149/2.0581606jes> (2016).
163. Andersson, S. & Pendry, J. B. Structure of CO Adsorbed on Cu(100) and Ni(100). *Phys. Rev. Lett.* **43**, 363–366. <https://link.aps.org/doi/10.1103/PhysRevLett.43.363> (1979).
164. Łukomska, A. & Sobkowski, J. Potential of Zero Charge of Monocrystalline Copper Electrodes in Perchlorate Solutions. *J. Electroanal. Chem.* **567**, 95–102. ISSN: 1572-6657. <http://www.sciencedirect.com/science/article/pii/S002207280300799X> (2004).

165. Gileadi, E., Argade, S. D. & Bockris, J. O. The Potential of Zero Charge of Platinum and Its pH Dependence. *J. Phys. Chem.* **70**, 2044–2046. eprint: <https://doi.org/10.1021/j100878a501>. <https://doi.org/10.1021/j100878a501> (1966).
166. Chen, L. D., Urushihara, M., Chan, K. & Nørskov, J. K. Electric Field Effects in Electrochemical CO₂ Reduction. *ACS Catalysis* **6**, 7133–7139. <https://doi.org/10.1021/acscatal.6b02299> (2016).
167. Che, F., Gray, J. T., Ha, S., Kruse, N., Scott, S. L. & McEwen, J.-S. Elucidating the Roles of Electric Fields in Catalysis: A Perspective. *ACS Catal.* **8**, 5153–5174. eprint: <https://doi.org/10.1021/acscatal.7b02899>. <https://doi.org/10.1021/acscatal.7b02899> (2018).
168. Atkins, P. & de Paula, J. *Atkins' Physical Chemistry; Oxford University Press; Oxford, United Kingdom* (2002).
169. Verdaguer-Casadevall, A., Li, C. W., Johansson, T. P., Scott, S. B., McKeown, J. T., Kumar, M., Stephens, I. E. L., Kanan, M. W. & Chorkendorff, I. Probing the Active Surface Sites for CO Reduction on Oxide-Derived Copper Electrocatalysts. *J. Am. Chem. Soc.* **137**, 9808–9811. eprint: <http://dx.doi.org/10.1021/jacs.5b06227>. <http://dx.doi.org/10.1021/jacs.5b06227> (2015).
170. Kizhakevariam, N., Jiang, X. & Weaver, M. J. Infrared spectroscopy of model electrochemical interfaces in ultrahigh vacuum: The archetypical case of carbon monoxide/water coadsorption on Pt(111). *J. Chem. Phys.* **100**, 6750–6764. eprint: <https://doi.org/10.1063/1.467271>. <https://doi.org/10.1063/1.467271> (1994).
171. Ogasawara, H., Yoshinobu, J. & Kawai, M. Direct observation of the molecular interaction between chemisorbed CO and water overlayer on Pt(111). *Surf. Sci.* **386**,

- 73–77. ISSN: 0039-6028. <http://www.sciencedirect.com/science/article/pii/S003960289700321X> (1997).
172. Yan, Y.-G., Li, Q.-X., Huo, S.-J., Ma, M., Cai, W.-B. & Osawa, M. Ubiquitous Strategy for Probing ATR Surface-Enhanced Infrared Absorption at Platinum Group Metal-Electrolyte Interfaces. *J. Phys. Chem. B* **109**, 7900–7906. eprint: <https://doi.org/10.1021/jp044085s>. <https://doi.org/10.1021/jp044085s> (2005).
173. Nagao, M., Watanabe, K. & Matsumoto, Y. Ultrafast Vibrational Energy Transfer in the Layers of D₂O and CO on Pt(111) Studied with Time-Resolved Sum-Frequency-Generation Spectroscopy. *J. Phys. Chem. C* **113**, 11712–11719. eprint: <https://doi.org/10.1021/jp901793q>. <https://doi.org/10.1021/jp901793q> (2009).
174. Yan, Y.-G., Peng, B., Yang, Y.-Y., Cai, W.-B., Bund, A. & Stimming, U. Interfacial Water at a CO-Predosed Platinum Electrode: A Surface Enhanced Infrared Study with Strong Hydrogen Evolution Reaction Control. *J. Phys. Chem. C* **115**, 5584–5592. eprint: <https://doi.org/10.1021/jp104180n>. <https://doi.org/10.1021/jp104180n> (2011).
175. Cheng, T., Xiao, H. & Goddard, W. A. Full Atomistic Reaction Mechanism with Kinetics for CO Reduction on Cu(100) from Ab Initio Molecular Dynamics Free-Energy Calculations at 298 K. *Proc. Natl. Acad. Sci. U.S.A.* **114**, 1795–1800. ISSN: 0027-8424. eprint: <https://www.pnas.org/content/114/8/1795.full.pdf>. <https://www.pnas.org/content/114/8/1795> (2017).
176. Pérez-Gallent, E., Figueiredo, M. C., Calle-Vallejo, F. & Koper, M. T. M. Spectroscopic Observation of a Hydrogenated CO Dimer Intermediate During CO Re-

- duction on Cu(100) Electrodes. *Angew. Chem. Int. Ed.* **56**, 3621–3624. <http://dx.doi.org/10.1002/anie.201700580> (2017).
177. Schouten, K., Kwon, Y., van der Ham, C., Qin, Z. & Koper, M. A New Mechanism for the Selectivity to C₁ and C₂ Species in the Electrochemical Reduction of Carbon Dioxide on Copper Electrodes. *Chem. Sci.* **2**, 1902–1909. <http://dx.doi.org/10.1039/C1SC00277E> (2011).
178. Hersbach, T. J. P., McCrum, I. T., Anastasiadou, D., Wever, R., Calle-Vallejo, F. & Koper, M. T. M. Alkali Metal Cation Effects in Structuring Pt, Rh, and Au Surfaces through Cathodic Corrosion. *ACS Applied Materials & Interfaces* **10**, 39363–39379. ISSN: 1944-8244. <https://doi.org/10.1021/acsami.8b13883> (2018).
179. Gao, D., Sinev, I., Scholten, F., Arán-Ais, R. M., Divins, N. J., Kvashnina, K., Timoshenko, J. & Roldan Cuenya, B. Selective CO₂ Electroreduction to Ethylene and Multicarbon Alcohols via Electrolyte-Driven Nanostructuring. *Angew. Chem. Int. Ed.* **58**, 17047–17053. eprint: <https://onlinelibrary.wiley.com/doi/pdf/10.1002/anie.201910155>. <https://onlinelibrary.wiley.com/doi/abs/10.1002/anie.201910155> (2019).
180. Matsushima, H., Haak, C., Taranovskyy, A., Gründer, Y. & Magnussen, O. M. In Situ Video STM Studies of the Hydrogen-Induced Reconstruction of Cu(100): Potential and pH Dependence. *Phys. Chem. Chem. Phys.* **12**, 13992–13998. <http://dx.doi.org/10.1039/C0CP00659A> (2010).
181. Trotochaud, L., Young, S. L., Ranney, J. K. & Boettcher, S. W. Nickel–Iron Oxyhydroxide Oxygen-Evolution Electrocatalysts: The Role of Intentional and Incidental Iron Incorporation. *Journal of the American Chemical Society* **136**, 6744–6753. ISSN: 0002-7863. <https://doi.org/10.1021/ja502379c> (2014).

182. Garcia, A. C., Touzalin, T., Nieuwland, C., Perini, N. & Koper, M. T. M. Enhancement of Oxygen Evolution Activity of Nickel Oxyhydroxide by Electrolyte Alkali Cations. *Angewandte Chemie International Edition* **58**, 12999–13003. eprint: <https://onlinelibrary.wiley.com/doi/pdf/10.1002/anie.201905501>. <https://onlinelibrary.wiley.com/doi/abs/10.1002/anie.201905501> (2019).
183. Sheng, W., Myint, M., Chen, J. G. & Yan, Y. Correlating the hydrogen evolution reaction activity in alkaline electrolytes with the hydrogen binding energy on monometallic surfaces. *Energy Environ. Sci.* **6**, 1509–1512. <http://dx.doi.org/10.1039/C3EE00045A> (5 2013).
184. Gileadi, E. *Physical Electrochemistry*. Wiley-VCH Verlag GmbH & KGaA; Weinheim, Germany (2011).
185. Holewinski, A. & Linic, S. Elementary Mechanisms in Electrocatalysis: Revisiting the ORR Tafel Slope. *J. Electrochem. Soc.* **159**, H864–H870. <https://doi.org/10.1149%2F2.022211jes> (2012).
186. Mills, J. N., McCrum, I. T. & Janik, M. J. Alkali cation specific adsorption onto fcc(111) transition metal electrodes. *Phys. Chem. Chem. Phys.* **16**, 13699–13707. <http://dx.doi.org/10.1039/C4CP00760C> (27 2014).
187. Danilovic, N., Subbaraman, R., Strmcnik, D., Paulikas, A. P., Myers, D., Stamenkovic, V. R. & Markovic, N. M. The Effect of Noncovalent Interactions on the HOR, ORR, and HER on Ru, Ir, and Ru_{0.50}Ir_{0.50} Metal Surfaces in Alkaline Environments. *Electrocatalysis* **3**, 221–229. ISSN: 1868-5994. <https://doi.org/10.1007/s12678-012-0100-7> (2012).
188. Xue, S., Garlyyev, B., Watzele, S., Liang, Y., Fichtner, J., Pohl, M. D. & Bandarenka, A. S. Influence of Alkali Metal Cations on the Hydrogen Evolution Re-

action Activity of Pt, Ir, Au, and Ag Electrodes in Alkaline Electrolytes. *ChemElectroChem* **5**, 2326–2329. eprint: <https://chemistry-europe.onlinelibrary.wiley.com/doi/pdf/10.1002/celc.201800690>. <https://chemistry-europe.onlinelibrary.wiley.com/doi/abs/10.1002/celc.201800690> (2018).